

**Quantitative nuclear imaging
for dosimetry
in radioembolization**

Mattijs Elschot

Quantitative nuclear imaging for dosimetry in radioembolization

PhD thesis, Utrecht University – with a summary in Dutch

© M. Elschot, Utrecht, 2013

elschot.mattijs@gmail.com

All rights reserved. No part of this publication may be reproduced or transmitted in any form or by any means without permission in writing from the author. The copyright of the articles that have been published or have been accepted for publication has been transferred to the respective journals.

ISBN: 978-94-6108-464-4

Cover design: Mattijs Elschot

Lay-out and printing: Gildeprint Drukkerijen - Enschede

**Quantitative nuclear imaging
for dosimetry
in radioembolization**

**Kwantitatieve nucleaire beeldvorming
voor dosimetrie bij radioembolisatie**
(met een samenvatting in het Nederlands)

Proefschrift

ter verkrijging van de graad van doctor
aan de Universiteit Utrecht
op gezag van de rector magnificus, prof.dr. G.J. van der Zwaan,
ingevolge het besluit van het college voor promoties
in het openbaar te verdedigen
op dinsdag 25 juni 2013 des middags te 4.15 uur

door

Mattijs Elschot
geboren op 3 november 1983
te Beuningen

Promotoren: Prof. dr. ir. M.A. Viergever
Prof. dr. M.A.A.J. van den Bosch

Co-promotor: Dr. ir. H.W.A.M. de Jong

Publication of this thesis was financially supported by:

Mallinckrodt Nederland B.V.

MRI Centrum

Stichting Ina Veenstra-Rademaker

Sirtex Medical Europe GmbH

Röntgenstichting

Contents

Chapter 1	General introduction and outline of thesis	7
Chapter 2	Quantitative evaluation of scintillation camera imaging characteristics of radionuclides used in liver radioembolization	33
Chapter 3	Quantitative comparison of PET and Bremsstrahlung SPECT for imaging the <i>in vivo</i> yttrium-90 microsphere distribution after liver radioembolization	53
Chapter 4	Quantitative Monte Carlo-based yttrium-90 SPECT reconstruction	75
Chapter 5	Quantitative Monte Carlo-based holmium-166 SPECT reconstruction	95
Chapter 6	Tc-99m-MAA overestimates the dose to the lungs in radioembolization: a quantitative evaluation in patients treated with Ho-166 microspheres	117
Chapter 7	Summary and general discussion	137
Addenda	Samenvatting in het Nederlands	151
	Dankwoord/Acknowledgments	159
	List of affiliations	163
	List of publications	165
	Curriculum Vitae	169

Chapter 1

General introduction and outline of thesis



1.1 Motivation

Liver cancer is a major cause of death worldwide. Radioembolization is a relatively new treatment form for this type of cancer, which involves the administration of radioactive microspheres to the hepatic artery for selective targeting of the liver malignancies. For treatment planning and evaluation in radioembolization, it is of utmost importance to gain knowledge about the distribution of the microspheres inside and outside the liver. In this thesis, quantitative nuclear imaging methods are presented, which enable accurate assessment of the *in vivo* distribution of the microspheres used in radioembolization.

1.2 Background and outline of the introduction

Emission tomography is a nuclear imaging technique, which has been used since the 1970s to visualize the three-dimensional (3D) distribution of radionuclides in patients. The most commonly used modalities today are single photon emission computed tomography (SPECT) and positron emission tomography (PET). SPECT is generally employed for imaging gamma photon-emitting radionuclides, whereas PET is used for positron-emitters. Most often, the radionuclide of interest is labeled to a biological compound, together forming a so-called radiopharmaceutical. Today, numerous radiopharmaceuticals are available to study a wide range of metabolic processes in the human body. This makes SPECT and PET indispensable for diagnostics and therapy evaluation in neurology, cardiology, oncology, and other fields of clinical research (1,2).

In many of these applications, the objective of emission tomography is quantification of the radionuclide activity concentration. Quantitative information enables comparison with reference values from population databases in cardiology and neurology, evaluation of disease progress on multiple time points in oncology, and estimation of the local delivered dose in radionuclide therapies. Unfortunately, acquisition of quantitative information is hampered by various effects, including photon scatter, photon attenuation, and instrumentation-related limitations. Although these effects play an important role in both PET and SPECT, the former is regarded by many as a “quantitative” modality, whereas the latter modality is traditionally regarded as “qualitative” (3). This is largely motivated by the fact that quantification has always been crucial for clinical PET applications (e.g. pharmacokinetic analysis), which stimulated the development of correction methods for image degrading

effects. Quantification with SPECT, on the other hand, is complicated by the rotating cameras, the collimators, and the variety of used radionuclides, all with different gamma photon energies. However, supported by increasing computer power and the introduction of hybrid SPECT/CT scanners, correction techniques have now evolved to the point that quantitative SPECT images are sufficiently accurate to be used in clinical practice. A timely overview of clinical applications that use SPECT for activity quantification is given by Bailey and Willowson (3).

Internal radiation therapy for treatment of cancer is one of the fields that have particularly triggered the recent interest in quantitative SPECT. The ideal radionuclides for internal radiation therapy are combined beta-gamma emitters; the high-energy beta-particles are used for tumor destruction, while the gamma photons enable image-based treatment planning and evaluation (i.e. dosimetry) (4). A relatively new form of internal radiation therapy is radioembolization, during which radio-labeled microspheres are administered to the hepatic artery for selective treatment of liver malignancies (5). Like all therapies based on ionizing radiation, radioembolization requires some form of treatment planning and evaluation, which should aim to optimize treatment efficacy, while keeping toxicity acceptably low. Unfortunately, the most commonly used methods for treatment planning in radioembolization lack patient-specificity and are mainly based on semi-empiric evidence with regard to toxicity and efficacy (see section 1.5.2). Although this methodology keeps the average toxicity over the patient population low, it possibly falls short in optimizing the radiation absorbed dose to the tumors for each patient individually (6). More personalized dosimetry methods exist, but are hindered by the lack of quantitative nuclear imaging possibilities for assessment of the microsphere distribution.

In this thesis, quantitative nuclear imaging methods are developed, evaluated, and exploited to improve personalized dosimetry in radioembolization. The largest part of this thesis is dedicated to the development of reconstruction algorithms for quantitative SPECT. Therefore, the general principles of SPECT are extensively discussed in the section 1.3 of this introductory chapter. Quantitative PET plays a somewhat smaller role in radioembolization and is shortly explained in section 1.4. In section 1.5, the general principles of radioembolization are surveyed, while focusing on personalized dosimetry and the challenges that currently impede it.

1.3 SPECT

1.3.1 Basic principles

A SPECT scanner is designed for detection of single gamma photons in the energy range of a several tens to a few hundred keV. The system consists of one or more gamma cameras (detectors) mounted on a flexible gantry. Newer systems typically combine two detectors with a CT scanner. During a SPECT acquisition, the detectors rotate around the patient, and two-dimensional (2D) projection images of the 3D activity distribution are recorded from a number of different angles. To enable proper reconstruction of the activity distribution, the detectors should together cover an orbit of at least 180°, and a sufficiently large number of projection angles should be chosen (7).

Scintillation detection

Most SPECT detectors that are used in clinical practice today consist of a lead collimator, a large-area (40 cm x 50 cm) NaI(Tl) scintillation crystal, a light guide, photomultiplier tubes (PMT), and front end electronics connected to a computer (Figure 1.1 A). Detection of a photon impinging on the scintillation crystal generally starts with photoelectric absorption, i.e. the complete photon energy is transferred to an atomic electron of the crystal. If the photon energy is higher than the binding energy of the electron, the electron can be ejected from its shell. This secondary electron travels through the crystal, while transferring its kinetic energy to thousands of atomic electrons as a result of inelastic collisions. The transferred energy is subsequently released in the form of (near) visible light (scintillation photons), hence the name “scintillation crystal”. After passing through the crystal and the light guide, the scintillation photons impinge on the photocathode of one of the PMTs. Secondary electrons are released, the number of which is multiplied in the PMT to produce a measurable electrical signal. Since a single, large-area, crystal is used and scintillation photons are emitted in a random direction, all PMTs contribute to the detection of a single photon. The mean position of gamma photon absorption is calculated by weighting the position of each PMT by the strength of its signal (Anger logics) and the photon energy is calculated by summing all PMT signals (7). The pulse-height of the final signal is proportional to the photon energy absorbed in the crystal, since all previously described processes are linear. This enables discrimination between photons based upon their energy, albeit to a limited extent; the energy resolution of NaI(Tl) scintillation detectors is approximately 10% (7). The width of the energy

detection window is generally set to 15 – 20% of the photopeak value, to include the majority of the photopeak photons.

Collimation

When a photon is emitted by a radiopharmaceutical, it travels in a random direction. This direction cannot be deduced from the signal provided by the scintillation detector; hence some form of collimation is required to determine the spatial distribution of the radiopharmaceuticals. This is performed by a mechanical collimator, which consists of a few centimeter-thick lead slab with tens of thousands small holes. The photons that propagate parallel to the axis of the holes reach the crystal, while the majority of the others are absorbed by the collimator. Consequently, this spatial information is won at the cost of a tremendous loss of sensitivity. Several types of collimators exist, which are mainly distinguished by the shape and orientation of their holes. Popular collimator types include fan-beam, cone-beam, pin-hole, and parallel-hole collimators, of which the latter is most widely used in the clinic today (7).

1.3.2 Image degrading effects

From the moment of emission in the patient until the moment of absorption in the scintillation crystal, photons are at serious risk of losing their spatial information by deviating from their original path. Properly collimated, non-collided photons that are directly detected in the energy window as a result of photoelectric absorption are referred to as primary photons (Figure 1.1 A, B, C; photon 1). All other photons are considered non-primary photons. Detection of non-primary photons degrades the visual quality and quantitative accuracy of the reconstructed SPECT images (8). Degradation of the SPECT image quality is mainly caused by photon interaction with the patient (Figure 1.1 A), collimator and detector limitations (Figure 1.1 B and C, respectively), and Poisson noise. It is also affected count rate linearity, radionuclide half-life, patient motion, and other factors that will not be discussed here. Non-primary photons typically constitute 20 – 50% of all photons detected in the energy window, although this number is largely dependent on the applied radionuclide and imaging situation. An extensive overview of all image degrading effects is given elsewhere (7).

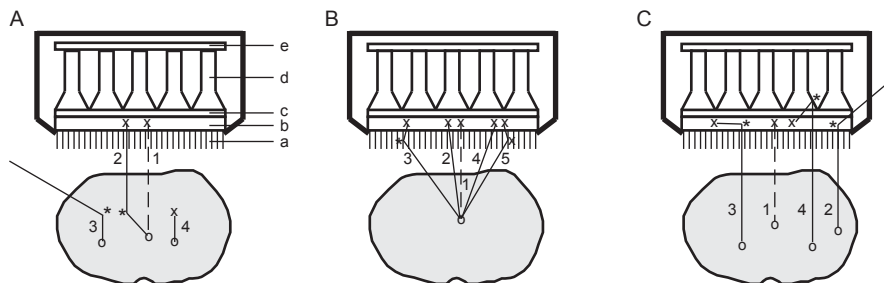


Figure 1.1. A schematic illustration of photon transport processes in SPECT imaging. The gamma camera includes a collimator (A, a), scintillation crystal (A, b), optical light guide (A, c), PMTs (A, d), and front-end electronics (A, e). The image can be degraded due to photon interaction with the patient (A), collimator (B), and detector (C). Primary photon paths are illustrated by dashed lines (photons numbered 1) and non-primary photon paths by solid lines (photons numbered 2 and higher). Positions of photon emission (o), Compton scatter (*), and photoelectric absorption (x) are also illustrated. The numbered photon paths are explained in the text of section 1.3.2.

Photon-patient interaction

Photons primarily interact with matter by photoelectric absorption, Compton scatter, coherent (Rayleigh) scatter, and pair production. For photons in the SPECT energy range, Compton scatter is the predominant effect in matter with low atomic number, such as the human body. In matter with high atomic number, such as the lead collimator, photoelectric absorption is dominant. Coherent scatter and pair production do not play a significant role in SPECT. (7)

In nuclear imaging, photon-patient interactions are usually divided in photon scatter and photon attenuation. Although it is common to treat these processes separately, they both primarily result from the Compton scatter. Compton scatter is the deflection of a photon due to interaction with an electron. During this process, part of the photon energy is transferred to the electron. The energy of the scattered photon (E_s) is dependent on the angle of deflection (θ) and is described with the Compton formula (9)

$$E_s = \frac{E_0}{1 + \frac{E_0}{mc^2}(1 - \cos(\theta))} \quad (1.1)$$

Here, E_0 is the energy of the incident photon, and mc^2 the energy of the electron at rest. The probability of scattering over an angle θ depends on the photon energy and is described by the Klein-Nishina formula in (10).

In nuclear imaging, scattered photons are considered those photons that are detected in the photopeak energy window after Compton scattering in the patient (Figure 1.1 A; photon 2). As is apparent from equation 1.1, relatively large angular

deflections lead to relatively small loss of photon energy. Because the energy window is not infinitely small (typically 15% – 20% full-width at half-maximum (FWHM)), scattered photons can still be detected, in spite of their lower energy. For radionuclides that emit multiple gamma photons, scattered high-energy photons can also be detected in the lower-energy photopeak window (down-scatter). In most clinical situations, scattered photons account for 30 – 40% of the total detected photons, which leads to blurred projection images, suboptimal reconstructed contrast, and errors in quantification of the reconstructed activity distribution (11).

Photon attenuation is considered the reduction of the photon flux towards the detector due to collisions with electrons in the patient's tissue. Both Compton interactions (Figure 1.1 A; photon 3) and photoelectric absorption (Figure 1.1 A; photon 4) contribute to attenuation, albeit the latter to a small extent. The reduction in flux of a narrow beam of photons with a given energy depends on the composition and thickness of the attenuation material it is passing through, and can be described by

$$\frac{\Phi_a}{\Phi_0} = \exp\left(-\int_0^D \mu^{PE}(l) + \mu^{CS}(l) dl\right) \quad (1.2)$$

Here, Φ_0 is the incident photon flux, Φ_a the attenuated photon flux, D the material thickness (cm), and $\mu^{PE}(l)$ and $\mu^{CS}(l)$ the linear attenuation coefficients of the medium at position l (cm^{-1}) as a result of the photoelectric effect and Compton scatter, respectively. The probability of both photoelectric absorption and Compton interaction depend on the energy of the photons that pass through the medium. Photon attenuation leads to underestimation of activity in structures that are located more centrally in body (12).

Collimator-detector effects

The collimator is designed to photoelectrically absorb all photons that do not traverse it on a line parallel to the collimator septa. However, the collimator holes are not infinitely narrow, and therefore all photons that arrive within a small solid angle ($\pm 1^\circ$) are accepted, which leads to a substantial loss in resolution (Figure 1.1 B; photon 2). Since the collimator resolution increases (approximately) linearly with increasing distance to the source (13,14), it is beneficial to position the detector as close to the patient as possible. Other collimator-related effects that degrade the image quality include Compton scatter in the collimator (Figure 1.1 B; photon 3), penetration of (high-energy) photons through the collimator septa (Figure 1.1 B; photon 4), and

characteristic lead X-rays, which can be emitted from the collimator as a result of photoelectric absorption of energies that exceed the binding energy of the atomic lead electrons (Figure 1.1 B; photon 5). The latter is only important for radionuclides that require an energy window around 90 keV or lower, since the energies of the relevant lead X-rays are 73, 75, and 85 keV.

Although the collimator resolution dominates the spatial resolution of reconstructed SPECT images, there are also several detector-related effects that deserve attention here. Compton scatter in the crystal may lead to partial energy deposition (Figure 1.1 C; photon 2) or may introduce uncertainty in event localization (Figure 1.1 C; photon 3). Additionally, higher-energy photons can backscatter in the PMTs, front-end electronics, or lead casing of the detector head, after which they may still be detected in the energy window (Figure 1.1 C; photon 4). Also, the intrinsic spatial resolution of a modern large-area scintillation crystal is limited to approximately 3 – 4 mm FWHM, which introduces additional blurring of the projection images (7). All these collimator-detector related image degrading effects complicate reconstruction of the source to the correct location, which reduces the spatial accuracy of the reconstructed activity distribution (8).

Poisson noise

Projection measurements are affected by Poisson noise, since radioactive decay, Compton scatter, and photoelectric absorption are Poisson processes. For such a process, the standard deviation on the number of counts measured in a pixel is equal to the square root of the number of counts (7). Therefore, the more counts are acquired, the higher the signal-to-noise ratio (SNR) of the measurement. However, the number of counts per pixel is typically low in emission tomography, as a result of efforts to keep the dose to the patient as low as reasonably achievable (ALARA). In clinical practice, this often means that spatial resolution is sacrificed for noise reduction, e.g. by averaging counts or low-pass filtering of the projection data (15). Consequently, Poisson noise limits the visual image quality and the quantitative accuracy of reconstructed activity in small structures (12).

1.3.3 Quantitative reconstruction

In emission tomography, reconstruction is the mathematical process of rebuilding a 3D object from its 2D projections. Today, statistical iterative reconstruction methodology is preferred over analytical filtered back projection (FBP), because its framework allows for modeling of photon transport and statistical variations. An

important feature of iterative reconstruction is that correction for image degrading effects is provided by incorporation of these effects in the photon transport model (15).

Iterative reconstruction

The framework of iterative reconstruction consists of the following four repetitive steps: forward projection, error calculation, back projection, and image updating (Figure 1.2). Projection images of an initial estimate of the activity distribution (image) are calculated in the forward projection step. Subsequently, error projections are calculated by comparison of the measured projection data to the estimated projection data. These error projections are then back projected to an error image, which is subsequently used to update the estimated image by multiplication. This process is iterated until a satisfactory image is obtained. Today, most iterative reconstruction methods are based on the maximum-likelihood expectation-maximization (MLEM) reconstruction algorithm (16,17). The MLEM algorithm seeks to converge to the activity distribution that maximizes the probability of the measured projection data, given a photon transport model. The Poisson nature of the emission process is taken into account by treating the measured projection data as Poisson random variables, and not as exact measurements. Photon transport is modeled by the system matrix $P = \{p_{i,j}\}$, which consists of the set of probabilities that image voxel i contributes to projection bin j (for forward projection) and vice versa (for back projection). The MLEM algorithm updates all voxels i of the estimated image at iteration $k+1$, according to

$$im_i^{k+1} = im_i^k \cdot \frac{1}{\sum_j p_{i,j}} \cdot \sum_j \left[p_{i,j} \cdot \frac{s_j}{\sum_i p_{i,j} \cdot im_i^k} \right] \quad (1.3)$$

Here, $IM^k = \{im_i^k\}$ is the k^{th} estimate of the activity distribution, $S = \{s_j\}$ is the sinogram of the measured projection bins, and $P = \{p_{i,j}\}$ the system matrix. Convergence is reached when the estimated projection data are as similar as possible to the measured projection data, i.e. when the most right ratio in equation 1.3 reaches unity. Consequently, the more accurate the photon transport is modeled by the system matrix, the more accurate is the estimate of the activity distribution.

A major drawback of MLEM is that it is notoriously slow. Therefore, the much faster alternative Ordered Subsets Expectation-Maximization (OSEM) is generally used in clinical practice (18). OSEM is an accelerated, block-iterative MLEM method, which divides the projection data in a number of subsets ordered to projection angle.

The MLEM algorithm is then applied to each subset, thereby generating a number of update steps per iteration that is equal to the number of subsets. OSEM is able to achieve acceleration factors as high as the number of subsets, while keeping loss in image quality marginal (19). Further speed up of the OSEM algorithm can be achieved by reducing the complexity of the system matrix used in the back projection step. Such a dual-matrix approach has negligible impact on the image quality in comparison with standard OSEM (20).

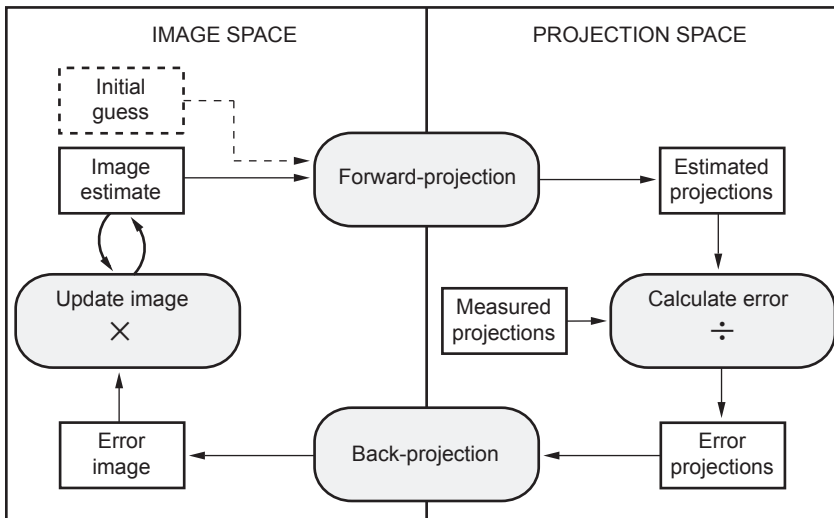


Figure 1.2. A schematic illustration of the iterative reconstruction process, specific for the maximum-likelihood expectation maximization (MLEM) algorithm (see section 1.3.3).

Photon transport modeling

Iterative reconstruction enables correction of image degrading effects by modeling these effects in the system matrix. This approach requires i) a patient-specific attenuation map, and ii) an accurate method for calculation of photon transport from emission to detection (15). Since the introduction of modern SPECT/CT scanners, a high quality attenuation map can be conveniently derived from the co-registered CT-images. This requires transformation from Hounsfield units to linear attenuation coefficients and subsequent conversion from the averaged spectrum of X-ray energies to the gamma photon energy (21). Photon transport is usually separately modeled for attenuation, scatter, and collimator-detector related effects. As explained in section 1.3.2, the shape and magnitude of these effects depend on many factors, including photon energy, tissue density and composition, collimator and detector characteristics, the distance between the source and the detector, and

energy window settings. Therefore, the required complexity of the photon transport models (and system matrix) very much depends on the photon energy spectrum of the administered radionuclide and the body part under investigation. For example, it has been demonstrated that quantitative SPECT with technetium-99m (^{99m}Tc) is already feasible with a rather approximate scatter model like the triple energy window (TEW) method (22,23). To the contrary, iodine-131 (^{131}I) requires a more extensive photon transport model, such as the effective scatter source estimation (ESSE) method, to compensate for deteriorating effects of high-energy photon contributions (24,25). A yet different approach with several attractive features is to calculate the photon transport “on-the-fly”, by making use of fast Monte Carlo simulations (26). Thanks to the development of effective acceleration methods (27-29) and the rapid increase in computer power, Monte Carlo-based photon transport modeling is now fast enough for clinical application (30,31). This approach is very flexible, since the photon transport can be completely simulated during the reconstruction process, irrespective of activity distribution, photon energy, scatter order, tissue density homogeneity, and other complicating factors (11). For a more complete overview of model-based correction approaches and their implementation in the MLEM algorithm, the reader is directed to excellent reviews on attenuation (32), scatter (11), and collimator-detector effects (33).

Image calibration

To obtain absolute quantitative values, the voxel intensities in the attenuation and scatter corrected SPECT images need to be converted from reconstructed counts into units of activity concentration (Bq ml^{-1}), which requires cross-calibration of the system sensitivity. A calibration factor is usually determined from projections of a point source in air or from reconstructed images of a uniform activity phantom (4). In both cases, the activity is first measured in a dose calibrator. Calibration factors must be determined for each unique combination of camera, collimators, radionuclide, and energy window.

1.4 PET

1.4.1 Basic principles

A PET camera is optimized for coincidence detection of a pair of 511 keV photons, which are emitted in near opposite direction as a result of positron-electron annihilation (34). PET cameras are equipped with many small scintillation detectors,

which are positioned in multiple rings surrounding the patient. A PET camera does not require a mechanical collimator, since the line of response is implicitly defined by simultaneous detection of a pair of annihilation photons in opposing detectors (Figure 1.3 A).

1.4.2 Image degrading effects

In addition to Poisson noise, the main image degrading effects in PET include scattered coincidences, random coincidences, and photon attenuation (34). Scattered coincidences result from Compton scattering of one or both of the annihilation photons before detection and may account for 35% – 50% of the total number of coincidences in 3D PET (35). Random coincidences occur when a pair of photons not originating from the same annihilation event is simultaneously detected. As illustrated in Figure 1.3, both scattered and random coincidences result in incorrect lines of response. Like in SPECT, photon attenuation in PET is mainly the result of Compton scattering and some photoelectric absorption. In addition to these image degrading effects, the spatial resolution of the reconstructed PET images is affected by the limited intrinsic resolution of the scintillation detectors ($\sim 2 - 3$ mm FWHM), the positron range before annihilation ($\sim 0.2 - 2$ mm), and small deviations from the 180° angle of annihilation photon emission ($\sim 0.3^\circ$), which is due to residual kinetic energy of the positron (34).

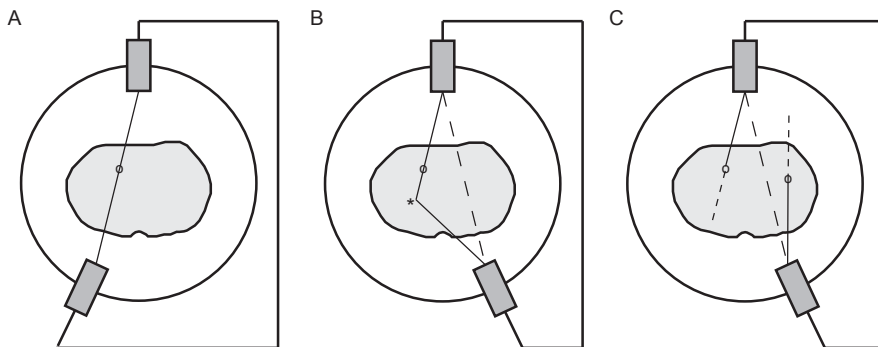


Figure 1.3. A schematic illustration of detection of primary (A), scattered (B), and random (C) events with a PET camera (see section 1.4.2). Photon paths are illustrated by solid lines and lines of response with dashed lines.

1.4.3 Quantitative reconstruction

The MLEM algorithm (or a derivative thereof) is the preferred algorithm for quantitative PET reconstruction, for the reasons discussed in section 1.3.3. In PET, modeling of photon attenuation is relatively straightforward, since it is independent of the emission position on the line of response (32). In clinical practice, the distribution of scattered coincidences is often estimated with the single scatter simulation (SSS) algorithm (36,37) and the distribution of random coincidences is usually estimated using (smoothed) delayed window techniques (34). Since these estimates are stationary (i.e. they do not require to be estimated during reconstruction), they can be modeled outside the system matrix of the MLEM algorithm (38)

$$im_i^{k+1} = im_i^k \cdot \frac{1}{\sum_j \frac{p_{i,j}}{a_j \cdot n_j}} \cdot \sum_j \left[p_{i,j} \cdot \frac{s_j}{\sum_i p_{i,j} \cdot im_i^k + (r_j \cdot n_j + c_j) \cdot a_j} \right] \quad (1.4)$$

Here, $IM^k = \{im_i^k\}$ is the k^{th} estimate of the activity distribution, $A = \{a_j\}$ the estimated attenuation, $C = \{c_j\}$ the estimated scatter, $R = \{r_j\}$ the estimated randoms, and $N = \{n_j\}$ the set of normalization factors, which correct for the non-uniform detector response. In this case, only the spatial response of the detector (39) and time-of-flight (TOF) information (if available) (40) have to be incorporated in the system matrix.

Calibration of reconstructed counts into units of activity concentration is relatively straightforward in PET, since the photon energy does not depend on the radiopharmaceutical. Consequently, all manufacturers provide procedures that allow for incorporation of the calibration factors in the reconstruction software (3).

1.5 Radioembolization

1.5.1 Rationale

Liver cancer, whether primary or metastatic, is a major cause of death worldwide (41). Partial hepatectomy is the treatment option of choice, but only a small fraction of the patients is eligible for complete surgical resection (42-44). Unfortunately, the effect of systemic chemotherapy on overall survival is insignificant for most tumor types, despite recent improvements in response rates and median survival (45,46). High tumor response rates have been reported for novel external radiation therapy techniques, including stereotactic body radiation therapy (SBRT) (47,48). Due to the limited tolerance of the healthy liver parenchyma to radiation (49), however, this application remains restricted to patients with a limited number of hepatic tumors

(48). Radioembolization is a relatively novel treatment option that can be described as selectively targeted internal radiation therapy. The efficacy of radioembolization relies on the fact that liver malignancies are exclusively perfused by arterial blood, whereas the healthy liver parenchyma mainly depends on the portal vein for its blood supply (50,51). This difference in blood supply is exploited by administration of embolic microspheres loaded with a high-energy beta-emitting radionuclide to the hepatic artery, which results in selective targeting of the tumors. Since the mean range of the beta-particles in tissue is in the order of a few millimeters, radioembolization leads to high tumor absorbed radiation doses, while the healthy liver parenchyma remains relatively spared (52,53).

1.5.2 Yttrium-90 radioembolization

Radioembolization using microspheres loaded with the high-energy beta-emitter yttrium-90 (^{90}Y , $E_{\beta,\text{max}} = 2.280 \text{ MeV}$ [$I = 100.0\%$]) is increasingly used as first-line or salvage treatment for unresectable liver tumors (54,55). To date, more than 18,000 patients have been treated with commercially available glass (TheraSphere; MDS Nordion, Ontario, Canada) and resin microspheres (SIR-Spheres; Sirtex Medical, Sydney, Australia). ^{90}Y radioembolization is associated with high tumor response rates (54,56-58), but the effect on overall survival is yet to be established. The ^{90}Y microsphere characteristics are provided in Table 1.1.

Table 1.1. Microsphere characteristics.

Microsphere (MS)	Glass ^{90}Y -MS	Resin ^{90}Y -MS	^{166}Ho -MS
Matrix material	Glass	Resin	poly(L-lactic acid)
Radionuclide	^{90}Y	^{90}Y	^{166}Ho
Half-life (h)	64.1	64.1	26.8
gamma-energy (keV)	-	-	80.6
beta-energy (MeV)	2.28 (100%)	2.28 (100%)	1.77 (49%); 1.85 (50%)
Sphere size (μm)	25 (20 – 30)	32 (20 – 60)	30 (20 – 50)
Activity sphere ⁻¹ (Bq)	2500	50	< 450
No. microspheres	4×10^6	50×10^6	33×10^6

Angiography and microsphere delivery

The procedure of microsphere delivery in ^{90}Y radioembolization is shortly surveyed here. A schematic overview of the procedure is given in Figure 1.4. Detailed descriptions of the standardized procedure can be found elsewhere (52,59). The ^{90}Y radioembolization procedure includes a standard work-up angiography for prophylactic coil-embolization of non-target vessels, followed by administration of

a scout dose of technetium-99m macroaggregated albumin (^{99m}Tc -MAA) particles through a microcatheter in the proper, left, or right hepatic artery. The ^{99m}Tc -MAA particles serve as a surrogate for the ^{90}Y microspheres and the distribution of the scout dose is assumed to mimic the distribution of the ^{90}Y treatment dose. Scintigraphic and SPECT(/CT) images of the ^{99m}Tc -MAA scout dose distribution are acquired for safety evaluation and treatment planning, as explained in the next section. In the absence of ^{99m}Tc -MAA deposition in extrahepatic tissue and excessive estimated lung dose, the patient is scheduled for treatment. On the day of treatment, a microcatheter is placed under angiography in the same position as used for administration of the ^{99m}Tc -MAA scout dose, followed by administration of the ^{90}Y treatment dose to the patient. Post-treatment Bremsstrahlung SPECT(/CT) imaging is recommended for evaluation of the distribution of the ^{90}Y treatment dose.

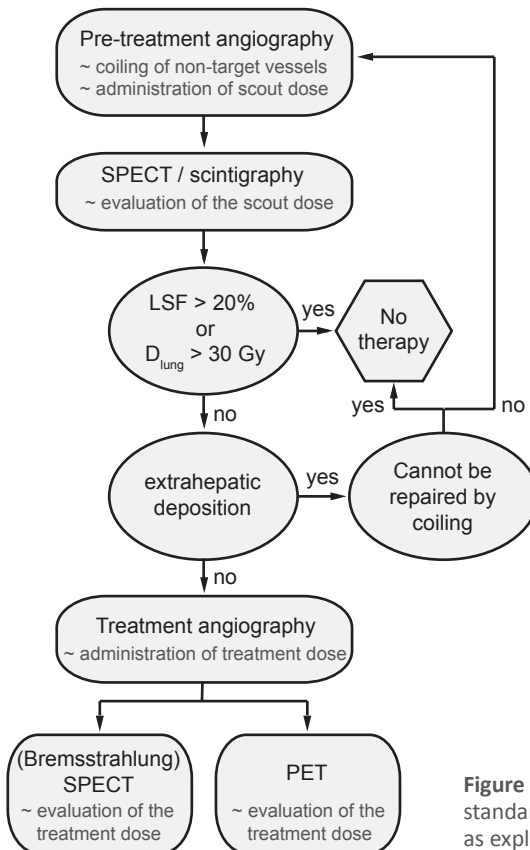


Figure 1.4. A schematic overview of the standardized radioembolization procedure as explained in section 1.5.2.

Treatment planning

The main objective of the work-up angiography is to assess the safety of the radioembolization procedure. Deposition of microspheres in non-target organs is a major risk factor of radioembolization, because it may cause serious complications, including ulceration and bleedings (60,61). Therefore, possible flow to the gastrointestinal tract is evaluated on SPECT(/CT) images of the scout dose distribution. A patient is disqualified for therapy if extrahepatic deposition of ^{99m}Tc -MAA is present that cannot be repaired by catheter embolization techniques (59).

A second major risk factor of radioembolization is radiation-induced pneumonitis, which may be caused by arteriovenous shunting of microspheres to the lungs (62,63). To estimate this risk, the fraction of particles that has shunted to the lungs (LSF) is calculated on (planar) scintigraphic images of the ^{99m}Tc -MAA scout dose (64). Patients with an LSF of higher than 20% are typically disqualified for ^{90}Y radioembolization with resin microspheres (52). For glass microspheres, the estimated dose to the lungs may not be in excess of 30 Gy for a single treatment and 50 Gy for multiple treatments. For this purpose, the dose to lungs (D_{LUNG}) is calculated as

$$D_{\text{LUNG}} (\text{Gy}) = 49.38 (\text{J} / \text{GBq}) \cdot \frac{A_0 (\text{GBq})}{m_{\text{LUNG}} (\text{kg})} \cdot \text{LSF} \quad (1.5)$$

Here, the factor of 49.38 is the total energy released per unit of activity ^{90}Y , m_{LUNG} the lung mass (usually assumed to be 1 kg) and A_0 the ^{90}Y activity planned for administration to the patient (52).

A third major risk factor of radioembolization is severe radiation-induced injury to the functional liver parenchyma, which may lead to radioembolization-induced liver disease (REILD) (54,58). Consequently, the administered ^{90}Y activity should be minutely planned to optimize the balance between liver toxicity and treatment efficacy. Currently, semi-empiric methods are most widely-used for activity planning. For resin microspheres, the ^{90}Y activity is usually calculated by a method that is based on the body-surface-area (BSA) of the patient

$$\text{BSA} (\text{m}^2) = 0.20247 \cdot \text{Height}^{0.725} (\text{m}) \cdot \text{weight}^{0.425} (\text{kg}) \quad (1.6)$$

$$A_0 (\text{GBq}) = \text{BSA} (\text{m}^2) - 0.2 + \frac{V_{\text{TUMOR}} (\text{L})}{V_{\text{LIVER}} (\text{L})} \quad (1.7)$$

Here, V_{TUMOR} and V_{LIVER} are the tumor and liver volume, respectively (52,59). For glass microspheres, planning of the ^{90}Y activity is based on the mean absorbed dose to the whole liver

$$A_0(Gy) = \frac{D_{LIVER}(Gy) \cdot m_{LIVER}(kg)}{49.38(J / GBq)} \quad (1.8)$$

Here, m_{LIVER} is the liver mass and D_{LIVER} the aimed whole liver radiation absorbed dose, which is usually chosen in the range of 100 – 120 Gy (52,59). These semi-empiric methods for activity planning are popular for their simplicity, but are limited by their generality. The use of these simple, minimally patient-specific methods may cause over- or under-treatment in selected patients, because the activity distribution over tumorous and healthy liver tissue, which relates to both treatment efficacy and liver toxicity, is not taken into account (6).

The partition model is a more personalized and scientifically sound method of activity planning (52,65). This method requires partitioning of the liver into tumor and healthy liver (normal) compartments and estimation of the activity concentration ratio (T/N-ratio) over these compartments. After delineation of the tumor and normal liver compartments on anatomical images, mean activity concentrations are obtained from the co-registered SPECT(/CT) images of the ^{99m}Tc -MAA scout dose (6). The T/N ratio is calculated as

$$T / N = \frac{[A]_{TUMOR}}{[A]_{NORMAL}} \quad (1.9)$$

Here, $[A]_{TUMOR}$ and $[A]_{NORMAL}$ are the mean activity concentrations in the tumorous and healthy liver tissue, respectively. Subsequently, the estimated radiation absorbed dose to the normal (D_{NORMAL}) and tumorous liver tissue (D_{TUMOR}) can be separately calculated with the following equations

$$D_{NORMAL}(Gy) = 49.38(J / GBq) \cdot \frac{A_0(Gy) \cdot (1 - LSF)}{m_{NORMAL}(kg) + T / N \cdot m_{TUMOR}(kg)} \quad (1.10)$$

$$D_{TUMOR}(Gy) = T / N \cdot D_{NORMAL}(Gy) \quad (1.11)$$

Here, m_{NORMAL} is the mass of the normal liver compartment and m_{TUMOR} the mass of the tumor compartment (52). By setting a limit to D_{NORMAL} , equation 1.10 can be solved to find the ^{90}Y activity that maximizes the dose to the tumors, while keeping the risk of liver toxicity acceptably low. The maximum tolerated dose to the healthy liver parenchyma is assumed to be in the range of 50 – 70 Gy (66). The partition model is

increasingly recognized as being (scientifically) superior to the semi-empiric methods (55,67-70) and its use is actively encouraged by some experienced physicians (6,66). However, a largely ignored issue is that in some patients the ^{99m}Tc -MAA scout dose distribution differs from the ^{90}Y treatment dose distribution (71), which may be due to differences in particle size, particle shape, particle density, injected particle load, micro-embolic effects, microcatheter tip placement and/or regional blood flow (6,72). In these cases, the T/N ratio is not accurately predicted, which may jeopardize patient safety and treatment efficacy. Replacement of the ^{99m}Tc -MAA particles by more realistic microsphere surrogates, or ideally by exactly the same microspheres as used for the treatment dose, can potentially address this problem.

^{90}Y imaging

Patient safety should be monitored by post-treatment ^{90}Y imaging (52,59), because ^{90}Y microspheres may be unexpectedly deposited in non-target organs, in spite of a safe ^{99m}Tc -MAA scout dose distribution (73,74). Additionally, post-treatment ^{90}Y imaging can be used for dosimetry purposes, if quantitatively accurate. Quantitative images enable calculation of the radiation absorbed dose to tumorous tissue and the healthy liver parenchyma, e.g. by application to the previously described partition model. These values provide insight in treatment efficacy and support selection of patients that potentially benefit from (super-selective) re-treatment with ^{90}Y radioembolization or other forms of adjuvant therapy.

SPECT imaging of the Bremsstrahlung photons, which are produced by interaction of the beta-particles with tissue, has long been considered the only imaging option for ^{90}Y . The quantitative accuracy of clinical Bremsstrahlung SPECT images, however, is limited by the low photon yield, wide energy range, and continuous nature of the ^{90}Y Bremsstrahlung photon spectrum (75). Quantitative ^{90}Y SPECT requires extensive modeling of the image degrading effects in the reconstruction algorithm, since the assumptions with regard to attenuation, scatter, and collimator-detector effects underlying simple photon transport models are not valid, if even applied. Recently, it has been demonstrated that PET imaging of the ^{90}Y distribution is also possible, thanks to a very low and largely overlooked positron branch (76,77). ^{90}Y PET may be an interesting alternative to Bremsstrahlung SPECT, since advanced correction techniques for scatter, random, and attenuation effects are clinically available and can be directly applied (78). Due to the very low positron yield, however, ^{90}Y PET images are prone to deterioration by Poisson noise. Quantitative ^{90}Y Bremsstrahlung SPECT and PET imaging is subject of chapters 2, 3, and 4 of this thesis.

1.5.3 Holmium-166 radioembolization

At the department of Radiology and Nuclear Medicine of the University Medical Center Utrecht, poly(L-lactic acid) microspheres loaded with the combined beta-gamma emitter holmium-166 (^{166}Ho) have been developed as an alternative radioembolization device to ^{90}Y microspheres (79). Recently, the safety and toxicity profile of radioembolization with ^{166}Ho microspheres have been established in patients with liver metastases (80). The possible advantages of ^{166}Ho over ^{90}Y mainly lie in its favorable imaging characteristics; ^{166}Ho emits low-energy gamma photons ($E_\gamma = 81 \text{ keV}$ [$I = 6.7\%$]) in addition to the high-energy beta particles ($E_{\beta,\text{max}} = 1.77 \text{ MeV}$ [$I = 48.7\%$], 1.85 MeV [$I = 50.0\%$]), which can be used for SPECT imaging (81). Furthermore, the high atomic number and highly paramagnetic nature of holmium enable visualization with CT and magnetic resonance imaging (MRI), respectively (82,83). The focus of this thesis is on exploiting the nuclear imaging characteristics of ^{166}Ho . The reader is directed to (84,85) to be educated on the role of the other imaging modalities in ^{166}Ho radioembolization. An overview of the ^{166}Ho microsphere characteristics is listed in Table 1.1.

^{166}Ho imaging

Post-treatment SPECT imaging of the ^{166}Ho microsphere distribution enables monitoring of patient safety and evaluation of the radiation absorbed dose to the tumors and healthy liver. Additionally, ^{166}Ho SPECT may facilitate treatment planning on a scout dose of ^{166}Ho microspheres instead of $^{99\text{m}}\text{Tc}$ -MAA particles. A scout dose of the exact same microspheres instead of microsphere surrogates can potentially improve its predictive value for extrahepatic deposition, lung-shunting, and T/N ratios for partition modeling (86).

All these imaging applications require quantification of the local amount of ^{166}Ho microspheres. However, ^{166}Ho SPECT images are degraded by the relatively high susceptibility of the 81 keV photopeak photons to scatter and attenuation and by the complexity of the ^{166}Ho energy spectrum. In addition to the 81 keV photopeak, the energy spectrum includes multiple high-energy gamma and Bremsstrahlung photon contributions. Furthermore, the characteristic lead X-rays produced in the collimator partially overlap with the ^{166}Ho detection window. Therefore, quantitative ^{166}Ho SPECT reconstruction requires an extensive photon transport model, which includes all of these effects. Quantitative ^{166}Ho SPECT is subject of chapters 2, 5, and 6 of this thesis.

1.6 Outline of this thesis

The research presented in this thesis aims to develop, evaluate, and exploit quantitative nuclear imaging methods for dosimetry in radioembolization. Several radionuclides (viz. ^{99m}Tc , ^{90}Y , and ^{166}Ho), modalities (SPECT and PET), dosimetric purposes (treatment planning and treatment evaluation) and radioembolization devices (^{90}Y microspheres and ^{166}Ho microspheres) have been described in the previous sections. ^{99m}Tc SPECT is used for treatment planning in ^{90}Y and ^{166}Ho radioembolization, ^{90}Y Bremsstrahlung SPECT and PET are of interest for treatment evaluation in ^{90}Y radioembolization, and ^{166}Ho SPECT is employed for both treatment planning and evaluation in ^{166}Ho radioembolization. Each combination of radionuclide and modality requires a specific reconstruction approach to obtain quantitative images, which is reported on in this thesis. In **chapter 2**, the gamma camera imaging characteristics of ^{99m}Tc , ^{90}Y , and ^{166}Ho are quantitatively evaluated and compared, to provide insight in the various image degrading effects that hamper quantitative SPECT. **Chapter 3** presents a quantitative comparison between state-of-the-art clinical ^{90}Y Bremsstrahlung SPECT and PET, which are both used for assessment of the ^{90}Y microsphere distribution after radioembolization. In a phantom study, image contrast, image noise, the ability to detect small accumulations of activity, and the accuracy of radiation absorbed dose estimates, are evaluated to compare the performance of both modalities. Additionally, SPECT and PET-based liver radiation absorbed dose estimates are compared in five patients treated with ^{90}Y radioembolization. **Chapter 4** reports on a novel method for quantitative ^{90}Y Bremsstrahlung SPECT reconstruction, which combines Monte Carlo-based modeling of photon scatter and attenuation with energy- and distance-dependent modeling of the collimator-detector effects. Using phantom experiments and clinical data, the performance of the proposed method is quantitatively evaluated and compared with state-of-the-art clinical ^{90}Y Bremsstrahlung SPECT and ^{90}Y PET technologies. In **chapter 5**, this Monte Carlo-based reconstruction algorithm is adapted for quantitative ^{166}Ho SPECT reconstruction. Its performance is evaluated in comparison with state-of-the-art clinical ^{166}Ho reconstruction algorithms, both in phantom experiments and in clinical practice. In **chapter 6**, quantitative ^{166}Ho SPECT is employed to evaluate the currently used lung dosimetry model for radioembolization, which is based on scintigraphic images of a ^{99m}Tc -MAA scout dose. In patients treated with ^{166}Ho radioembolization, quantitative lung dose measurements are compared between the ^{99m}Tc -MAA scout dose, the ^{166}Ho microsphere scout dose, and the ^{166}Ho microsphere treatment dose.

Chapter 7 provides a summary of the previous chapters and discusses possible future directions of quantitative nuclear imaging and dosimetry in radioembolization.

References

- 1 Mariani G, Bruselli L, Kuwert T et al. A review on the clinical uses of SPECT/CT. *Eur J Nucl Med Mol Imaging*. 2010;37:1959-1985.
- 2 Mitra E, Quon A. Positron Emission Tomography/Computed Tomography: The Current Technology and Applications. *Radiol Clin North Am*. 2009;47:147-160.
- 3 Bailey DL, Willowson KP. An Evidence-Based Review of Quantitative SPECT Imaging and Potential Clinical Applications. *J Nucl Med*. 2013;54:83-89.
- 4 Dewaraja YK, Frey EC, Sgouros G et al. MIRD Pamphlet No. 23: Quantitative SPECT for Patient-Specific 3-Dimensional Dosimetry in Internal Radionuclide Therapy. *J Nucl Med*. 2012;53:1310-1325.
- 5 Kennedy A, Coldwell D, Sangro B, Wasan H, Salem R. Radioembolization for the Treatment of Liver Tumors: General Principles. *Am J Clin Oncol*. 2012;35.
- 6 Kao YH, Tan EH, Ng CE, Goh SW. Clinical implications of the body surface area method versus partition model dosimetry for yttrium-90 radioembolization using resin microspheres: a technical review. *Ann Nucl Med*. 2011;25:455-461.
- 7 Cherry SR, Sorenson JA, Phelps ME. *Physics in Nuclear Medicine*. Philadelphia: Saunders; 2003:290.
- 8 Beekman FJ, Kamphuis C, King MA, van Rijk PP, Viergever MA. Improvement of image resolution and quantitative accuracy in clinical Single Photon Emission Computed Tomography. *Comput Med Imaging Graph*. 2001;25:135-146.
- 9 Compton AH. A quantum theory of the scattering of x-rays by light elements. *Phys Rev*. 1923;21:0483-0502.
- 10 Klein O, Nishina T. Uber die Streuung von Strahlung durch freie Elektronen nach der neuen relativistischen Quantendynamik von Dirac. *Z Physik*. 1929;52:853-868.
- 11 Hutton BF, Buvat I, Beekman FJ. Review and current status of SPECT scatter correction. *Phys Med Biol*. 2011;56:R85-R112.
- 12 Beekman FJ, Kamphuis C, Viergever MA. Improved SPECT quantitation using fully three-dimensional iterative spatially variant scatter response compensation. *IEEE Trans Med Imaging*. 1996;15:491-499.
- 13 Metz CE, Atkins FB, Beck RN. The geometric transfer function component for scintillation camera collimators with straight parallel holes. *Phys Med Biol*. 1980;25:1059-1070.
- 14 Tsui BMW, Hu HB, Gilland DR, Gullberg GT. Implementation of Simultaneous Attenuation and Detector Response Correction in Spect. *IEEE Trans Nucl Sci*. 1988;35:778-783.
- 15 Qi JY, Leahy RM. Iterative reconstruction techniques in emission computed tomography. *Phys Med Biol*. 2006;51:R541-R578.
- 16 Shepp LA, Vardi Y. Maximum Likelihood Reconstruction for Emission Tomography. *IEEE Trans Med Imaging*. 1982;1:113-122.
- 17 Lange K, Carson R. EM reconstruction algorithms for emission and transmission tomography. *J Comput Assist Tomogr*. 1984;8:306-316.
- 18 Hudson HM, Larkin RS. Accelerated Image-Reconstruction Using Ordered Subsets of Projection Data. *IEEE Trans Med Imaging*. 1994;13:601-609.
- 19 Kamphuis C, Beekman FJ, Viergever MA. Evaluation of OS-EM vs. ML-EM for 1D, 2D and fully 3D SPECT reconstruction. *IEEE Trans Nucl Sci*. 1996;43:2018-2024.
- 20 Kamphuis C, Beekman FJ, van Rijk PP, Viergever MA. Dual matrix ordered subsets reconstruction for accelerated 3D scatter compensation in single-photon emission tomography. *Eur J Nucl Med*. 1998;25:8-18.
- 21 Fleming JS. A technique for using CT images in attenuation correction and quantification in SPECT. *Nucl Med Commun*. 1989;10.

- 22 Ogawa K, Harata Y, Ichihara T, Kubo A, Hashimoto S. A practical method for position-dependent Compton-scatter correction in single photon emission CT. *IEEE Trans Med Imaging*. 1991;10:408-412.
- 23 Zeintl J, Vija AH, Yahil A, Hornegger J, Kuwert T. Quantitative Accuracy of Clinical 99mTc SPECT/CT Using Ordered-Subset Expectation Maximization with 3-Dimensional Resolution Recovery, Attenuation, and Scatter Correction. *J Nucl Med*. 2010;51:921-928.
- 24 Frey EC, Tsui BMW. A new method for modeling the spatially-variant, object-dependent scatter response function in SPECT. *Conf Record of IEEE Nuclear Science Symp and Medical Imaging Conf*. 1997;1082-1086.
- 25 Song N, Du Y, He B, Frey EC. Development and evaluation of a model-based downscatter compensation method for quantitative I-131 SPECT. *Med Phys*. 2011;38:3193-3204.
- 26 Beekman FJ, de Jong HW, van GS. Efficient fully 3-D iterative SPECT reconstruction with Monte Carlo-based scatter compensation. *IEEE Trans Med Imaging*. 2002;21:867-877.
- 27 de Wit TC, Xiao JB, Beekman FJ. Monte Carlo-based statistical SPECT reconstruction: Influence of number of photon tracks. *IEEE Trans Nucl Sci*. 2005;52:1365-1369.
- 28 De Jong HWAM, Slijpen ETP, Beekman FJ. Acceleration of Monte Carlo SPECT simulation using convolution-based forced detection. *IEEE Trans Nucl Sci*. 2001;48:58-64.
- 29 De Jong HWAM, Wang WT, Frey EC, Viergever MA, Beekman FJ. Efficient simulation of SPECT down-scatter including photon interactions with crystal and lead. *Med Phys*. 2002;29:550-560.
- 30 Xiao JB, de Wit TC, Staelens SG, Beekman FJ. Evaluation of 3D Monte Carlo-based scatter correction for Tc-99m cardiac perfusion SPECT. *J Nucl Med*. 2006;47:1662-1669.
- 31 Xiao JB, de Wit TC, Zbijewski W, Staelens SG, Beekman FJ. Evaluation of 3D Monte Carlo-based scatter correction for Tl-201 cardiac perfusion SPECT. *J Nucl Med*. 2007;48:637-644.
- 32 Bailey DL. Transmission scanning in emission tomography. *Eur J Nucl Med*. 1998;25:774-787.
- 33 Tsui and MW. The importance and implementation of accurate 3D compensation methods for quantitative SPECT. *Phys Med Biol*. 1994;39:509.
- 34 Cherry S, Dahlbom M. PET: Physics, Instrumentation, and Scanners. In: Phelps M, ed. *PET*. Springer New York; 2006:1-117.
- 35 Adam LE, Zaers J, Ostertag H, Trojan H, Bellemann ME, Brix G. Performance evaluation of the whole-body PET scanner ECAT EXACT HR+ following the IEC standard. *IEEE Trans Nucl Sci*. 1997;44:1172-1179.
- 36 Watson CC. Extension of Single Scatter Simulation to Scatter Correction of Time-of-Flight PET. *IEEE Trans Nucl Sci*. 2007;54:1679-1686.
- 37 Roberto Accorsi and Lars-Eric Adam and Matthew E Werner and Joel. Optimization of a fully 3D single scatter simulation algorithm for 3D PET. *Phys Med Biol*. 2004;49:2577.
- 38 Comtat C, Bataille F, Michel C et al. OSEM-3D reconstruction strategies for the ECAT HRRT. *Conf Record of IEEE Nuclear Science Symp and Medical Imaging Conf*. 2004;6:3492-3496.
- 39 Panin VY, Kehren F, Michel C, Casey M. Fully 3-D PET reconstruction with system matrix derived from point source measurements. *IEEE Trans Med Imaging*. 2006;25:907-921.
- 40 Yamamoto M, Nohara N, Tanaka E et al. Time-of-flight positron imaging and the resolution improvement by an iterative method. *IEEE Trans Nucl Sci*. 1989;36:998-1002.
- 41 Parkin DM, Bray F, Ferlay J, Pisani P. Global cancer statistics, 2002. *CA Canc J Clin*. 2005;55:74-108.
- 42 Yamane B, Weber S. Liver-Directed Treatment Modalities for Primary and Secondary Hepatic Tumors. *Surg Clin North Am*. 2009;89:97.

- 43 Bennett JJ, Cao DC, Posner MC. Determinants of unresectability and outcome of patients with occult colorectal hepatic metastases. *J Surg Oncol.* 2005;92:64-69.
- 44 Pawlik TM, Choti MA. Surgical therapy for colorectal metastases to the liver. *J Gastrointest Surg.* 2007;11:1057-1077.
- 45 Edeline J, Raoul JL, Vauleon E, Guillygomach A, Boudjema K, Boucher E. Systemic chemotherapy for hepatocellular carcinoma in non-cirrhotic liver: A retrospective study. *World J Gastroenterol.* 2009;15:713-716.
- 46 Adam R, Wicherts DA, de Haas RJ et al. Patients With Initially Unresectable Colorectal Liver Metastases: Is There a Possibility of Cure? *J Clin Oncol.* 2009;27:1829-1835.
- 47 Feng M, Ben-Josef E. Radiation Therapy for Hepatocellular Carcinoma. *Semin Radiat Oncol.* 2011;21:271-277.
- 48 Schefter TE, Kavanagh BD. Radiation Therapy for Liver Metastases. *Semin Radiat Oncol.* 2011;21:264-270.
- 49 Cromheecke M, Konings AWT, Szabo BG, Hoekstra HJ. Liver tissue tolerance for irradiation: Experimental and clinical investigations. *Hepatogastroenterology.* 2000;47:1732-1740.
- 50 Breedis C, Young G. The Blood Supply of Neoplasms in the Liver. *Am J Pathol.* 1954;30:969-985.
- 51 Bierman HR, Byron RL, Jr., Kelley KH, Grady A. Studies on the blood supply of tumors in man. III. Vascular patterns of the liver by hepatic arteriography in vivo. *J Natl Cancer Inst.* 1951;12:107-131.
- 52 Dezarn WA, Cessna JT, Dewerd LA et al. Recommendations of the American Association of Physicists in Medicine on dosimetry, imaging, and quality assurance procedures for Y-90 microsphere brachytherapy in the treatment of hepatic malignancies. *Med Phys.* 2011;38:4824-4845.
- 53 Lewandowski RJ, Sato KT, Atassi B et al. Radioembolization with Y-90 microspheres: Angiographic and technical considerations. *Cardiovasc Intervent Radiol.* 2007;30:571-592.
- 54 Kennedy AS, McNeillie P, Dezarn WA et al. Treatment Parameters and Outcome in 680 Treatments of Internal Radiation With Resin 90Y-Microspheres for Unresectable Hepatic Tumors. *Int J Radiat Oncol Biol Phys.* 2009;74:1494-1500.
- 55 Hendlisz A, Van den Eynde M, Peeters M et al. Phase III Trial Comparing Protracted Intravenous Fluorouracil Infusion Alone or With Yttrium-90 Resin Microspheres Radioembolization for Liver-Limited Metastatic Colorectal Cancer Refractory to Standard Chemotherapy. *J Clin Oncol.* 2010;28:3687-3694.
- 56 Vente MA, Wondergem M, van der Tweel I et al. Yttrium-90 microsphere radioembolization for the treatment of liver malignancies: a structured meta-analysis. *Eur Radiol.* 2009;19:951-959.
- 57 Gulec SA, Pennington K, Wheeler J et al. Yttrium-90 Microsphere-selective Internal Radiation Therapy With Chemotherapy (Chemo-SIRT) for Colorectal Cancer Liver Metastases: An In Vivo Double-Arm-Controlled Phase II Trial. *Am J Clin Oncol.* 2012; Publish Ahead of Print.
- 58 Coldwell D, Sangro B, Salem R, Wasan H, Kennedy A. Radioembolization in the Treatment of Unresectable Liver Tumors Experience Across a Range of Primary Cancers. *Am J Clin Oncol.* 2012;35:167-177.
- 59 Kennedy AS, Nag S, Salem R et al. Recommendations for radioembolization of hepatic malignancies using yttrium-90 microsphere brachytherapy: A consensus panel report from the Radioembolization Brachytherapy Oncology Consortium. *Int J Radiat Oncol Biol Phys.* 2007;68:13-23.
- 60 Murthy R, Brown DB, Salem R et al. Gastrointestinal complications associated with hepatic arterial yttrium-90 microsphere therapy. *J Vasc Intervent Radiol.* 2007;18:553-562.

- 61 Riaz A, Lewandowski RJ, Kulik LM et al. Complications Following Radioembolization with Yttrium-90 Microspheres: A Comprehensive Literature Review. *J Vasc Intervent Radiol.* 2009;20:1121-1130.
- 62 Leung TWT, Lau WY, Ho SKW et al. Radiation Pneumonitis After Selective Internal Radiation Treatment with Intraarterial (90)Yttrium-Microspheres for Inoperable Hepatic-Tumors. *Int J Radiat Oncol Biol Phys.* 1995;33:919-924.
- 63 Dancey JE, Shepherd FA, Paul K et al. Treatment of nonresectable hepatocellular carcinoma with intrahepatic Y-90-microspheres. *J Nucl Med.* 2000;41:1673-1681.
- 64 Ho S, Lau WY, Leung TW, Chan M, Johnson PJ, Li AK. Clinical evaluation of the partition model for estimating radiation doses from yttrium-90 microspheres in the treatment of hepatic cancer. *Eur J Nucl Med.* 1997;24:293-298.
- 65 Ho S, Lau WY, Leung TW et al. Partition model for estimating radiation doses from yttrium-90 microspheres in treating hepatic tumours. *Eur J Nucl Med.* 1996;23:947-952.
- 66 Lau WY, Kennedy AS, Kim YH et al. Patient Selection and Activity Planning Guide for Selective Internal Radiotherapy with Yttrium-90 Resin Microspheres. *Int J Radiat Oncol Biol Phys.* 2012;82:401-407.
- 67 Campbell JM, Wong CO, Muzik O, Marples B, Joiner M, Burmeister J. Early dose response to yttrium-90 microsphere treatment of metastatic liver cancer by a patient-specific method using single photon emission computed tomography and positron emission tomography. *Int J Radiat Oncol Biol Phys.* 2009;74:313-320.
- 68 Kao YH, Tan AEH, Burgmans MC et al. Image-Guided Personalized Predictive Dosimetry by Artery-Specific SPECT/CT Partition Modeling for Safe and Effective Y-90 Radioembolization. *J Nucl Med.* 2012;53:559-566.
- 69 Garin E, Lenoir L, Rolland Y et al. Dosimetry Based on Tc-99m-Macroaggregated Albumin SPECT/CT Accurately Predicts Tumor Response and Survival in Hepatocellular Carcinoma Patients Treated with Y-90-Loaded Glass Microspheres: Preliminary Results. *J Nucl Med.* 2012;53:255-263.
- 70 Flamen P, Vanderlinden B, Delatte P et al. Multimodality imaging can predict the metabolic response of unresectable colorectal liver metastases to radioembolization therapy with Yttrium-90 labeled resin microspheres. *Phys Med Biol.* 2008;53:6591-6603.
- 71 Knesaurek K, Machac J, Muzinic M, DaCosta M, Zhang Z, Heiba S. Quantitative comparison of yttrium-90 (90Y)-microspheres and technetium-99m (99mTc)-macroaggregated albumin SPECT images for planning 90Y therapy of liver cancer. *Technol Cancer Res Treat.* 2010;9:253-262.
- 72 Van de Wiele C, Maes A, Brugman E et al. SIRT of liver metastases: physiological and pathophysiological considerations. *Eur J Nucl Med Mol Imaging.* 2012;39:1646-1655.
- 73 Gupta A, Gill A, Shrikanthan S, Srinivas S. Nontargeted Y-90 Microsphere Radioembolization to Duodenum Visualized on Y-90 PET/CT and Bremsstrahlung SPECT/CT. *Clin Nucl Med.* 2012;37:98-99.
- 74 Ahmadzadehfar H, Muckle M, Sabet A et al. The significance of Bremsstrahlung SPECT-CT of the Abdomen after Yttrium 90 microsphere selective internal radiation treatment (SIRT) in the early Diagnosis of SIRT-Induced Extrahepatic Side Effects. *Eur J Nucl Med Mol Imaging.* 2010;37:S264.
- 75 Shen S, DeNardo GL, Yuan A, DeNardo DA, DeNardo SJ. Planar gamma camera imaging and quantitation of yttrium-90 bremsstrahlung. *J Nucl Med.* 1994;35:1381-1389.
- 76 Lhommel R, van Elmbt L, Goffette P et al. Feasibility of Y-90 TOF PET-based dosimetry in liver metastasis therapy using SIR-Spheres. *Eur J Nucl Med Mol Imaging.* 2010;37:1654-1662.
- 77 Langhoff H, Hennies HH. Zum Experimentellen Nachweis Von Zweiquantenerfall Beim 0+-0+-Ubergang des Zr90. *Z Phys.* 1961;164:166-173.

- 78 van Elmbt L, Walrand S, Lhommel R, Jamar F, Pauwels S. Quantitative comparison between LYSO and BGO PET-tomographs in 90Y imaging. *Eur J Nucl Med Mol Imaging*. 2010;37:S293.
- 79 Nijsen JF, Zonnenberg BA, Woittiez JR et al. Holmium-166 poly lactic acid microspheres applicable for intra-arterial radionuclide therapy of hepatic malignancies: effects of preparation and neutron activation techniques. *Eur J Nucl Med*. 1999;26:699-704.
- 80 Smits MLJ, Nijsen JFW, van den Bosch MAAJ et al. Holmium-166 radioembolisation in patients with unresectable, chemorefractory liver metastases (HEPAR trial): a phase 1, dose-escalation study. *Lancet Oncol*. 2012;13:1025-1034.
- 81 de Wit TC, Xiao J, Nijsen JF et al. Hybrid scatter correction applied to quantitative holmium-166 SPECT. *Phys Med Biol*. 2006;51:4773-4787.
- 82 Seppenwoolde JH, Nijsen JF, Bartels LW, Zielhuis SW, van het Schip AD, Bakker CJ. Internal radiation therapy of liver tumors: qualitative and quantitative magnetic resonance imaging of the biodistribution of holmium-loaded microspheres in animal models. *Magn Reson Med*. 2005;53:76-84.
- 83 Seevinck PR, Seppenwoolde JH, de Wit TC et al. Factors affecting the sensitivity and detection limits of MRI, CT, and SPECT for multimodal diagnostic and therapeutic agents. *Anticancer Agents Med Chem*. 2007;7:317-334.
- 84 Seevinck PR. Multimodal imaging of holmium-loaded microspheres for internal radiation therapy [dissertation]. Utrecht University, The Netherlands. 2009.
- 85 van de Maat GH. Magnetic resonance imaging in Ho-166 liver radioembolization [dissertation]. Utrecht University, The Netherlands. 2013.
- 86 Vente MA, de Wit TC, van den Bosch MA et al. Holmium-166 poly(L-lactic acid) microsphere radioembolisation of the liver: technical aspects studied in a large animal model. *Eur Radiol*. 2010;20:862-869.

Chapter 2

**Quantitative evaluation of scintillation camera imaging
characteristics of radionuclides used in liver radioembolization**



Published as:

M. Elschot, J.F.W. Nijssen, A.J. Dam, H.W.A.M. de Jong. Quantitative evaluation of scintillation camera imaging characteristics of isotopes used in liver radioembolization. *PLoS ONE*. 2011;6:e26174

Abstract

Objectives

Scintillation camera imaging is used for treatment planning and post-treatment dosimetry in liver radioembolization (RE). In yttrium-90 (^{90}Y) RE, scintigraphic images of technetium-99m ($^{99\text{m}}\text{Tc}$) are used for treatment planning, while ^{90}Y Bremsstrahlung images are used for post-treatment dosimetry. In holmium-166 (^{166}Ho) RE, scintigraphic images of ^{166}Ho can be used for both treatment planning and post-treatment dosimetry. The aim of this study is to quantitatively evaluate and compare the imaging characteristics of these three radionuclides, in order that imaging protocols can be optimized and RE studies with varying radionuclides can be compared.

Methods

Phantom experiments were performed in line with NEMA guidelines to assess the spatial resolution, sensitivity, count rate linearity, and contrast recovery of $^{99\text{m}}\text{Tc}$, ^{90}Y and ^{166}Ho . In addition, Monte Carlo simulations were performed to obtain detailed information about the history of detected photons.

Results

The use of a broad energy window and the high-energy collimator gave optimal combination of sensitivity, spatial resolution, and primary photon fraction for ^{90}Y Bremsstrahlung imaging, although differences with the medium-energy collimator were small. For ^{166}Ho , the high-energy collimator also slightly outperformed the medium-energy collimator. In comparison with $^{99\text{m}}\text{Tc}$, the image quality of both ^{90}Y and ^{166}Ho is degraded by a lower spatial resolution, a lower sensitivity, and larger scatter and collimator penetration fractions.

Conclusions

The quantitative evaluation of the scintillation camera characteristics presented in this study helps to optimize acquisition parameters and supports future analysis of clinical comparisons between RE studies.

2.1 Introduction

Intra-arterial liver radioembolization (RE) using microspheres loaded with a high-energy beta emitting radionuclide, is an emerging technique for radiation treatment of patients with unresectable liver tumors (1,2). RE leads to high tumor absorbed radiation doses, while the surrounding healthy liver tissue is spared (3). RE is generally a two-step procedure, consisting of i) the administration of a small amount of activity, the scout dose, and ii) subsequent administration of the activity that is expected to have a therapeutic effect, the treatment dose. The spatial distribution of the scout dose is expected to represent the distribution of the treatment dose, and can consequently be used to predict safety of the procedure.

The spatial distribution of the scout and treatment dose is commonly assessed using scintillation camera imaging. Following administration of the scout dose, the patient undergoes single photon emission computed tomography (SPECT) to detect extrahepatic deposition of activity, which is a contra-indication for therapy, and planar scintillation camera imaging to determine the percentage of activity that shunted to the lungs. A high lung-shunting (LS) percentage provokes reduction of the treatment dose ($10\% < LS < 20\%$ (SIR-Spheres package insert; Sirtex Medical, Sydney, Australia)) or even cancellation of therapy ($LS > 20\%$). After treatment, a SPECT scan of the treatment dose is usually acquired to confirm absence of extrahepatic activity. This scan can also be used to retrospectively assess a dose-response relation.

The beta-emitter yttrium-90 (^{90}Y , Table 2.1) is most frequently used for RE. Its distribution can be assessed by means of SPECT imaging of the Bremsstrahlung photons (4-7). Unfortunately, the continuous Bremsstrahlung energy spectrum comprises photon energies ranging up to 2 MeV, and is therefore associated with poor image quality (6). For this reason, Technetium-99m-labeled macroaggregated albumin particles ($^{99\text{m}}\text{Tc-MAA}$) are generally used for the scout dose, as a substitute for the ^{90}Y microspheres, since the image quality is much better (8,9). The $^{99\text{m}}\text{Tc-MAA}$ particles, however, differ in shape, size, density and quantity from the ^{90}Y microspheres, potentially affecting the spatial distribution of the scout dose (10,11). Furthermore, the instability of $^{99\text{m}}\text{Tc-MAA}$ particles frequently leads to uptake of dissociated $^{99\text{m}}\text{Tc-pertechnetate}$ in the thyroid and gastrointestinal tract (12), and to shunting of smaller and disintegrated particles to the lungs (13), which altogether may cause false adjustment of the ^{90}Y treatment dose. As a potential alternative to ^{90}Y microspheres, holmium-166 (^{166}Ho , Table 2.1) loaded microspheres are currently investigated in a clinical study (14-18). The higher specific activity and shorter half life

may have a beneficial impact on tumor kill. Additionally, the imaging characteristics of ^{166}Ho are believed to be more suitable for quantitative imaging than ^{90}Y , because it is a combined beta-gamma emitter (19,20). ^{166}Ho microspheres may conceivably be used for both the scout dose and the treatment dose, which potentially improves the predictive value of the scout dose distribution and post-treatment liver dosimetry.

Scintillation camera images of $^{99\text{m}}\text{Tc}$, ^{90}Y , and ^{166}Ho are all used for clinical assessment of the activity distribution in liver RE, but they have differing imaging characteristics. In contrast to $^{99\text{m}}\text{Tc}$, information on the scintillation camera imaging characteristics of ^{90}Y and ^{166}Ho is sparse, and a systematical comparison between these three radionuclides does not exist. Therefore, the aim of this study is to provide a systematical evaluation and comparison of the scintillation camera imaging characteristics of ^{90}Y , ^{166}Ho and $^{99\text{m}}\text{Tc}$, using a series of phantom experiments and Monte Carlo simulations. This is important for (future) clinical comparisons between microsphere RE studies with varying radionuclides and imaging protocols. In addition, the outcome of this study can be used to optimize the acquisition settings for ^{90}Y and ^{166}Ho imaging, and to guide future developments in SPECT image reconstruction.

2.2 Materials and Methods

The spatial resolution, sensitivity, count rate linearity, and contrast recovery of $^{99\text{m}}\text{Tc}$, ^{90}Y , and ^{166}Ho were evaluated by means of phantom experiments. If possible, the well-defined National Electrical Manufacturers Association (NEMA) 2007 guidelines were adopted, facilitating (future) comparison with other radionuclides and acquisition protocols (21,22). In addition, Monte Carlo simulations were performed to yield data that cannot be retrieved from physical experiments, including the fractions of primary photons, scattered photons, and collimator-penetrated photons of the line source measurements.

2.2.1 Phantom experiments

Data was acquired with a Philips FORTE™ dual-headed camera with 3/8 inch thick thallium-doped sodium-iodide (NaI(Tl)) crystals. $^{99\text{m}}\text{Tc}$ measurements were performed with the low-energy general purpose (VXGP) collimator. Medium-energy (MEGP) and high-energy general purpose (HEGP) collimators were mounted for the ^{90}Y and ^{166}Ho measurements, to reduce collimator penetration of high-energy photons. The energy window settings for ^{90}Y Bremsstrahlung imaging vary between institutions, ranging from small windows with a relatively low central energy (23,24),

to intermediate (5,7) and broad energy windows (4,6,25-27). Although it is generally believed that a wide energy window is required to maintain sufficient sensitivity, no consensus exists on the optimal central energy and window width. Therefore, both a broad 50-250 keV window, which optimizes sensitivity, and a smaller 120-250 keV window, which is expected to have less scatter contamination, were evaluated in this study. The used energy window settings and collimator characteristics are listed in Table 2.1 and 2.2, respectively.

Table 2.1. Radionuclide characteristics and measurement settings.

Radionuclide	Half-life (h)	$E_{\beta\max}$ (MeV) ^a	E_{γ} (keV) ^b	E_{win} (keV) ^c	Collimator
^{99m} Tc	6.0	N/A	140.5 (89%)	130–151	VXGP
⁹⁰ Y	64.1	2.28 (99.9%)	Bremsstrahlung	120–250	MEGP
				50–250	HEGP
¹⁶⁶ Ho	26.8	1.77 (48.7%)	80.6 (6.7%)	74.6–86.6	MEGP
		1.85 (50.0%)	1379.4 (0.9%)		HEGP
			1581.0 (0.2%)		

^a $E_{\beta\max}$ represents the maximum energy and abundance of the beta particles

^b E_{γ} represents the gamma photon energy and abundance

^c E_{win} represents the lower and upper limits of the energy window

Table 2.2. Collimator characteristics. All collimators have hexagonal hole shapes.

Collimator	Hole size (mm)	Septal thickness (mm)	Length (mm)
VXGP	1.78	0.152	42
MEGP	2.95	1.143	48
HEGP	3.81	1.727	60

Spatial resolution

Spatial resolution defines whether small accumulations of activity, e.g. in or around tumors, can be detected and quantified. Projection images (matrix = 256 x 256, pixelsize = 2.332 x 2.332 mm²) of a 28 cm long line source with an inner diameter of 2 mm were acquired. To create realistic conditions with regard to electron absorption, and (Bremsstrahlung) photon emission and scatter, the line source was centered in 2, 10, and 20 cm of poly(methyl methacrylate) (PMMA), leading to 1, 5, and 10 cm of scatter material below and on top of the source. Measurements were performed with a source to collimator distance of 2, 6 and 11 cm for 1 cm of scatter material and 11 cm for the measurements with 5 and 10 cm of scatter material (Figure 2.1). The central lines perpendicular to the source were summed over a distance of 10 cm to obtain the line spread function (LSF). The full width at half maximum (FWHM) and the full width at tenth maximum (FWTM) of the LSF were determined according to NEMA guidelines.

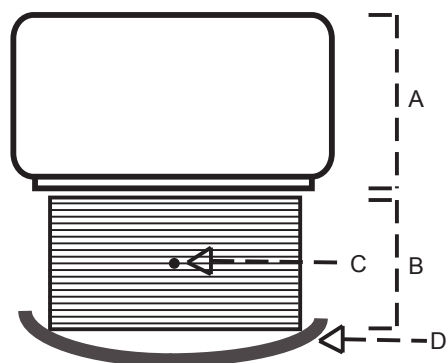


Figure 2.1. Schematic overview of the spatial resolution measurement of the line-source centered in 20 cm PMMA. Shown are the camera, including the collimator (A), a stack of 20 PMMA slabs of size 40x40x1 cm (B), the location of the line-source (C), and the patient bed (D). The line-source to collimator-face distance is 11 cm.

Sensitivity

The imaging sensitivity of a radionuclide is directly related to the image noise, which can be important for detection of small amounts of extrahepatic activity. As described by NEMA, a Petri dish was filled with a thin layer of activity, which was beforehand measured with a calibrated dose calibrator. The dish was placed in the center of the field-of-view of the camera, at a distance of 10 cm and 40 cm from the collimator. To ensure stopping all electrons and proper creation of the Bremsstrahlung photons, 1 cm thick PMMA slabs were placed below and on top of the dish for the ^{90}Y and ^{166}Ho sensitivity measurements. In each measurement, 4 million counts were acquired. The sensitivity (S) (cps Mbq^{-1}) was calculated as the total number of counts in the field-of-view, divided by acquisition time times activity.

To enable calculation of the system count-rate linearity, described in the next section, the sensitivity measurements were simultaneously acquired in two energy windows: the regular photopeak energy window, and an energy window covering the complete energy range of the camera ('full-energy-window').

Count rate linearity

In RE, treatment doses up to several GBqs are typically administered to the patient. These high activities can lead to detector dead-time and, consequently, to underestimation of the dose. This effect is described by the system count rate curve, that depends on i) the system sensitivity, which is determined by the number of photons that pass the collimator and fall within the energy window, and ii) the dead-time, which depends on the total number of photons that hit the crystal. The first can be measured as described in the 'sensitivity' section. The latter is theoretically described by Sorensen's count rate model for paralyzable scintillation cameras (28) and can be provided by the intrinsic count rate measurements described here.

Cylindrical vials with an inner diameter of 2.4 cm were filled with the radionuclides solved in 11 ml water. Activities ranged from 0.5-24.5 MBq for ^{99m}Tc , 16.9-350.8 MBq for ^{90}Y and 5.0-121.1 MBq for ^{166}Ho , to include count rates from the linear range to count rates that cause dead-time effects. The vials were placed in the center of the field-of-view of the camera, at 66.5 cm from the detector, resulting in a uniform photon flux on the detector. The acquisition time was 10 minutes and the energy window was set to the full-energy-window, yielding an intrinsic count rate (cps) comprised of all photons that hit the detector.

From the intrinsic count rate curve (measured in the full-energy-window), the system sensitivity in the full-energy-window, and the system sensitivity in the photopeak window, the system count rate in the photopeak window can be calculated for each radionuclide and collimator and plotted as a function of activity. The reported maximum activity with linear count rate response (A_{linmax}) was defined as the highest activity with less than 2% loss of count rate. The corresponding maximum achievable linear count rate (R_{linmax}) was also reported.

Contrast recovery

Contrast recovery is important if quantification of local accumulation of activity is required, as is the case with image based tumor dosimetry in RE. Contrast recovery was determined using a fillable torso-shaped NEMA image quality phantom (volume = 9700 ml) containing six fillable coplanar spheres (inner diameter = 10, 13, 17, 22, 28, and 37 mm). Lung tissue was simulated by a central cylindrical lung insert. The phantom background activity concentrations and SPECT scan times were matched to obtain the total number of counts corresponding to a 30 minutes SPECT scan with clinically realistic liver activity concentrations: 137 kBq ml⁻¹, 573 kBq ml⁻¹, and 166 kBq ml⁻¹, for ^{99m}Tc , ^{90}Y , and ^{166}Ho , respectively, and a sphere-to-background activity concentration ratio (R) of 9:1. These activity concentrations were based on a scout dose for ^{99m}Tc and ^{166}Ho , and a treatment dose for ^{90}Y . SPECT data was acquired in 120 projections over a 360° orbit. Volumes were reconstructed using filtered back projection (FBP), on a 128 x 128 x 128 grid with an isotropic voxel size of 4.664 mm. No additional filtering other than the ramp filter was applied. Post-reconstruction, images were corrected for attenuation using the Chang algorithm with a non-uniform effective broad beam linear attenuation coefficient. Contrast recovery coefficients (Q_H) were calculated in accordance with NEMA guidelines. An example of the filled phantom with hot sphere and background regions of interest (ROI) is given in Figure 2.2.

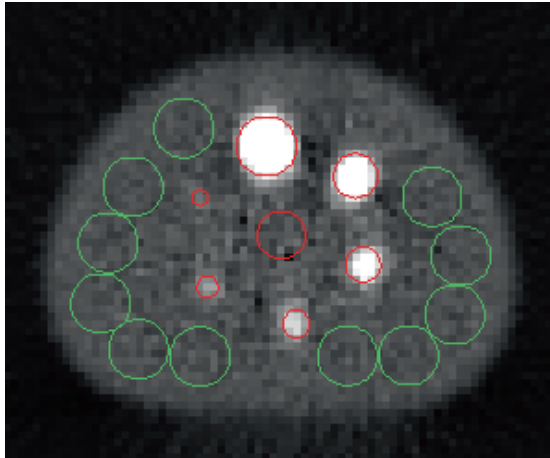


Figure 2.2. Overview of the hot sphere and background ROI. The slice through the center of the spheres of the contrast recovery phantom filled with ^{99m}Tc is shown. Overlaid are the locations of the lung insert (central red ROI), the hot sphere ROI (peripheral red ROI), and 11 of the 55 background ROI of the largest sphere (green ROI).

2.2.2 Monte Carlo simulations

Monte Carlo simulations were performed with the well validated general purpose Monte Carlo radiation transport code *mcnp* 2.5.0 (29). The camera head was modeled realistically including collimator housing, collimator, aluminum crystal housing, NaI(Tl) crystal, 5 cm of crown glass mimicking the backscatter compartments, and lead shielding. Both gamma photon (for ^{99m}Tc and ^{166}Ho) and Bremsstrahlung photon (for ^{90}Y and ^{166}Ho) contributions were simulated. The mono-energetic gamma photons were simulated weighted by their relative abundance as given in Table 2.1. Only 2.0% of the ^{90}Y and 1.2% of the ^{166}Ho beta emissions lead to Bremsstrahlung photons with an energy higher than 50 keV. Therefore, the Bremsstrahlung photons were sampled from a predefined energy spectrum and source distribution, similar to the approach published by Rault et al (30), which improved the efficiency of the simulations substantially.

Primary, scatter, and penetration fraction

Monte Carlo simulations were performed to estimate the fractions of primary (PF), scattered (SF) and collimator-penetrated (CPF) photons. Since high SF and CPF have deteriorating effects on the image quality, their characterizations give insight into the effectiveness of the chosen collimator and energy window. The geometry of the simulations was equal to the geometry of measurements of the line source centered in 20 cm PMMA, shown in Figure 2.1. A detected photon was defined as a photon that deposited at least part of its energy in the crystal, sub-divided in three groups:

- i) Primary photons: detected photons that did not interact with material or penetrate through the collimator.
- ii) Scattered photons: detected photons that scattered in the PMMA, photons that scattered in the camera-housing or detector, and photons that were created in the collimator (lead x-rays). None of these photons penetrated the collimator.
- iii) Penetrated photons: all detected photons (unscattered or scattered) that penetrated through the collimator.

The number of photons released was 300 million for both gamma photon and Bremsstrahlung photon simulations. Equal to the spatial resolution measurements, the central lines perpendicular to the source were summed over a distance of 10 cm to obtain the LSF. The total ^{166}Ho LSF was calculated as the abundance weighted summation of gamma and Bremsstrahlung photon contributions. The experimental and simulated LSF measurements were compared visually.

2.3 Results

2.3.1 Phantom experiments

Spatial resolution

Table 2.3 lists the FWHM and FWTM in mm of the measured LSF for the three radionuclides. In both energy windows, the ^{90}Y LSF showed smaller FWHM and FWTM for the HEGP than for the MEGP collimator. The FWHM were slightly smaller for the 120-250 keV window than for the 50-250 keV window, but the FWTM were substantially larger. For ^{166}Ho , the HEGP collimator yielded a higher resolution than the MEGP collimator, as can be appreciated by the slightly smaller FWHM, and substantially smaller FWTM, for all measurements.

Table 2.3. Spatial resolution given as the FWHM (FWTM) in mm. S01D02 corresponds to the measurement with 1 cm of scatter material and line-source to collimator distance of 2 cm, S01D06 to the measurement with 1cm of scatter material and line-source to collimator distance of 6 cm, etc.

	^{99m} Tc	⁹⁰ Y 120-250 keV		⁹⁰ Y 50-250 keV		¹⁶⁶ Ho	
	VXGP	MEGP	HEGP	MEGP	HEGP	MEGP	HEGP
S01D02	5.4 (10.4)	11.5 (173.7)	7.0 (113.1)	10.9 (123.2)	7.5 (49.2)	11.1 (61.7)	6.5 (17.2)
S01D06	6.6 (12.3)	12.9 (222.2)	11.0 (137.2)	11.4 (149.7)	11.1 (60.2)	11.7 (42.2)	10.5 (21.5)
S01D11	8.2 (15.0)	17.1 (286.1)	15.3 (160.0)	15.8 (172.9)	15.4 (57.6)	14.7 (35.8)	14.1 (25.4)
S05D11	8.4 (16.6)	19.7 (300.6)	16.4 (218.9)	19.4 (235.7)	17.0 (159.3)	15.8 (97.0)	14.6 (43.5)
S10D11	8.5 (17.4)	28.1 (341.2)	18.1 (269.5)	26.3 (294.9)	20.1 (241.3)	15.6 (168.3)	14.9 (113.7)

Sensitivity

The planar sensitivities, measured at a distance of 10 and 40 cm from the collimator face, are listed in Table 2.4. As was expected from the photon abundances, the ^{99m}Tc sensitivity was higher than the ¹⁶⁶Ho sensitivity. The ⁹⁰Y sensitivity was lower than ¹⁶⁶Ho sensitivity for both energy windows. No difference was observed between the ^{99m}Tc sensitivities at 10 cm and 40 cm, indicating proper collimation of the photons. To the contrary, the sensitivity for both ⁹⁰Y and ¹⁶⁶Ho decreased at a larger distance from the collimator, due to collimator penetration effects. This effect was larger for the MEGP collimator than for the HEGP collimator.

Table 2.4. Sensitivity in counts per second per unit activity.

	^{99m} Tc	⁹⁰ Y 120-250 keV		⁹⁰ Y 50-250 keV		¹⁶⁶ Ho	
	VXGP	MEGP	HEGP	MEGP	HEGP	MEGP	HEGP
S - 10 cm (cps MBq ⁻¹)	63.8	6.0	3.1	10.5	6.0	12.6	10.6
S - 40 cm (cps MBq ⁻¹)	63.1	3.0	1.8	6.0	4.9	9.9	8.2

Count rate linearity

Figure 2.3 A shows the observed intrinsic count rate as a function of the ideal count rate for all radionuclides. As expected, this intrinsic count rate curve did not depend on the radionuclide imaged and was fitted well by Sorensen's count rate model of paralyzable scintillation cameras (28). Figure 2.3 B shows the system count rate curves for all radionuclides and measurement settings, estimated from the intrinsic count rate curve and the system sensitivities. A_{linmax} and R_{linmax} are listed in Table 2.5. The A_{linmax} of approximately 1.5 GBq for ¹⁶⁶Ho might be a limitation for scintillation camera imaging directly after treatment. The quantitative accuracy of imaging the ^{99m}Tc-MAA scout dose (~ 150 MBq), ¹⁶⁶Ho scout dose (~ 250 MBq), and ⁹⁰Y treatment dose (~ 1-3 GBq) in the clinical range will not be affected by dead-time effects.

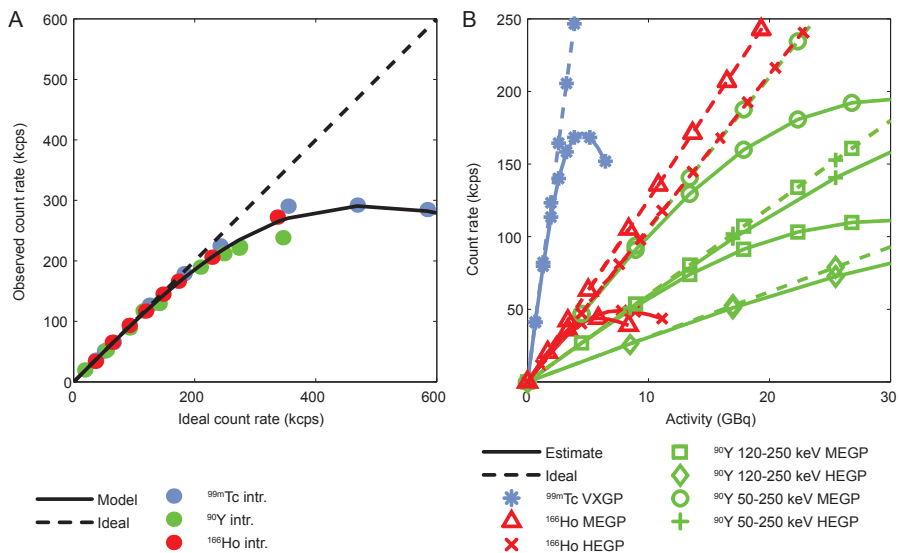


Figure 2.3. Intrinsic and system count rate linearity curves. (A) The observed count rate is plotted as a function of ideal count rate. Sorensen’s count rate model for paralyzable cameras (solid line) is fitted to the intrinsic count rate measurements (data points). The ideal camera count rate response, without dead-time effects, is plotted by the dashed line. (B) Shown are the system count rate curves (solid lines), composed of the intrinsic count rate linearity curve and the system sensitivity measurements. The slope of the ideal system camera count rate response (dashed lines) corresponds to the system sensitivity.

Table 2.5. Estimated maximum activity in the linear detection range and corresponding estimated maximum linear count rate.

	^{99m} Tc		⁹⁰ Y 120-250 keV		⁹⁰ Y 50-250 keV		¹⁶⁶ Ho	
	VXGP	MEGP	HEGP	MEGP	HEGP	MEGP	HEGP	
A _{linmax} (MBq)	1095	7595	14430	7595	14430	1420	1891	
R _{linmax} (kcps)	68	45	44	78	85	18	20	

Contrast recovery

Figure 2.4 shows the slice through the centers of the spheres of all FBP reconstructed images. In Figure 2.5, contrast recovery coefficients are shown as a function of sphere diameter. The ^{99m}Tc contrast recovery was 59% for the largest sphere. For ⁹⁰Y and ¹⁶⁶Ho, this was 17% and 35%, respectively. Neither collimator choice, nor energy window choice affected the ⁹⁰Y contrast recovery much. Also, no difference was observed between the MEGP and HEGP ¹⁶⁶Ho contrast recovery curves.

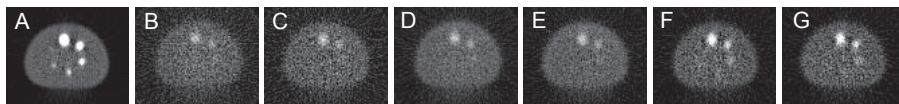


Figure 2.4. FBP reconstructed images of the contrast recovery phantom. The slices through the center of the spheres of the contrast recovery phantom are shown for ^{99m}Tc and VXGP (A), ^{90}Y 120-250 keV and MEGP (B), ^{90}Y 120-250 keV and HEGP (C), ^{90}Y 50-250 keV and MEGP (D), ^{90}Y 50-250 keV and HEGP (E), ^{166}Ho and MEGP (F), and ^{166}Ho and HEGP (G). All images were linearly window-levelled from 0 to 4 times the average background intensity.

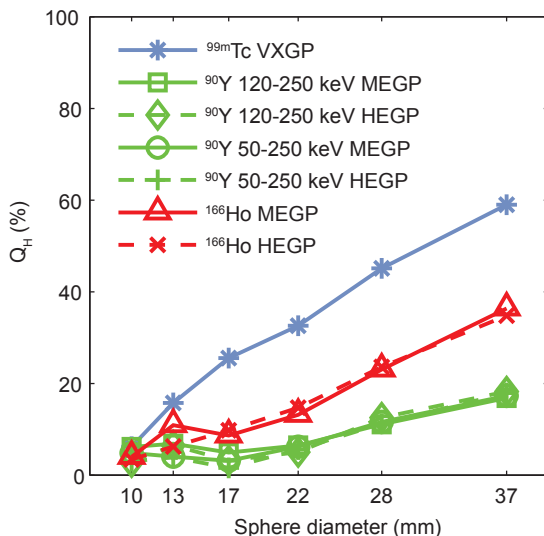


Figure 2.5. Contrast recovery as a function of sphere diameter. Q_H is the recovery of sphere-to-background contrast in the measurement, as compared to the true contrast in the phantom.

2.3.2 Monte Carlo simulations

Primary, scatter, and penetration fraction

The measured and simulated LSF of the line source centered in 20 cm PMMA are shown in Figure 2.6. The good agreement between both the center and the tails confirms the accuracy of the Monte Carlo simulations. The simulated LSF were subdivided in the three different photon classification groups. Table 2.6 lists the PF, SF and CPF of each radionuclide. For both ^{90}Y and ^{166}Ho , the HEGP collimator yielded a higher PF than the MEGP collimator, due to reduction of the number of penetrated photons. PF was similar for ^{90}Y measured in the 120-250 keV window and in the 50-250 keV energy window, but the first was more contaminated by septal penetration, and the latter more by scatter. The ^{166}Ho LSF was more contaminated by septal penetration than by scatter.

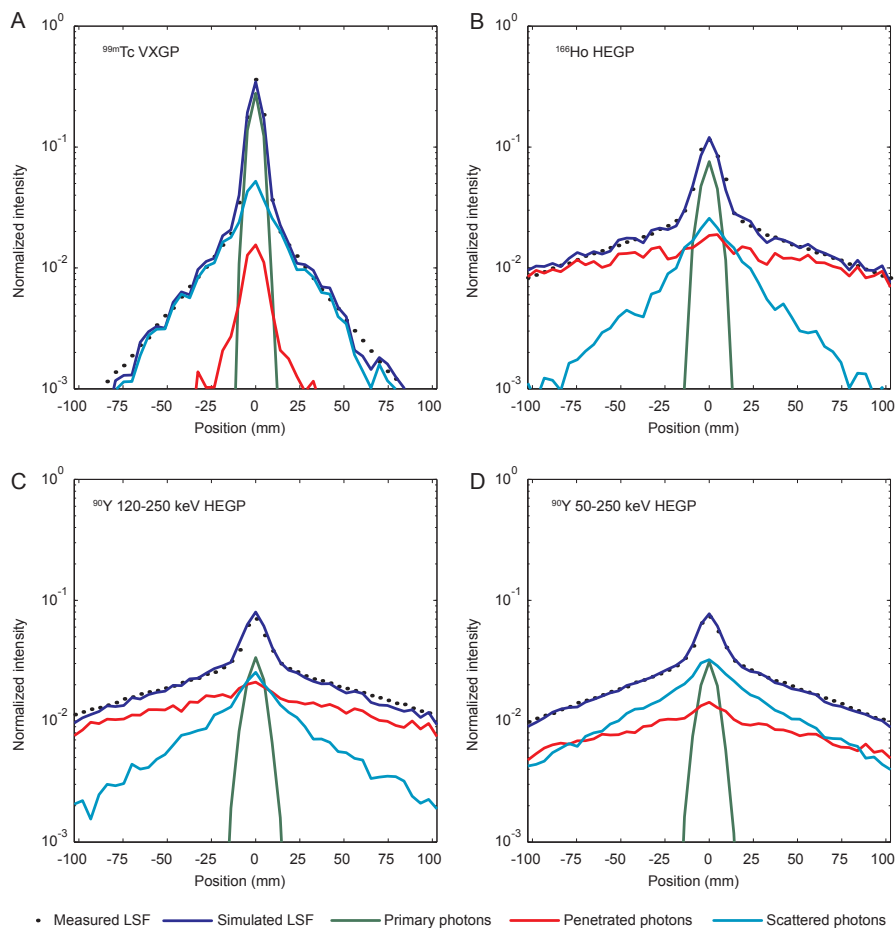


Figure 2.6. Measured and simulated LSF of the line-source centered in 20 cm PMMA. (A) LSF of the ^{99m}Tc line-source and VXGP collimator, (B) ^{166}Ho and HEGP, (C) ^{90}Y 120-250 keV and HEGP, and (D) ^{90}Y 50-250 keV and MEGP. Data is plotted on semi-logarithmic scale, showing good agreement between the measurements (data points) and simulations (blue solid line). The intensity is normalized to the total number of counts in the ROI. Contributions of primary, scattered, and penetrated photons are shown in green, light blue, and red, respectively.

Table 2.6. Monte Carlo simulated primary, scatter and collimator penetration fractions for the experimental set-up with the line source centered in 20 cm PMMA.

	^{99m}Tc	^{90}Y 120-250 keV		^{90}Y 50-250 keV		^{166}Ho	
	VXGP	MEGP	HEGP	MEGP	HEGP	MEGP	HEGP
PF (%)	56	6	10	6	9	15	20
SF (%)	37	21	33	41	54	20	27
CPF (%)	7	73	58	52	37	65	54

2.4 Discussion

The scintillation camera imaging characteristics of three radionuclides used in RE were quantitatively evaluated with phantom experiments and Monte Carlo simulations. Although the superiority of ^{99m}Tc was expected, its characteristics are valuable in evaluation of and comparison to the other two radionuclides.

NEMA prescribes assessment of spatial resolution by means of point source measurements, but the more practical approach of the line source was chosen in this work. Nonetheless, good agreement between the FWHM presented here and in the literature was found for all radionuclides. The measured FWHM of ^{99m}Tc appeared to be slightly larger than that given in the specifications of the camera manufacturer (8.2 mm and 7.8 mm, respectively). This difference might be due to the measurement set-up with the source behind 1 cm PMMA. Indeed, measurement of the ^{99m}Tc line source in air (data not shown) yielded a FWHM of 7.7 mm. The set-up was chosen, however, to be in line with ^{90}Y and ^{166}Ho measurements, which need the scatter material around the source to create all Bremsstrahlung photons. The spatial resolution of the ^{90}Y LSF was in good agreement with results of previous studies, despite small differences in measurement settings. Shen et al reported a FWHM of 12.5 mm for a point source placed behind 1.8 cm of lucite, a source to detector (HEGP collimator) distance of 6.8 cm and an energy window of 55-285 keV (6), which is in good agreement with the FWHM of 11.4 mm found in this study for the line source behind 1 cm PMMA, a source to detector distance of 6 cm, and an energy window of 50-250 keV. Interestingly, the FWHM of the 120-250 keV window was slightly smaller than the 50-250 keV window, whereas the FWTM was substantially larger. This effect can be explained by the higher (collimator) scatter fraction in the 50-250 keV window, which broadened the FWHM, and the larger amount of collimator penetration in the 120-250 keV window, which caused a large FWTM. The spatial resolution of ^{166}Ho was investigated by Bayouth and Macey, reporting a FWHM of approximately 16 mm of a line source measured behind 12 cm of scatter material (19), which is in good agreement with the FWHM of 15.6 mm of the ^{166}Ho line source behind 10 cm PMMA (HEGP, collimator distance 11 cm) found in this study.

The ^{90}Y planar system sensitivity was similar to earlier reports (6). The sensitivity found for ^{166}Ho was higher than the window-based, non-primary subtraction corrected sensitivity reported by Bayouth and Macey (19). Good agreement was found if taking into account that about half of the detected photons of this study are non-primary, as was estimated from Monte Carlo simulations. The MEGP collimator

showed a higher planar sensitivity than the HEGP collimator for both ^{90}Y and ^{166}Ho . However, Monte Carlo simulations elucidated higher primary fractions for the HEGP than for the MEGP collimator (Table 2.6). Monte Carlo simulations also revealed that ^{90}Y and ^{166}Ho non-primary photons lack spatial information, as is illustrated in Figure 2.6. Taking this into account, the useable sensitivity of the HEGP collimator, i.e. the sensitivity for primary photons, is similar to that of the MEGP collimator. With similar number of primary photons, and less background signal due to penetrated photons, the HEGP is preferred over the MEGP collimator for both ^{90}Y and ^{166}Ho .

The contrast recovery SPECT data was reconstructed using FBP, without inclusion of collimator modeling and scatter correction techniques. Compared to (model-based) iterative reconstruction algorithms, the FBP approach will result in suboptimal contrast recovery, but the first requires parameters that need to be optimized and have a large effect on image quality, such as the number of iterations. Reasonably accurate model-based quantitative image reconstruction methods have been proposed for both ^{166}Ho and ^{90}Y (5,20), but these have distinct underlying algorithms, which makes straight-forward comparison of the radionuclide performance difficult. The FBP reconstructed contrast recovery coefficients reported in this study should not be interpreted as a measure of maximum radionuclide performance, but as a measure of radionuclide performance relative to each other. Since contrast recovery depends on resolution, scatter and penetration, it can be interpreted as a quantitative measure of overall image quality. This image quality of $^{99\text{m}}\text{Tc}$ is higher than the ^{166}Ho image quality, which in turn is higher than that of ^{90}Y (Figure 2.5). No differences in ^{90}Y contrast recovery were observed between energy windows and collimators. Although the HEGP collimator demonstrated a higher spatial resolutions and higher primary photon fraction than the MEGP collimator, differences were potentially too subtle to cause a substantial gain in contrast recovery in the FBP reconstructed images. Likewise, the ^{166}Ho contrast recovery curves did not show differences between the MEGP and HEGP collimators. From Figure 2.4, however, it can be appreciated that the perceptual ^{90}Y image quality is substantially better in the 50-250 keV energy window than the 120-250 keV energy window, due to reduction of the image noise. It can therefore be postulated that the use of a broad energy window and a HEGP collimator gave the optimal combination of sensitivity, spatial resolution and primary photon fraction for ^{90}Y imaging, although differences with the MEGP collimator were small. The HEGP collimator also slightly outperformed the MEGP collimator in the ^{166}Ho experiments.

The Monte Carlo simulations provided valuable information on the contribution and spatial distribution of different classes of photons, which could not be obtained by performing measurements alone. As is illustrated in Figure 2.6, there is a fundamental difference between the penetrated photons of ^{99m}Tc and those of ^{90}Y and ^{166}Ho . Collimator penetration of ^{99m}Tc photons is dominated by photons that slightly graze the septum edge. These photons maintain their spatial information. On the contrary, collimator penetration of ^{90}Y and ^{166}Ho is dominated by high-energy photons that, after penetration, scatter in the crystal or backscatter in the camera. These photons lack spatial information and degrade the image quality. Also, from Figure 2.6 it can be appreciated that photon scatter is the main source of degradation of ^{90}Y image quality in the 50-250 keV energy window, and collimator penetration in the 120-250 keV energy window.

The results presented in this paper suggest that accurate scatter and collimator penetration correction techniques could greatly enhance the quantitative accuracy of ^{90}Y and ^{166}Ho scintillation camera imaging. Quantitative accuracies of ^{99m}Tc SPECT with optimized correction techniques are typically within 5% for phantom studies and within 10% for clinical studies (31-34). Reasonably accurate distribution estimates in phantoms have already been reported for ^{166}Ho SPECT by de Wit *et al.* (20) and for ^{90}Y by Minarik *et al.* (5). The quantitative accuracy of ^{99m}Tc SPECT might be approached if these correction schemes are further improved, which is important for accurate assessment of the distribution of the scout dose, determination of the lung-shunting fraction, and post-treatment liver dosimetry in radioembolization.

Besides scintillation camera imaging, other imaging modalities may also allow for quantitative assessment of the microsphere distribution in radioembolization. Recently, Positron Emission Tomography (PET) was proposed to image the ^{90}Y treatment dose distribution (35-38) and phantom experiments have demonstrated the feasibility of quantitative imaging of the distribution of (non-radioactive) holmium with magnetic resonance imaging (MRI) (15,39,40). Although both ^{90}Y PET and holmium MRI have intrinsically promising imaging characteristics, such as a high spatial resolution, the clinical value of these modalities in microsphere radioembolization is yet unknown and subject of ongoing research.

In this study, the scintillation camera imaging characteristics of three radionuclides used in radioembolization were quantitatively evaluated and compared. The use of a broad energy window and HEGP collimator gave optimal combination of sensitivity, spatial resolution, and primary photon fraction for ^{90}Y Bremsstrahlung imaging, although differences with the MEGP collimator were small. For ^{166}Ho imaging, the

HEGP collimator slightly outperformed the MEGP. The image quality of both ^{90}Y and ^{166}Ho was affected more by partial volume effects, scatter, and collimator penetration than that of $^{99\text{m}}\text{Tc}$. The detailed breakdown of these imaging characteristics can help to direct the optimization of acquisition protocols and quantitative reconstruction algorithms for ^{90}Y and ^{166}Ho SPECT. The characterization of the three radionuclides can guide future comparisons between or within clinical radioembolization studies with varying radionuclides and imaging protocols.

References

- 1 Kennedy AS, Salem R. Radioembolization (yttrium-90 microspheres) for primary and metastatic hepatic malignancies. *Cancer J*. 2010;16:163-175.
- 2 Vente MA, Wondergem M, van der Tweel I et al. Yttrium-90 microsphere radioembolization for the treatment of liver malignancies: a structured meta-analysis. *Eur Radiol*. 2009;19:951-959.
- 3 Gulec SA, Fong Y. Yttrium 90 microsphere selective internal radiation treatment of hepatic colorectal metastases. *Arch Surg*. 2007;142:675-682.
- 4 Fabbri C, Sarti G, Cremonesi M et al. Quantitative analysis of 90Y Bremsstrahlung SPECT-CT images for application to 3D patient-specific dosimetry. *Cancer Biother Radiopharm*. 2009;24:145-154.
- 5 Minarik D, Sjogreen GK, Ljungberg M. Evaluation of quantitative (90)Y SPECT based on experimental phantom studies. *Phys Med Biol*. 2008;53:5689-5703.
- 6 Shen S, DeNardo GL, Yuan A, DeNardo DA, DeNardo SJ. Planar gamma camera imaging and quantitation of yttrium-90 bremsstrahlung. *J Nucl Med*. 1994;35:1381-1389.
- 7 Minarik D, Ljungberg M, Segars P, Gleisner KS. Evaluation of quantitative planar 90Y bremsstrahlung whole-body imaging. *Phys Med Biol*. 2009;54:5873-5883.
- 8 Ho S, Lau WY, Leung TW et al. Tumour-to-normal uptake ratio of 90Y microspheres in hepatic cancer assessed with 99Tcm macroaggregated albumin. *Br J Radiol*. 1997;70:823-828.
- 9 Ho S, Lau WY, Leung TW, Chan M, Johnson PJ, Li AK. Clinical evaluation of the partition model for estimating radiation doses from yttrium-90 microspheres in the treatment of hepatic cancer. *Eur J Nucl Med*. 1997;24:293-298.
- 10 Bult W, Vente MAD, Zonnenberg BA, van het Schip AD, Nijsen JFW. Microsphere, radioembolization of liver malignancies: current developments. *Q J Nucl Med Mol Imaging*. 2009;53:325-335.
- 11 Koch W, Tatsch K. Nuclear medicine procedures for treatment evaluation. In: Bilbao JI, Reiser MF, editors, eds. *Liver radioembolization with 90Y microspheres*. Heidelberg: Springer; 2008:75-91.
- 12 Sabet A, Ahmadzadehfard H, Muckle M et al. Significance of Oral Administration of Sodium Perchlorate in Planning Liver-Directed Radioembolization. *J Nucl Med*. 2011;52:1063-1067.
- 13 Salem R, Parikh P, Atassi B et al. Incidence of Radiation Pneumonitis After Hepatic Intra-Arterial Radiotherapy With Yttrium-90 Microspheres Assuming Uniform Lung Distribution. *Am J Clin Oncol*. 2008;31:431-438.
- 14 Nijsen JF, Zonnenberg BA, Woittiez JR et al. Holmium-166 poly lactic acid microspheres applicable for intra-arterial radionuclide therapy of hepatic malignancies: effects of preparation and neutron activation techniques. *Eur J Nucl Med*. 1999;26:699-704.
- 15 Nijsen JF, Seppenwoolde JH, Havenith T, Bos C, Bakker CJ, van het Schip AD. Liver tumors: MR imaging of radioactive holmium microspheres--phantom and rabbit study. *Radiology*. 2004;231:491-499.
- 16 Vente MA, Nijsen JF, de Wit TC et al. Clinical effects of transcatheter hepatic arterial embolization with holmium-166 poly(L-lactic acid) microspheres in healthy pigs. *Eur J Nucl Med Mol Imaging*. 2008;35:1259-1271.
- 17 Smits MLJ, Nijsen JFW, van den Bosch MAAJ et al. Holmium-166 radioembolization for the treatment of patients with liver metastases: design of the phase I HEPAR trial. *J Exp Clin Onc Res*. 2010;29.

- 18 Vente MA, de Wit TC, van den Bosch MA et al. Holmium-166 poly(L-lactic acid) microsphere radioembolisation of the liver: technical aspects studied in a large animal model. *Eur Radiol.* 2010;20:862-869.
- 19 Bayouth JE, Macey DJ. Quantitative imaging of holmium-166 with an Anger camera. *Phys Med Biol.* 1994;39:265-279.
- 20 de Wit TC, Xiao J, Nijssen JF et al. Hybrid scatter correction applied to quantitative holmium-166 SPECT. *Phys Med Biol.* 2006;51:4773-4787.
- 21 National Electrical Manufacturers Association. NEMA Standards Publication NU 1-2007: Performance Measurements of Gamma Cameras. 2007. Rosslyn, VA, National Electrical Manufacturers Association.
- 22 National Electrical Manufacturers Association. NEMA Standards Publication NU 2-2007: Performance Measurements of Positron Emission Tomographs. 2007. Rosslyn, VA, National Electrical Manufacturers Association.
- 23 Knesaurek K, Machac J, Muzinic M, DaCosta M, Zhang Z, Heiba S. Quantitative comparison of yttrium-90 (90Y)-microspheres and technetium-99m (99mTc)-macroaggregated albumin SPECT images for planning 90Y therapy of liver cancer. *Technol Cancer Res Treat.* 2010;9:253-262.
- 24 Mansberg R, Sorensen N, Mansberg V, Van der Wall H. Yttrium 90 Bremsstrahlung SPECT/CT scan demonstrating areas of tracer/tumour uptake. *Eur J Nucl Med Mol Imaging.* 2007;34:1887.
- 25 Clarke LP, Cullom SJ, Shaw R et al. Bremsstrahlung Imaging Using the Gamma-Camera - Factors Affecting Attenuation. *J Nucl Med.* 1992;33:161-166.
- 26 Flamen P, Vanderlinden B, Delatte P et al. Multimodality imaging can predict the metabolic response of unresectable colorectal liver metastases to radioembolization therapy with Yttrium-90 labeled resin microspheres. *Phys Med Biol.* 2008;53:6591-6603.
- 27 Ito S, Kurosawa H, Kasahara H et al. (90)Y bremsstrahlung emission computed tomography using gamma cameras. *Ann Nucl Med.* 2009;23:257-267.
- 28 Sorensen JA. Deadtime characteristics of anger cameras. *J Nucl Med.* 1975;16:284-288.
- 29 Hendricks JS, McKinney GW, Waters LS et al. MCNPX Extensions, Version 2.5.0. 2005. Los Alamos, CA, Los Alamos National Laboratory Report LA-UR-05-2675.
- 30 Rault E, Staelens S, Van HR, De BJ, Vandenberghe S. Fast simulation of yttrium-90 bremsstrahlung photons with GATE. *Med Phys.* 2010;37:2943-2950.
- 31 Da Silva AJ, Tang HR, Wong KH, Wu MC, Dae MW, Hasegawa BH. Absolute Quantification of Regional Myocardial Uptake of 99mTc-Sestamibi with SPECT: Experimental Validation in a Porcine Model. *J Nucl Med.* 2001;42:772-779.
- 32 Shcherbinin S, Celler A, Belhocine T, Vanderwerf R, Driedger A. Accuracy of quantitative reconstructions in SPECT/CT imaging. *Phys Med Biol.* 2008;53:4595-4604.
- 33 Vandervoort E, Celler A, Harrop R. Implementation of an iterative scatter correction, the influence of attenuation map quality and their effect on absolute quantitation in SPECT. *Phys Med Biol.* 2007;52:1527-1545.
- 34 Zeintl J, Vija AH, Yahil A, Hornegger J, Kuwert T. Quantitative Accuracy of Clinical 99mTc SPECT/CT Using Ordered-Subset Expectation Maximization with 3-Dimensional Resolution Recovery, Attenuation, and Scatter Correction. *J Nucl Med.* 2010;51:921-928.
- 35 Gates VL, Esmail AAH, Marshall K, Spies S, Salem R. Internal Pair Production of (90)Y Permits Hepatic Localization of Microspheres Using Routine PET: Proof of Concept. *J Nucl Med.* 2011;52:72-76.

- 36 Walrand S, Jamar F, van Elmbt L, Lhommel R, Bekonde EB, Pauwels S. 4-Step Renal Dosimetry Dependent on Cortex Geometry Applied to (90)Y Peptide Receptor Radiotherapy: Evaluation Using a Fillable Kidney Phantom Imaged by (90)Y PET. *J Nucl Med*. 2010;51:1969-1973.
- 37 Lhommel R, Goffette P, Van den Eynde M et al. Yttrium-90 TOF PET scan demonstrates high-resolution biodistribution after liver SIRT. *Eur J Nucl Med Mol Imaging*. 2009;36:1696.
- 38 Lhommel R, van Elmbt L, Goffette P et al. Feasibility of Y-90 TOF PET-based dosimetry in liver metastasis therapy using SIR-Spheres. *Eur J Nucl Med Mol Imaging*. 2010;37:1654-1662.
- 39 Seevinck PR, Seppenwoolde JH, Zwanenburg JJ, Nijsen JF, Bakker CJ. FID sampling superior to spin-echo sampling for T2*-based quantification of holmium-loaded microspheres: theory and experiment. *Magn Reson Med*. 2008;60:1466-1476.
- 40 Seppenwoolde JH, Nijsen JF, Bartels LW, Zielhuis SW, van het Schip AD, Bakker CJ. Internal radiation therapy of liver tumors: qualitative and quantitative magnetic resonance imaging of the biodistribution of holmium-loaded microspheres in animal models. *Magn Reson Med*. 2005;53:76-84.

Chapter 3

**Quantitative comparison of PET and Bremsstrahlung SPECT
for imaging the *in vivo* yttrium-90 microsphere distribution
after liver radioembolization**



Published as:

M. Elschot, B.J. Vermolen, M.G.E.H. Lam, B. de Keizer, M.A.A.J. van den Bosch, H.W.A.M. de Jong. Quantitative comparison of PET and Bremsstrahlung SPECT for imaging the *in vivo* yttrium-90 microsphere distribution after liver radioembolization. *PLoS ONE*. 2013;8:e55742

Abstract

Objectives

After yttrium-90 (^{90}Y) microsphere radioembolization (RE), evaluation of extrahepatic activity and liver dosimetry is typically performed on ^{90}Y Bremsstrahlung SPECT images. Since these images demonstrate a low quantitative accuracy, ^{90}Y PET has been suggested as an alternative. The aim of this study is to quantitatively compare SPECT and state-of-the-art PET on the ability to detect small accumulations of ^{90}Y and on the accuracy of liver dosimetry.

Methods

SPECT/CT and PET/CT phantom data were acquired using several acquisition and reconstruction protocols, including resolution recovery and Time-Of-Flight (TOF) PET. Image contrast and noise were compared using a torso-shaped phantom containing six hot spheres of various sizes. The ability to detect extra- and intrahepatic accumulations of activity was tested by quantitative evaluation of the visibility and unique detectability of the phantom hot spheres. Image-based dose estimates of the phantom were compared to the true dose. For clinical illustration, the SPECT and PET-based estimated liver dose distributions of five RE patients were compared.

Results

At equal noise level, PET showed higher contrast recovery coefficients than SPECT. The highest contrast recovery coefficients were obtained with TOF PET reconstruction including resolution recovery. All six spheres were consistently visible on SPECT and PET images, but PET was able to uniquely detect smaller spheres than SPECT. TOF PET-based estimates of the dose in the phantom spheres were more accurate than SPECT-based dose estimates, with underestimations ranging from 45% (10-mm sphere) to 11% (37-mm sphere) for PET, and 75% to 58% for SPECT, respectively. The differences between TOF PET and SPECT dose-estimates were supported by the patient data.

Conclusions

In this study we quantitatively demonstrated that the image quality of state-of-the-art PET is superior over Bremsstrahlung SPECT for the assessment of the ^{90}Y microsphere distribution after radioembolization.

3.1 Introduction

Intra-arterial radioembolization (RE) using microspheres labeled with the high-energy beta-emitter yttrium-90 (^{90}Y), is used in clinical practice for treatment of unresectable liver tumors (1,2). Prior to RE, prophylactic coil-embolization of arteries communicating with the gastrointestinal (GI) tract is performed, followed by administration of technetium-99m macroaggregated-albumin ($^{99\text{m}}\text{Tc-MAA}$) particles. Subsequent gamma camera imaging is used to assess any extrahepatic particle deposition, which is a contra-indication for RE. Also, the percentage of particles that shunts to the lungs is measured, which may lead to adjustment of the ^{90}Y dose (3). After administration of the ^{90}Y microspheres, a post-treatment ^{90}Y Bremsstrahlung SPECT scan is performed for two reasons. First, ^{90}Y may unexpectedly be present outside the liver, despite a favorable distribution on the $^{99\text{m}}\text{Tc-MAA}$ scan. Accumulation of ^{90}Y microspheres in organs other than the liver will likely cause serious complications, like ulceration and bleedings in the GI tract (4,5). Therefore, severe pain after treatment should be aggressively managed to prevent development of more serious complications (4), which may be facilitated by early detection of possible extrahepatic activity (6). Second, the intrahepatic microsphere distribution over tumorous and non-tumorous liver tissue is expected to be an important predictor of treatment efficacy (7). Post-treatment imaging facilitates estimation of the tumor and non-tumor absorbed radiation dose on the image-based microsphere distribution.

Unfortunately, the low photon yield and continuous nature of the Bremsstrahlung X-ray spectrum limit the quantitative accuracy of ^{90}Y Bremsstrahlung SPECT. Per MBq, approximately 23000 Bremsstrahlung photons with energy higher than 50 keV are produced by interaction of the beta particle with tissue (8), therefore acquisition in a wide energy window is required to maximize sensitivity. The absence of a photopeak prohibits the use of simple window-based scatter rejection, scatter correction, and attenuation correction techniques, and penetration of high-energy photons through the collimator septa leads to further loss of image contrast (9). Recent efforts to optimize reconstruction algorithms, e.g. by compensation for scatter and collimator blurring with pre-calculated ^{90}Y point-spread functions (PSF) (8,10), have improved the quantitative accuracy of ^{90}Y Bremsstrahlung SPECT, but are not widely available in the clinic to date.

Yttrium-90 PET was recently shown to be feasible in phantoms and patients and may be an interesting alternative to Bremsstrahlung SPECT (11). Per MBq, ^{90}Y emits

32 positrons per second with a maximum energy of 758 keV (12,13). Consequently, annihilation photon pairs are produced approximately 700 times less often than Bremsstrahlung photons ($E > 50$ keV). Nevertheless, ^{90}Y PET may allow for the detection of extrahepatic activity and accurate tumor and liver dose estimation, since the spatial resolution is expected to be comparable to that of ^{18}F PET, which has a maximum positron energy of 633 keV (14). Additionally, advanced correction techniques for scatter, random, and attenuation effects that are clinically available for ^{18}F PET, can be directly applied to ^{90}Y PET (15). Several groups have successfully assessed the post-treatment ^{90}Y microsphere distribution in RE patients (11,16-19).

To date, no systematic studies have quantitatively compared clinically available ^{90}Y PET with Bremsstrahlung SPECT. The potential for accurately assessing the intra- and extrahepatic microsphere distribution is determined by fundamental limitations of the imaging modality. The first objective of this study was to quantitatively evaluate and compare the contrast and noise characteristics of ^{90}Y PET and SPECT images, which are relevant parameters for activity detection and liver dosimetry in clinical practice. Image contrast depends on spatial resolution and on other effects that distort quantification of local ^{90}Y content, like photon attenuation, photon scatter, collimator penetration and random coincidences. Image noise is dependent on sensitivity and on the stochastic nature of attenuation, scatter and collimation. The second objective was to quantitatively compare ^{90}Y PET and SPECT on the ability to detect small accumulations of ^{90}Y inside and outside the liver, and on the accuracy of liver dose estimates, based on the recorded ^{90}Y distribution. All quantitative results were obtained in phantom experiments. Additionally, Bremsstrahlung SPECT and PET scans of five ^{90}Y RE patients were evaluated to support the results of the phantom study.

3.2 Materials and Methods

3.2.1 Ethics statement

Dual post-treatment imaging using both SPECT/CT and PET/CT techniques was part of the quality control protocol for implementation of ^{90}Y -PET imaging as the standard post-radioembolization procedure. All data were retrospectively analyzed, written patient informed consent was therefore not sought nor documented. The institutional review board (IRB) of the University Medical Center Utrecht approves this type of retrospective study and waives the requirements for patient informed consent. The image data were handled anonymously, in accordance with the Declaration of Helsinki and the regulations of the IRB.

3.2.2 Scanners, acquisition and reconstruction

PET/CT data were acquired on a state-of-the-art Siemens mCT Time-Of-Flight (TOF) PET/CT scanner (Siemens Medical Solutions USA, Inc.). The mCT combines a whole body LSO PET scanner with a 40-slice CT scanner. The PET component is equipped with a large axial field-of-view (FOV) of 21.8 cm and wide acceptance angle of 13.2° to maximize sensitivity. In whole body mode, consecutive bed positions overlap approximately 43%. A detailed characterization of the physical and clinical performance of the mCT was performed by Jakoby *et al* (20). PET data were acquired with a lower- and upper-level discriminator of 435 keV and 650 keV, respectively. Three reconstruction algorithms were compared, all including correction for random coincidences, scatter and attenuation (20). The first algorithm was fully 3D iterative attenuation weighted ordinary Poisson ordered subset expectation maximization (OP-OSEM) reconstruction (21) ('iterative'), the second algorithm was iterative reconstruction extended with a PSF model of the detector response (22) ('iterative+PSF'), and the third was iterative reconstruction including PSF and TOF information ('iterative+PSF+TOF'). Images were reconstructed using 3 iterations with 24 or 21 (iterative+PSF+TOF) subsets and a 5 mm full-width at half-maximum (FWHM) Gaussian post-reconstruction filter. The reconstructed voxel size was $2 \times 2 \times 2 \text{ mm}^3$.

SPECT/CT data were acquired on a Siemens Symbia T16 system (Siemens Medical Solutions USA, Inc.). The Symbia T16 combines a dual detector SPECT scanner with a 16-slice CT scanner. The SPECT detectors are equipped with 3/8 inch thick crystals. All our experiments were performed with the high-energy collimators mounted, which proved to be the best option for ^{90}Y imaging with maximum resolution and contrast (9,23). SPECT data were acquired in a 105-195 keV energy window (8,24), using 120 projections over 360° and a 256×256 matrix with a pixel size of $2.4 \times 2.4 \text{ mm}^2$. Images were reconstructed with two different reconstruction algorithms. The first algorithm was 2D OSEM reconstruction including correction for attenuation with an effective broad beam linear attenuation coefficient ('iterative'), and the second algorithm was iterative reconstruction including a Gaussian PSF model of the geometric collimator-detector response of the camera (25) ('iterative+PSF'). In both cases 8 iterations with 8 subsets were used without post-reconstruction filtering. The reconstructed voxel size was $2.4 \times 2.4 \times 2.4 \text{ mm}^3$.

3.2.3 Phantom set up

The NEMA 2007/IEC 2008 PET Image Quality (IQ) Phantom, which is designed for evaluation of reconstructed image quality and activity recovery, was used for all phantom experiments to allow for direct comparison between the two modalities (26). The phantom consists of a fillable torso-shaped compartment (volume = 9700 ml) containing six fillable coplanar spheres (inner diameter = 10, 13, 17, 22, 28, and 37 mm) and a cylindrical lung insert.

Table 3.1 lists the separately performed phantom experiments. PET data were acquired in one bed position centered on the spheres. Since the PET FOV covering a whole liver requires two bed positions (30 cm in axial direction) and for SPECT one FOV (40 cm) is sufficient, all PET scan times were set to half the SPECT scan times. The initial ^{90}Y activity concentration in the spheres ($[A]_{\text{sph}}$) and background compartment ($[A]_{\text{bkg}}$) was 2.40 and 0 MBq ml $^{-1}$, respectively. All six spheres were filled with activity, which slightly deviates from the NEMA recommendations. After performing experiments 1, ^{90}Y was added to the background for experiments 2-4, resulting in $[A]_{\text{bkg}} = 0.27$ MBq ml $^{-1}$. The total activity in the phantom was 119 and 2600 MBq, for experiments 1, and 2-4, respectively. Instead of adjusting the activity in the phantom, the scan times were prolonged x 2 and x 4 times in experiments 2-4 to obtain the simulated activity concentrations given in Table 3.1. This approach was deemed valid, because both the measured total activity and the maximum simulated total activity, which corresponded to approximately 2600 MBq for a 2000 ml liver, were within the linear range (i.e. no dead time effects) of ^{90}Y PET and Bremsstrahlung SPECT (9,11).

Table 3.1. Phantom experiments.

Exp.	Ratio	Modality	Real scan time (min.)	$[A]_{\text{sph}}$ (MBq ml $^{-1}$)	$[A]_{\text{bkg}}$ (MBq ml $^{-1}$)
1P	1:0	PET	15	2.4 (real)	0 (real)
1S	1:0	SPECT	30	2.4 (real)	0 (real)
2P	9:1	PET	15	2.4 (real)	0.27 (real)
2S	9:1	SPECT	30	2.4 (real)	0.27 (real)
3P	9:1	PET	30	4.8 (simulated)	0.54 (simulated)
3S	9:1	SPECT	60	4.8 (simulated)	0.54 (simulated)
4P	9:1	PET	60	9.6 (simulated)	1.09 (simulated)
4S	9:1	SPECT	120	9.6 (simulated)	1.09 (simulated)

3.2.4 Image contrast and noise

Image contrast and noise measurements were obtained from phantom experiments 4 (Table 3.1), representing a clinically realistic liver background activity concentration of 1.09 MBq ml⁻¹. For comparison: using the body surface area (BSA) method (see 'Patients' section), the mean activity concentration in a 1.5 kg liver with 10% tumor involvement of an 'average' patient (1.70 m, 70 kg) would be 1.14 MBq ml⁻¹. Six circular hot sphere regions of interest (ROIs) were automatically delineated on the CT slice through the center of the spheres, covering the inner compartment voxels of each of the six phantom spheres. A background ROI was delineated on the same slice consisting of all voxels that fell within the physical phantom boundaries, excluding the voxels belonging to the hot sphere ROIs and the lung insert. For each reconstructed SPECT and PET volume, contrast recovery coefficients (Q_H) were calculated with equation 3.1.

$$Q_H = \frac{C_H/C_B - 1}{R - 1} \times 100\% \quad (3.1)$$

Here, C_H is the mean intensity in the hot sphere ROIs, C_B is the mean intensity in the background ROI and R is the true sphere-to-background activity concentration ratio. As a measure of image noise, the coefficient of variation (CV) was calculated with equation 3.2.

$$CV = \frac{STDV_B}{C_B} \times 100\% \quad (3.2)$$

Here, $STDV_B$ is the standard deviation in the background ROI.

3.2.5 Detectability

The ability to detect small accumulations of activity (detectability) in a region without background activity is important for evaluation of extrahepatic microsphere deposition. Additionally, the detectability of activity in a region with background activity is important when intrahepatic tumor identification is based on the contrast in the SPECT and PET scans, e.g. using isocontours when the target volume cannot be derived from a CT or MRI scan.

A hot spot of activity can only be accurately identified, if it can be reliably distinguished from the background, i.e. if it is visible. The visibility (v_H) of the six hot spheres was tested by quantitative evaluation of the hot sphere and background signal; for each hot sphere the effective contrast-to-noise ratio (CNR) was calculated according to equation 3.3.

$$v_H = \frac{C_H - C_B}{STDV_B} \times \sqrt{N_{\text{voxels}}} \quad (3.3)$$

with C_H , C_B , and $STDV_B$ as defined in the previous section and N_{voxels} the number of voxels in the hot sphere ROI. Subsequently, a hot sphere was scored 'visible' when u_H was larger than 4, in accordance with the Rose criterion (27,28).

In addition to the visibility criterion, which is an established method for detection of false negatives, a new method is presented to evaluate the presence of false positive hot spots. Since accumulations of activity are not 'uniquely detectable' if false positives are present, we will refer to this criterion as 'unique detectability' in the remainder of this work. The unique detectability of the six hot spheres was evaluated in five consecutive background slices, placed five cm away from the slice through the center of the spheres. Circular ROIs to test for false positives ($ROI_{\text{TEST-FP}}$) with the same diameter as the hot sphere ROIs were centered on all phantom voxels in the five slices. The visibility ($u_{\text{TEST-FP}}$) of each $ROI_{\text{TEST-FP}}$ was calculated with equation 3.4.

$$v_{\text{TEST-FP}} = \frac{C_{\text{TEST-FP}} - C_B}{STDV_B} \times \sqrt{N_{\text{voxels}}} \quad (3.4)$$

Here, $C_{\text{TEST-FP}}$ is the mean intensity in $ROI_{\text{TEST-FP}}$, C_B the mean intensity in the background ROI of the same slice (consisting of all voxels falling within the phantom boundaries, excluding the lung insert), $STDV_B$ the standard deviation in the background ROI and N_{voxels} the number of voxels in $ROI_{\text{TEST-FP}}$. We investigated two different criteria to score a sphere 'uniquely detectable'. According to the first criterion, a visible hot sphere was scored 'uniquely detectable', if $u_{\text{TEST-FP}}$ was smaller than 4 for all $ROI_{\text{TEST-FP}}$ of the same size, i.e. if none of the corresponding $ROI_{\text{TEST-FP}}$ were visible according to the Rose criterion. Translated to clinical practice, this criterion measures whether any visible hot spot of a certain diameter can be reliably characterized as 'true positive'. According to the second criterion, a visible hot sphere was scored 'uniquely detectable' if $u_{\text{TEST-FP}}$ was smaller than u_H for all $ROI_{\text{TEST-FP}}$ of the same size, i.e. if the hot sphere was better visible than all corresponding $ROI_{\text{TEST-FP}}$. This criterion is less strict and measures whether the visible hot spot with the highest CNR can be reliably characterized as 'true positive'.

When using CNR with the relaxation term $\sqrt{N_{\text{voxels}}}$ for evaluation of the visibility of hot spots, a uniform count density in the hot spot ROI is assumed. However, the mean intensities of the relatively small hot sphere and false positive ROIs are

susceptible to outliers and may therefore not accurately represent human perception. Median values, on the other hand, are less sensitive to outliers and may be a better measure for this purpose. Consequently, equations 3 and 4 were also evaluated using median intensities for C_H and $C_{TEST-FP}$, respectively. The 'median-based' hot sphere visibility and unique detectability results were presented next to their 'mean-based' equivalents. Data from experiments 1 (Table 3.1) were used to analyze the extrahepatic detectability and experiments 2-4 were used to mimic the intrahepatic situation, for three different activity concentrations.

3.2.6 Patients

Radioembolization with ^{90}Y -labeled resin microspheres (SIR-Spheres, Sirtex Medical, Sydney, Australia) was performed in 5 consecutive patients (2 women, 3 men; mean age \pm SD, 56.8 \pm 13.0 y; age range 43-76 y) according to the international consensus report from the Radioembolization Brachytherapy Oncology Consortium (3). The BSA method was used to calculate the activities (A) administered to the patients, according to the equation $A \text{ (GBq)} = \text{BSA} - 0.2 + V_T/V_L$, with $\text{BSA} \text{ (m}^2\text{)} = 0.20247 * \text{height}^{0.725} * \text{weight}^{0.425}$, and V_T and V_L the tumor and whole liver volume derived from CT or MRI, respectively. Dose adjustments were not required, since the percentage $^{99\text{m}}\text{Tc-MAA}$ lung shunting was below 10% for all patients. Four patients were diagnosed with liver metastases (2 colorectal carcinomas, 1 nasopharyngeal carcinoma, and 1 mammary carcinoma) and one patient was diagnosed with hepatocellular carcinoma. Four patients received whole liver treatment and one patient received left lobar treatment. PET data were acquired in two bed positions (total scan length 30 cm) centered on the liver, whereas the SPECT axial FOV was 40 cm. SPECT and PET data were both acquired in 30 minutes, which was considered the maximum desirable scan time for a RE patient. All patient and treatment characteristics are summarized in Table 3.2.

3.2.7 Absorbed dose estimation

Phantom

The iterative+PSF+TOF PET and iterative+PSF SPECT images of experiments 4 (Table 3.1) were used to evaluate the accuracy of dosimetry. Calibration factors to convert the PET and SPECT images into units of activity were determined by dividing the total reconstructed counts in the phantom by the known activity in the phantom. A digital phantom representing the 'true activity distribution' (TRUE) was constructed from a segmented high-resolution CT dataset (voxel size 0.6x0.6x0.6 mm³). Activity

concentrations of 1.09 MBq ml^{-1} and 9.6 MBq ml^{-1} were applied to the segmented 3D background ROI and 3D hot sphere ROIs, respectively. Dose maps were calculated from the PET, SPECT, and TRUE activity images by convolution with the appropriate ^{90}Y 3D dose-point kernel (DPK), in accordance with MIRD Pamphlet No. 17 (29). For this purpose, DPKs with the same voxel sizes as the high-resolution CT, SPECT and PET images were calculated using the Monte Carlo engine MCNPX 2.5.0 (30).

Three-dimensional ROIs of the fillable spheres and a 2000 ml background region were delineated on the CT scans, altogether representing a liver with tumors. Cumulative dose-volume histograms (CDVH) and mean absorbed doses were calculated for all ROIs. Additionally, the mean absorbed doses in the hot sphere ROIs were corrected for incomplete activity recovery due to partial volume effects (PVE), by multiplication with the corresponding correction factors calculated as $R * C_B / C_H$. Errors in the uncorrected and corrected SPECT and PET-based dose estimates were calculated in comparison to the TRUE dose.

Patients

Patient data were reconstructed with the same settings as the phantom data. Three-dimensional liver ROIs were manually delineated on the CT scans. To be able to mutually compare the SPECT and PET-based dose distributions, the liver ROI of each patient was segmented into a low-dose ROI and a high-dose ROI. The high-dose ROI included all voxels that had on one or both modalities an activity concentration of at least two times the mean liver concentration. The low-dose ROI consisted of the other liver voxels, i.e. the liver ROI excluding the high-dose ROI. The resulting 'integrated' SPECT/PET ROIs allowed for an unbiased, direct comparison of the dose distribution between the modalities. Following conversion of PET and SPECT activity images into dose maps, CDVH and mean absorbed doses were calculated for all ROIs.

3.3 Results

3.3.1 Image contrast and noise

Figure 3.1 shows that iterative+PSF+TOF reconstruction resulted in PET images with the highest contrast recovery. Iterative+PSF reconstruction resulted in the highest contrast recovery for SPECT. PET contrast recovery coefficients were substantially higher than those of SPECT in all spheres. In comparison, both image contrast and image noise were higher in PET than in SPECT (Figure 3.2 A), which is also evident from the transversal slices through the phantom in Figure 3.2 B and 3.2 C. The

noise level in the PET images was substantially reduced when reconstructed with 1 iteration and a 15 mm FWHM post-reconstruction filter (equal noise (EQN) PET), approximately to the noise level of the SPECT images (approximately 18% CV, Figure 3.2 A and 3.2 D). This set-up allows for a fair comparison of image contrast. At equal noise level, all PET images still showed higher contrast than SPECT, although contrast was lost in comparison with PET images reconstructed with optimal settings.

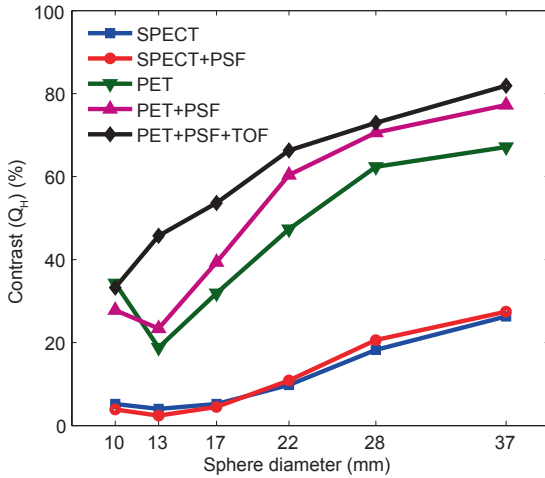


Figure 3.1. Contrast recovery as a function of sphere diameter for all reconstruction methods.

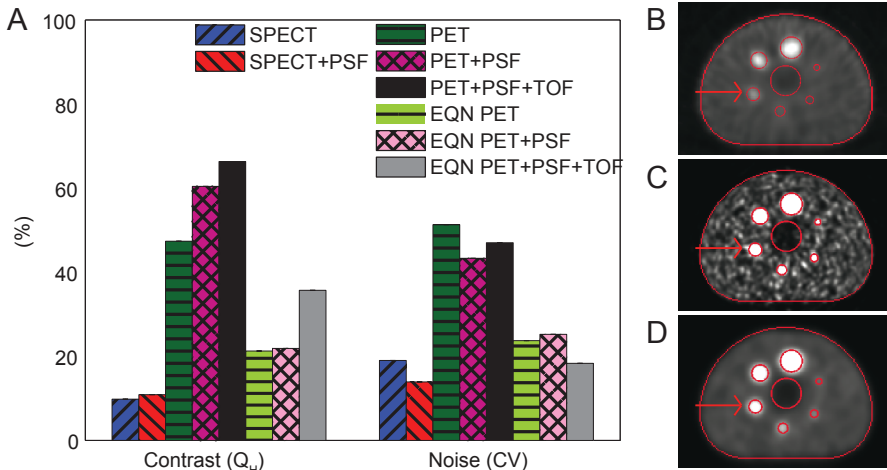


Figure 3.2. PET and SPECT contrast recovery and image noise. Contrast recovery and image noise in the 22-mm sphere for all reconstruction methods (A), the slice through the center of the SPECT volume (iterative+PSF) (B), the slice through the center of the PET volume (iterative+PSF+TOF) (C), and the slice through the center of the PET volume (iterative+PSF+TOF) reconstructed with SPECT-like noise level (D). All images were linearly window-leveled from 0 to 4 times the mean intensity in the background ROI. The boundaries of the central lung insert, the six hot sphere ROIs, and the background ROI are illustrated by the red lines and the 22-mm sphere is indicated by the arrow.

Table 3.2. Patient and treatment characteristics.

Patient	Primary ^a	Lobes ^b	V _L ^c	V _T ^d	A _A ^e	A _S ^f	A _P ^g
1	CRC	W	2481	153	1714	1303	1602
2	CRC	W	1835	50	1852	1483	1499
3	NPC	W	1230	72	1199	922	1109
4	MC	L	383	20	281	216	270
5	HCC	W	3050	178	1177	916	927

^a Primary disease: CRC = colorectal carcinoma; NPC = nasopharyngeal carcinoma; MC = mammary carcinoma; HCC = hepatocellular carcinoma

^b Lobes treated: W = whole liver treatment; L = left lobar treatment

^c V_L = treated liver volume (ml)

^d V_T = volume of tumors in treated liver volume (ml)

^e A_A = Activity administered to the patient, at time of administration (MBq)

^f A_S = Activity at time of SPECT acquisition (MBq)

^g A_P = Activity at time of PET acquisition (MBq)

3.3.2 Detectability

From Table 3.3 it can be appreciated that the ‘mean-based’ and ‘median-based’ visibility results were equal for all images but one. The unique detectability results differed between the ‘mean-based’ and ‘median-based’ approach, for both detectability criteria. From Figure 3.3 it is apparent the ‘mean-based’ approach detected more false positives than the ‘median-based’ approach. Being less affected by outliers, the ‘median-based’ approach only detected the more or less uniform false positives regions and was therefore considered the best approach for false positive detection. Consequently, in the remainder of this section the ‘median-based’ results are reported for hot sphere visibility and unique detectability. Table 3.3 and Figure 3.3 show that in the extrahepatic situation, all six spheres were visible on SPECT and PET images according to the Rose criterion. According to the criterion $u_{\text{TEST-FP}} < 4$, none of the spheres were uniquely detectable with SPECT, whereas the smallest sphere uniquely detectable with PET was 28 mm in diameter. According to the criterion $u_{\text{TEST-FP}} < u_{\text{H}}$, all hot spheres in the cold background were uniquely detectable with PET, whereas the smallest sphere uniquely detectable with SPECT was 13 mm in diameter. For all three activity concentrations of the intrahepatic situation, all six spheres were visible with both SPECT and PET, but none of them was uniquely detectable according to the criterion $u_{\text{TEST-FP}} < 4$. According to the criterion $u_{\text{TEST-FP}} < u_{\text{H}}$, the smallest sphere uniquely detectable with PET was 13 mm in diameter, whereas this was 22 mm for SPECT, for all activity concentrations.

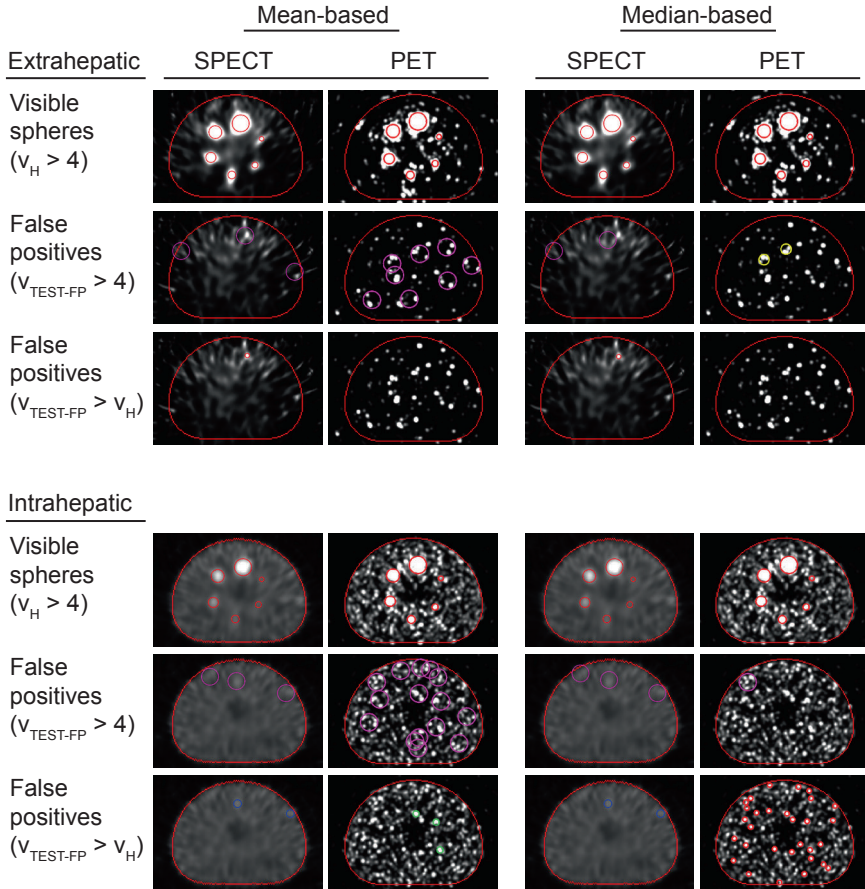


Figure 3.3. Visualization of the visibility and unique detectability results. The activity concentration in the hot spheres was 2.4 MBq ml^{-1} for both the images without (rows 1-3) and with background activity (rows 4-6). In the 1st and 4th row, the SPECT+PSF (1st and 3rd column) and PET+PSF+TOF (2nd and 4th column) slices are overlaid with the location of the visible phantom spheres (red). In rows 2, 3, 5 and 6 a background slice is overlaid with the location of false positive regions. For illustrative reasons, only the largest false positive ROIs are shown (red: 10 mm; green: 13 mm; blue: 17 mm; yellow: 22 mm; purple: 37 mm). Clustered ROIs with connecting center voxels are represented by the ROI with the highest $u_{TEST-FP}$ value.

Table 3.3. Extra- and intrahepatic visibility and unique detectability. The extra- and intrahepatic activity distribution is represented by hot spheres in a cold and warm background, respectively. For each image, the diameters (mm) of the first ‘mean-based’ visible and uniquely detectable spheres are given, followed by the diameters of the ‘median-based’ results in brackets. ‘X’ means that none of the spheres were uniquely detectable.

Visible: $u_H > 4$	Extrahepatic	Intrahepatic		
	$[A]_{\text{sph}}$ (MBq ml ⁻¹)	$[A]_{\text{sph}}$ (MBq ml ⁻¹)		
	2.4	9.6	4.8	2.4
SPECT	10 (10)	10 (10)	13 (13)	10 (10)
SPECT+PSF	10 (10)	10 (10)	10 (10)	10 (10)
PET	10 (10)	10 (10)	10 (10)	10 (13)
PET+PSF	10 (10)	10 (10)	10 (10)	10 (10)
PET+PSF+TOF	10 (10)	10 (10)	10 (10)	10 (10)
Uniquely detectable: $u_{\text{TEST-FP}} < 4$				
SPECT	X (X)	X (X)	X (X)	X (X)
SPECT+PSF	X (X)	X (X)	X (X)	X (X)
PET	X (37)	X (X)	X (X)	X (X)
PET+PSF	X (X)	X (X)	X (X)	X (X)
PET+PSF+TOF	X (28)	X (X)	X (X)	X (X)
Uniquely detectable: $u_{\text{TEST-FP}} < u_H$				
SPECT	17 (17)	22 (22)	22 (22)	22 (28)
SPECT+PSF	13 (13)	22 (22)	22 (22)	22 (22)
PET	13 (13)	17 (17)	17 (17)	13 (22)
PET+PSF	13 (13)	17 (17)	13 (17)	13 (22)
PET+PSF+TOF	10 (10)	10 (13)	13 (13)	17 (13)

3.3.3 Absorbed dose estimation

Phantom

The error of the uncorrected (in brackets: corrected for PVE) PET dose estimates ranged from -11% (+6%) for the largest sphere to -45% (+40%) for the smallest sphere (Table 3.4). For SPECT the errors were larger, ranging from -58% (+18%) to -75% (+69%). Figure 3.4 shows that the PET-based CDVH of the hot sphere ROI followed the true CDVH more closely than the SPECT-based CDVH. The higher image noise in TOF PET was reflected by the flattened slope of the CDVH curve.

Table 3.4. Phantom dosimetry. The uncorrected mean dose (Gy) in the 6 hot sphere ROIs and the background ROI (BKG), followed by the mean dose corrected for PVE in brackets (spheres only). The TRUE dose represents the actual dose in the phantom.

	Phantom ROI						
	10 mm	13 mm	17 mm	22 mm	28 mm	37 mm	BKG
SPECT	76 (516)	69 (514)	78 (511)	102 (487)	143 (484)	181 (508)	61
PET	167 (431)	224 (432)	255 (433)	333 (475)	324 (426)	384 (457)	60
TRUE	306	341	372	395	412	432	52

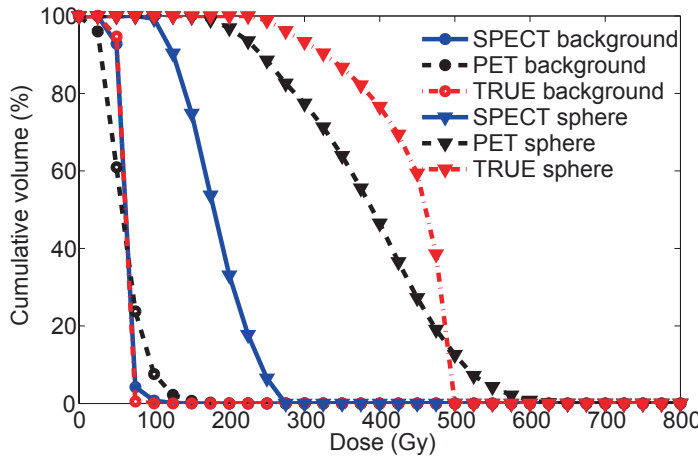


Figure 3.4. Phantom dosimetry. CDVH of the phantom background ROI and the ROI of the 37-mm diameter sphere. The presented doses were not corrected for PVE.

Patients

For all patients, the difference between the estimated dose in the high-dose ROI and the low-dose ROI was larger for PET than for SPECT (Table 3.5). This effect is also illustrated by the CDVH and fused images of patient 2 in Figure 3.5.

Table 3.5. Patient dosimetry. The mean dose (Gy) in the low-dose ROI (LD) and the high-dose ROI (HD) are given for all patients.

	Patient ROI									
	1		2		3		4		5	
	LD	HD	LD	HD	LD	HD	LD	HD	LD	HD
SPECT	26	37	34	73	30	53	22	36	12	31
PET	29	85	38	111	33	80	26	58	11	47



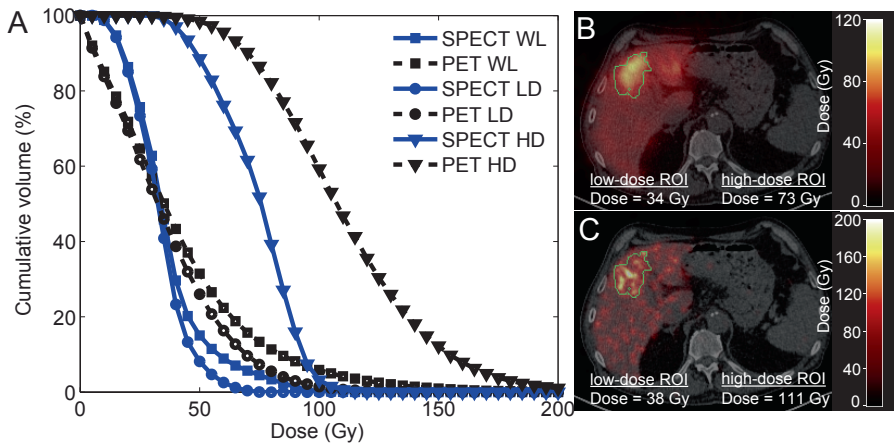


Figure 3.5. Patient 2 dosimetry. The CDVH of the whole liver (WL), low-dose (LD) and high-dose (HD) ROIs of patient 2 (A), a transversal slice through the SPECT-based dose map, fused with CT (B), and the same transversal slice through the PET-based dose map (C). The boundary of the high-dose ROI is depicted by the green line.

3.4 Discussion

In this study, we quantitatively compared the accuracy of ^{90}Y Bremsstrahlung SPECT and state-of-the-art PET for the assessment of the intra- and extrahepatic microsphere distribution after radioembolization, using the physical parameters image contrast and image noise, and the clinically relevant parameters detectability and dosimetry. We realize that image contrast and noise not only depend on the fundamental limitations of the imaging modalities, but also on acquisition and reconstruction settings; e.g., a well-known property of iterative reconstruction algorithms is that contrast can be maximized at the cost of noise amplification by varying the number of iterations (31). Before defining the study setup as published, we evaluated image contrast and noise for various energy windows (wide: 50 – 250 keV (6,9,23,32-35); medium-wide: 105 – 195 keV (8,24); small: 76 – 105 keV (36,37), SPECT only), various numbers of iterations (1, 3, 5, and 8), and various post-reconstruction filters (0, 5, and 10 mm FWHM). The settings resulting in the highest image contrast were the starting point for this study. The results imply that ^{90}Y Bremsstrahlung SPECT and PET image contrast is improved by inclusion of a PSF model in the reconstruction process. The PET image contrast is further improved by inclusion of TOF information, which also resulted in slightly higher image noise. The latter can be attributed to faster convergence of TOF reconstruction (20). At similar noise level, all PET algorithms demonstrated higher contrast recovery coefficients than optimal SPECT. Therefore, we conclude that the image quality of ^{90}Y state-of-the-art PET outperforms Bremsstrahlung SPECT.

In comparison with ^{18}F PET and $^{99\text{m}}\text{Tc}$ SPECT, the Q_{H} of ^{90}Y were consistently lower (e.g. 66% (^{90}Y) vs 71% (^{18}F) and 11% (^{90}Y) vs 57% ($^{99\text{m}}\text{Tc}$) for the 22-mm sphere, data not shown). The large difference in SPECT Q_{H} can probably be attributed to the low spatial resolution and the large amount of photon scatter and septal penetration with ^{90}Y (9), all of which increase the PVE. Recent work on ^{90}Y SPECT reconstruction demonstrated that image contrast may be substantially improved by including accurate models of the scattered and penetrated photons, but these algorithms are not available in the clinic to date (8,10). To the contrary, PET reconstruction algorithms include advanced techniques to correct for random coincidences, photon scatter, and attenuation effects. Nevertheless, a slight difference in Q_{H} between ^{90}Y and ^{18}F was observed, which was probably not caused by resolution effects; the difference in spatial resolution was estimated to be within 1%, using the analytical resolution model of Lubberink and Herzog (38). Instead, the intensity in the low-count background region may have been overestimated, possibly due to sparsity of the (smoothed) delayed coincidences sinogram that is used for random correction in the OP-OSEM algorithm (39). This effect has also been observed in dynamic studies with short frame rates (40). Further research is required to fully understand the clinical impact of these effects.

Inadvertent extrahepatic deposition of activity may be detected directly post-treatment on ^{90}Y SPECT or PET images. Ahmadzadehfar *et al* showed that detection of extrahepatic activity on Bremsstrahlung SPECT/CT scans predicted GI ulcers with a sensitivity of 87% and a specificity of 100%, despite low image quality (6). In this study, we investigated the detectability of accumulations of activity of different sizes with the well-known Rose criterion for detection of false negatives and with a new method for detection of false positives. The ‘median-based’ unique detectability approach was deemed better than its ‘mean-based’ equivalent, since the latter tended to erroneously classify non-uniform regions as ‘false positive’. We demonstrated that the visibility of intra- and extrahepatic accumulations of activity was equal between SPECT and PET, for the investigated sphere sizes and activity concentration ratios. Unique detectability with the $u_{\text{TEST-FP}} < u_{\text{H}}$ criterion demonstrated larger differences between PET and SPECT than the $u_{\text{TEST-FP}} < 4$ criterion, but will depend on the activity concentration in the hot spheres. Nevertheless, according to both criteria, PET was able to uniquely detect smaller accumulations of activity than SPECT, endorsing the use of (TOF) PET/CT instead of SPECT/CT. Given the relative simplicity of the detectability models used, we should emphasize that the results of our phantom study should not be interpreted as the lower limits of (lesion) detection

performance by a human observer, but merely as a comparison between ^{90}Y SPECT and PET. The results are likely to be dependent on acquisition and reconstruction settings, which were optimized for image contrast in this study. Optimization of the imaging protocols for noise, e.g. by increasing the FWHM of the post-reconstruction filter, may improve the unique detectability of hot spots.

Accurate tumor and liver dosimetry can improve RE patient care, e.g. by facilitating (selective) re-treatment of tumorous tissue that did not receive a sufficient dose during the first treatment. The relationship between the $^{99\text{m}}\text{Tc}$ -MAA SPECT-based tumor absorbed dose and tumor response is reported in numerous publications investigating the possibilities of treatment optimization by individualized $^{99\text{m}}\text{Tc}$ -MAA SPECT-based dose planning (e.g. (7,33,41)). To the contrary, publications on the ^{90}Y SPECT or PET-based dose-response relation are relatively sparse (42,43). The latter approach has the advantage of imaging the real ^{90}Y microsphere distribution, which avoids the question of accurate prediction of the microsphere distribution with $^{99\text{m}}\text{Tc}$ -MAA, but it is not used for individualized treatment planning. Using phantom experiments, we demonstrated that ^{90}Y TOF PET-based dose estimates were more accurate than Bremsstrahlung SPECT-based dose estimates. Based on the incomplete contrast recovery observed in the image quality phantom, dose underestimations with both PET and SPECT were to be expected. SPECT-based absorbed dose estimates in the high-dose regions of the phantom were lower than those of PET, which was supported by the results of our patient study. When correcting the hot sphere mean dose estimates for PVE, the absolute dose errors were reduced, but dose overestimations up to 69% were still observed. The use of PVE correction factors is restricted to correction of mean ROI values, and PVE correction was therefore applied to the mean absorbed dose values of the hot sphere ROIs. Due to the range of the beta-particles, however, the mean absorbed dose in the hot sphere ROIs not only depends on the locally absorbed energy as a result of activity in the ROIs itself, but also on the energy absorbed as a result of activity in adjacent background voxels. With hot spheres in a warm background, PVE result in an underestimation of the first contribution to the mean absorbed dose, whereas the latter contribution is overestimated. Consequently, application of the activity-based PVE correction factors leads to erroneous up-scaling of the adjacent background voxels' contribution to the mean absorbed dose in the hot sphere ROIs. This effect is stronger for smaller spheres, due to the relatively large amount of adjacent background voxels, and stronger for SPECT than for PET, due to the higher correction factors of the first. For dosimetry purposes, a better approach may be to determine correction factors on

dose images, which not only include PVE but also DPK effects. However, these dose correction factors will strongly depend on the activity concentration ratio between ROIs and adjacent background voxels, which undesirably complicates PVE correction in clinical practice. For this reason, we chose not to correct the mean dose estimates in the patient study for PVE effects. The results of the patient study indicate that the use of high-resolution PET can potentially improve dose-response relationships on the level of the tumor for ^{90}Y RE. The evaluation of the estimated absorbed liver dose in low-dose and high-dose regions, which did not necessarily coincide with healthy liver and tumor regions, did not harm the conclusions presented in this study, since the primary aim was a quantitative comparison of the ^{90}Y SPECT and PET-based dose distribution, and not clinical liver dosimetry. Evaluation of the absorbed dose to tumorous and healthy liver tissue should be performed in a larger (prospective) patient study and is beyond the scope of this study.

3.5 Conclusion

This study demonstrates that the ^{90}Y image quality of state-of-the-art PET is superior over Bremsstrahlung SPECT for the assessment of the microsphere distribution after radioembolization. Intra- and extrahepatic hot spots of 10 mm in diameter or larger are visible on SPECT and PET images, but PET is able to uniquely detect smaller accumulations of activity than SPECT. Additionally, TOF PET-based dose estimates are more accurate than SPECT-based dose estimates, which give large underestimations in high-dose regions.

References

- 1 Kennedy AS, Salem R. Radioembolization (yttrium-90 microspheres) for primary and metastatic hepatic malignancies. *Cancer J*. 2010;16:163-175.
- 2 Vente MA, Wondergem M, van der Tweel I et al. Yttrium-90 microsphere radioembolization for the treatment of liver malignancies: a structured meta-analysis. *Eur Radiol*. 2009;19:951-959.
- 3 Kennedy AS, Nag S, Salem R et al. Recommendations for radioembolization of hepatic malignancies using yttrium-90 microsphere brachytherapy: A consensus panel report from the Radioembolization Brachytherapy Oncology Consortium. *Int J Radiat Oncol Biol Phys*. 2007;68:13-23.
- 4 Riaz A, Lewandowski RJ, Kulik LM et al. Complications Following Radioembolization with Yttrium-90 Microspheres: A Comprehensive Literature Review. *J Vasc Intervent Radiol*. 2009;20:1121-1130.
- 5 Murthy R, Brown DB, Salem R et al. Gastrointestinal complications associated with hepatic arterial yttrium-90 microsphere therapy. *J Vasc Intervent Radiol*. 2007;18:553-562.
- 6 Ahmadzadehfard H, Muckle M, Sabet A et al. The significance of Bremsstrahlung SPECT-CT of the Abdomen after Yttrium 90 microsphere selective internal radiation treatment (SIRT) in the early Diagnosis of SIRT-Induced Extrahepatic Side Effects. *Eur J Nucl Med Mol Imaging*. 2010;37:S264.
- 7 Chiesa C, Maccauro M, Romito R et al. Need, feasibility and convenience of dosimetric treatment planning in liver selective internal radiation therapy with Y-90 microspheres: the experience of the National Cancer Institute of Milan. *Q J Nucl Med Mol Imaging*. 2011;55:168-197.
- 8 Minarik D, Sjogreen GK, Ljungberg M. Evaluation of quantitative (90)Y SPECT based on experimental phantom studies. *Phys Med Biol*. 2008;53:5689-5703.
- 9 Elschot M, Nijssen JFW, Dam AJ, de Jong HWAM. Quantitative Evaluation of Scintillation Camera Imaging Characteristics of Isotopes Used in Liver Radioembolization. *PLoS ONE*. 2011;6:e26174.
- 10 Rong X, Du Y, Ljungberg M, Rault E, Vandenberghe S, Frey EC. Development and evaluation of an improved quantitative Y-90 bremsstrahlung SPECT method. *Med Phys*. 2012;39:2346-2358.
- 11 Lhommel R, van Elmbt L, Goffette P et al. Feasibility of Y-90 TOF PET-based dosimetry in liver metastasis therapy using SIR-Spheres. *Eur J Nucl Med Mol Imaging*. 2010;37:1654-1662.
- 12 Langhoff H, Hennies HH. Zum Experimentellen Nachweis Von Zweiquantenzerfall Beim $0^+ \rightarrow 0^+$ -Übergang des Zr90. *Z Phys*. 1961;164:166-173.
- 13 Nickles RJ, Roberts AD, Nye JA et al. Assaying and PET imaging of yttrium-90: $1 > 34 \text{ ppm} > 0$. *Conf Record of IEEE Nuclear Science Symp and Medical Imaging Conf*. 2004;6:3412-3414.
- 14 Bailey DL, Karp JS, Surti S. Physics and instrumentation in PET. In: Valk PE, Bailey DL, Townsend DW, Maisey MN, eds. *Positron Emission Tomography: Basic Science and Clinical Practice*. London: Springer-Verlag; 2003:41-67.
- 15 van Elmbt L, Walrand S, Lhommel R, Jamar F, Pauwels S. Quantitative comparison between LYSO and BGO PET-tomographs in 90Y imaging. *Eur J Nucl Med Mol Imaging*. 2010;37:S293.
- 16 Lhommel R, Goffette P, Van den Eynde M et al. Yttrium-90 TOF PET scan demonstrates high-resolution biodistribution after liver SIRT. *Eur J Nucl Med Mol Imaging*. 2009;36:1696.

- 17 Werner MK, Brechtel K, Beyer T, Dittmann H, Pfannenbergs C, Kupferschlag J. PET/CT for the assessment and quantification of Y-90 biodistribution after selective internal radiotherapy (SIRT) of liver metastases. *Eur J Nucl Med Mol Imaging*. 2010;37:407-408.
- 18 Gates VL, Esmail AAH, Marshall K, Spies S, Salem R. Internal Pair Production of (90)Y Permits Hepatic Localization of Microspheres Using Routine PET: Proof of Concept. *J Nucl Med*. 2011;52:72-76.
- 19 D'Arienzo M, Chiamarida P, Chiacchiararelli L et al. Y-90 PET-based dosimetry after selective internal radiotherapy treatments. *Nucl Med Commun*. 2012;33:633-640.
- 20 Jakoby BW, Bercier Y, Conti M, Casey ME, Bendriem B, Townsend DW. Physical and clinical performance of the mCT time-of-flight PET/CT scanner. *Phys Med Biol*. 2011;56:2375-2389.
- 21 Comtat C, Kinahan PE, Defrise M, Michel C, Townsend DW. Fast reconstruction of 3D PET data with accurate statistical modeling. *IEEE Trans Nucl Sci*. 1998;45:1083-1089.
- 22 Panin VY, Kehren F, Michel C, Casey M. Fully 3-D PET reconstruction with system matrix derived from point source measurements. *IEEE Trans Med Imaging*. 2006;25:907-921.
- 23 Shen S, DeNardo GL, Yuan A, DeNardo DA, DeNardo SJ. Planar gamma camera imaging and quantitation of yttrium-90 bremsstrahlung. *J Nucl Med*. 1994;35:1381-1389.
- 24 Minarik D, Ljungberg M, Segars P, Gleisner KS. Evaluation of quantitative planar 90Y bremsstrahlung whole-body imaging. *Phys Med Biol*. 2009;54:5873-5883.
- 25 Tsui BMW, Hu HB, Gilland DR, Gullberg GT. Implementation of Simultaneous Attenuation and Detector Response Correction in Spect. *IEEE Trans Nucl Sci*. 1988;35:778-783.
- 26 National Electrical Manufacturers Association. NEMA Standards Publication NU 2-2007: Performance Measurements of Positron Emission Tomographs. 2007. Rosslyn, VA, National Electrical Manufacturers Association.
- 27 Cherry SR, Sorenson JA, Phelps ME. *Physics in Nuclear Medicine*. Philadelphia: Saunders; 2003:290.
- 28 Rose A. The Sensitivity Performance of the Human Eye on An Absolute Scale. *J Opt Soc Am*. 1948;38:196-208.
- 29 Bolch WE, Bouchet LG, Robertson JS et al. MIRD pamphlet No. 17: the dosimetry of nonuniform activity distributions--radionuclide S values at the voxel level. Medical Internal Radiation Dose Committee. *J Nucl Med*. 1999;40:11S-36S.
- 30 Hendricks JS, McKinney GW, Waters LS et al. MCNPX Extensions, Version 2.5.0. 2005. Los Alamos, CA, Los Alamos National Laboratory Report LA-UR-05-2675.
- 31 Hutton BF, Hudson HM, Beekman FJ. A clinical perspective of accelerated statistical reconstruction. *Eur J Nucl Med Mol Imaging*. 1997;24:797-808.
- 32 Clarke LP, Cullom SJ, Shaw R et al. Bremsstrahlung Imaging Using the Gamma-Camera - Factors Affecting Attenuation. *J Nucl Med*. 1992;33:161-166.
- 33 Flamen P, Vanderlinden B, Delatte P et al. Multimodality imaging can predict the metabolic response of unresectable colorectal liver metastases to radioembolization therapy with Yttrium-90 labeled resin microspheres. *Phys Med Biol*. 2008;53:6591-6603.
- 34 Fabbri C, Sarti G, Cremonesi M et al. Quantitative analysis of 90Y Bremsstrahlung SPECT-CT images for application to 3D patient-specific dosimetry. *Cancer Biother Radiopharm*. 2009;24:145-154.
- 35 Ito S, Kurosawa H, Kasahara H et al. (90)Y bremsstrahlung emission computed tomography using gamma cameras. *Ann Nucl Med*. 2009;23:257-267.
- 36 Mansberg R, Sorensen N, Mansberg V, Van der Wall H. Yttrium 90 Bremsstrahlung SPECT/CT scan demonstrating areas of tracer/tumour uptake. *Eur J Nucl Med Mol Imaging*. 2007;34:1887.

- 37 Knesaurek K, Machac J, Muzinic M, DaCosta M, Zhang Z, Heiba S. Quantitative comparison of yttrium-90 (90Y)-microspheres and technetium-99m (99mTc)-macroaggregated albumin SPECT images for planning 90Y therapy of liver cancer. *Technol Cancer Res Treat*. 2010;9:253-262.
- 38 Lubberink M, Herzog H. Quantitative imaging of (124)I and (86)Y with PET. *Eur J Nucl Med Mol Imaging*. 2011;38:10-18.
- 39 Comtat C, Bataille F, Michel C et al. OSEM-3D reconstruction strategies for the ECAT HRRT. *Conf Record of IEEE Nuclear Science Symp and Medical Imaging Conf*. 2004;6:3492-3496.
- 40 van Velden FHP, Kloet RW, van Berckel BNM, Wolfensberger SPA, Lammertsma AA, Boellaard R. Comparison of 3D-OP-OSEM and 3D-FBP reconstruction algorithms for High-Resolution Research Tomograph studies: effects of randoms estimation methods. *Phys Med Biol*. 2008;53:3217-3230.
- 41 Garin E, Lenoir L, Rolland Y et al. Dosimetry Based on Tc-99m-Macroaggregated Albumin SPECT/CT Accurately Predicts Tumor Response and Survival in Hepatocellular Carcinoma Patients Treated with Y-90-Loaded Glass Microspheres: Preliminary Results. *J Nucl Med*. 2012;53:255-263.
- 42 Strigari L, Sciuto R, Rea S et al. Efficacy and Toxicity Related to Treatment of Hepatocellular Carcinoma with Y-90-SIR Spheres: Radiobiologic Considerations. *J Nucl Med*. 2010;51:1377-1385.
- 43 Walrand S, Lhommel R, Goffette P, Van den Eynde M, Pauwels S, Jamar F. Hemoglobin level significantly impacts the tumor cell survival fraction in humans after internal radiotherapy. *EJNMMI Res*. 2012;2:20.

Chapter 4

Quantitative Monte Carlo-based yttrium-90 SPECT reconstruction



Accepted for publication as:

M. Elschot, M.G.E.H. Lam, M.A.A.J. van den Bosch, M.A. Viergever, H.W.A.M. de Jong. Quantitative Monte Carlo-based yttrium-90 SPECT reconstruction. *J Nucl Med*.

Abstract

Objectives

Evaluation of the radiation absorbed dose on tumorous and healthy tissue is of increasing interest for yttrium-90 (^{90}Y) microsphere radioembolization of liver malignancies. The objective of this work is to introduce and validate a new reconstruction method for quantitative ^{90}Y Bremsstrahlung SPECT to improve post-treatment dosimetry.

Methods

A fast Monte Carlo simulator was adapted for ^{90}Y and incorporated in a statistical reconstruction algorithm (SPECT-MC). Photon scatter and attenuation for all photons sampled from the full ^{90}Y energy spectrum were modeled during reconstruction by Monte Carlo simulations. The energy- and distance-dependent collimator-detector response was modeled using pre-calculated convolution kernels. The NEMA2007/IEC2008 image quality phantom was used to quantitatively evaluate the performance of SPECT-MC in comparison with state-of-the-art clinical SPECT reconstruction and PET. The SPECT, PET and SPECT-MC estimated liver radiation absorbed doses were evaluated in five patients consecutively treated with radioembolization.

Results

In comparison with state-of-the-art clinical ^{90}Y SPECT reconstruction, SPECT-MC substantially improved image contrast (e.g. from 25% to 88% for the 37 mm sphere) and decreased the mean residual count error in the lung insert (from 73% to 15%) at the cost of higher image noise. Image noise and the mean count error were lower for SPECT-MC than for PET. Image contrast was higher in the larger spheres (diameter ≥ 28 mm) for SPECT-MC than for PET, but lower in the smaller spheres (≤ 22 mm). In the clinical study, mean absorbed dose estimates in high-absorbed-dose liver regions were consistently higher for SPECT-MC than for SPECT ($p = 0.0625$) and consistently higher for SPECT-MC than for PET ($p = 0.0625$).

Conclusions

The quantitative accuracy of ^{90}Y Bremsstrahlung SPECT is substantially improved by Monte Carlo-based modeling of the image degrading factors. Consequently, ^{90}Y Bremsstrahlung SPECT may be used as an alternative to ^{90}Y PET.

4.1 Introduction

The high-energy beta-emitter yttrium-90 (^{90}Y) is used in clinical practice for several radiotherapeutical applications, including intra-arterial microsphere radioembolization for treatment of unresectable liver tumors (1,2). To enable evaluation of the radiation absorbed dose to the tumorous and the healthy liver tissue, post-treatment imaging of the ^{90}Y microsphere distribution has recently gained interest (3-5).

Assessment of the ^{90}Y microsphere distribution can be performed by imaging Bremsstrahlung photons with a SPECT camera, or by imaging annihilation photons with a PET camera. Post-treatment dosimetry with ^{90}Y PET has advantages over SPECT, mainly due to the higher resolution and image contrast (6,7). However, the very low positron branch (32×10^{-6}) in ^{90}Y decay ideally requires a state-of-the-art L(Y)SO Time-Of-Flight (TOF) PET/CT scanner to obtain images with sufficiently high quantitative accuracy for dosimetry purposes (8,9). Post-treatment imaging with a standard SPECT/CT system may be a more widely available and cost-effective option for most centers, but the image quality of state-of-the-art clinical ^{90}Y Bremsstrahlung SPECT is still limited (7). The wide range (0–2.3 MeV) and continuous nature of the ^{90}Y Bremsstrahlung photon energy spectrum prohibit the use of simple energy window-based scatter rejection and correction techniques, hinder attenuation correction based on a single photon energy, and require compensation for collimator-detector related image degrading effects like collimator scatter, lead X-rays, septal penetration, camera (back)scatter, and partial energy deposition in the crystal (10). The shape and magnitude of these effects depend on photon energy, tissue composition, collimator and detector characteristics, the distance between the source and the collimator, and the energy window settings.

To date, clinically available reconstruction algorithms cannot adequately compensate for the image degrading effects that limit quantitative ^{90}Y Bremsstrahlung SPECT. However, it was recently shown by Rong et al. that extensive modeling of scatter and attenuation effects and the collimator-detector response (CDR) improves activity quantification for ^{90}Y SPECT (11). In their approach, Monte Carlo simulations were used to pre-calculate energy-dependent scatter kernels and energy- and distance-dependent CDR tables, which were subsequently applied during reconstruction. In the present study, we propose a new model-based ^{90}Y SPECT reconstruction algorithm, which makes use of a fast Monte Carlo simulator for ‘on-the-fly’ calculation of the scatter and attenuation effects in the patient, rather than using pre-calculated scatter

kernels. These Monte Carlo simulations are performed anew for every patient, during every update of the reconstruction process. The hypothetical advantage of this approach is that all photon transport physics can be included in a detailed and accurate way, irrespective of source distribution, photon energy, scatter order, non-uniform tissue density, and other complicating factors (12,13). Only the photon interactions in the collimator and detector are modeled with pre-calculated kernels. The quantitative accuracy of the proposed reconstruction method is evaluated and compared to state-of-the-art clinically available ^{90}Y Bremsstrahlung SPECT and ^{90}Y PET in phantom experiments. Additionally, intrahepatic dosimetry is performed and evaluated in five patients treated with ^{90}Y radioembolization in clinical practice.

4.2 Materials and Methods

The Utrecht Monte Carlo System (UMCS) is a validated, fully 3D Monte Carlo-based approach for simulation of gamma camera projection images of a radionuclide distribution. UMCS is fast enough for on-the-fly photon transport calculation in a statistical image reconstruction algorithm. An extensive description of standard UMCS has been given elsewhere (13,14). The approach has been validated for simulation of technetium-99m ($^{99\text{m}}\text{Tc}$) (15) and thallium-201 (^{201}Tl) projections (16). In contrast to ^{90}Y , however, these radionuclides do not require simulation of high-energy photon contributions to a lower-energy detection window. For the purpose of this work, UMCS was adapted to simulate ^{90}Y projection images, including photon contributions from the full ^{90}Y energy spectrum.

4.2.1 UMCS physics

Two major adaptations to standard UMCS as published in (14) were made to make the approach suitable for simulation of ^{90}Y projection images: the source photon energies were sampled from a continuous energy spectrum, and the energy-dependency of the CDR was modeled including all collimator-detector related image degrading effects. Schematic overviews of UMCS physics are given in Figure 4.1.

Source photon energy sampling

We implemented the ^{90}Y photon energy spectrum as a combination of the ^{90}Y Bremsstrahlung spectrum, generated with MCNPX 2.5.0 (17), the 511 keV annihilation photon peak (3.2×10^{-5} cps Bq^{-1}), and the 1760 keV prompt gamma peak (7.8×10^{-5} cps Bq^{-1}), similar to (18,19). Beta-particle physics were not implemented in UMCS. Photon

emission energies were sampled directly from the ^{90}Y photon energy distribution and photons were emitted from the point of decay. In reality, Bremsstrahlung photons are created along the tract of the beta-particle, which introduces an additional blurring. This effect was included in the CDR (see section 'Pre-calculation of CDR kernels'). After photon emission, the standard UMCS scatter and attenuation models were used for calculation of photon transport in the patient.

Simulation of scatter maps

Photons were first traced from their emission position to their final scatter position, in our case via maximally 10 scatter events. For each scatter event, the photon intensity (i.e. probability of existence), position, direction, and energy were recorded. Subsequently, for every camera angle photons were forced to Compton scatter (coherent scatter was not included) from each recorded scatter position towards the detector and the photon intensities were updated accordingly (Figure 4.1 A). For the purpose of computationally efficient modeling of the distance- and energy-dependent CDR, the updated photon intensities were voxelwise binned in eight energy-dependent, voxelized 3D scatter maps, according to their energy after the last scatter event (i.e. towards the detector). The energy limits of the scatter maps are given in Figure 4.1 B.

Photon detection

Photons of all energies may potentially contribute to the detection window (in our case 50 – 250 keV), e.g. via collimator scatter, lead X-rays, or partial energy deposition in the crystal (10). These effects are modeled by the CDR in the photon detection model. To simulate energy-dependent photon detection, we made use of techniques that have been developed for fast simulation of down-scatter projections for dual-isotope SPECT (20). The detection process was performed separately for each of the eight scatter maps, in two steps. First, for each voxel of the scatter map the photon attenuation in the patient on the path towards the detector was approximated by using a scatter map-specific attenuation coefficient (μ_{central} , Figure 4.1 B), being the central μ -value of the scatter map's energy range (bin). Second, the attenuation corrected scatter maps were blurred layer-by-layer by convolution with the pre-calculated distance-dependent CDR, which represents the spatially varying detection probability of the corresponding photon energy ($E_{\mu\text{-central}}$, Figure 4.1 B) if measured in air (see next section). Subsequently, the blurred, attenuation corrected scatter maps were summed over the direction perpendicular to the camera face to form 2D

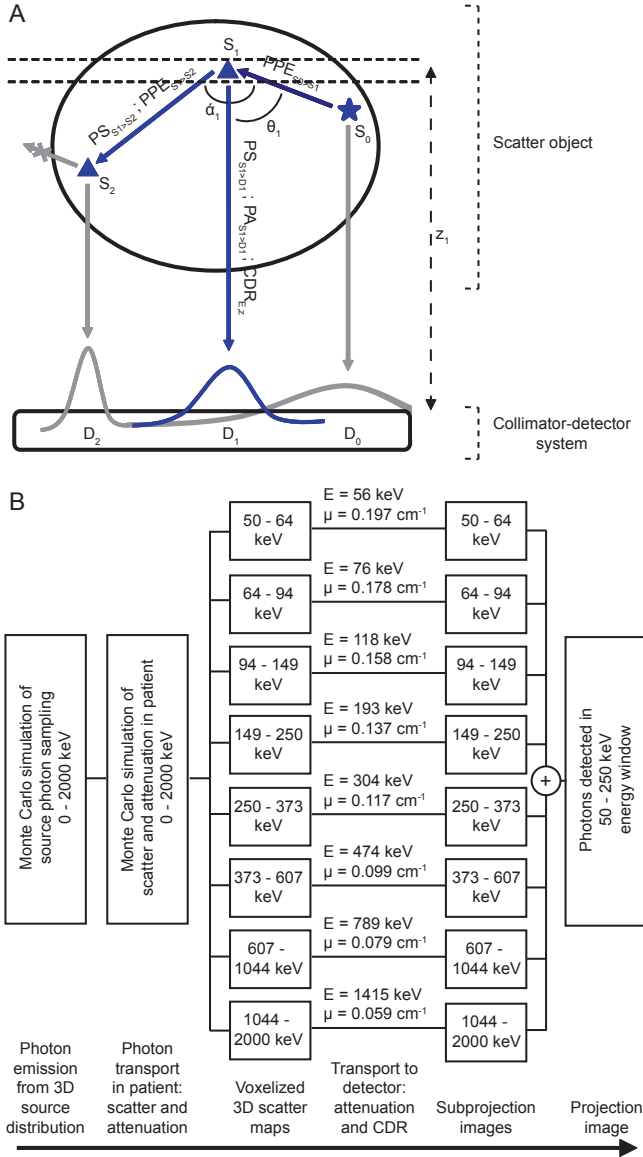


Figure 4.1. A schematic overview of the UMCS physics models in the scatter object and collimator-detector system (A) and of the subsequent steps involved in simulation of 2D projection images from a 3D source distribution (B). After photon emission (S_0), the probability of existence of a photon at scatter position S_n ($1 \leq n \leq 10$) is dependent on the probability of not having been absorbed photo-electrically (PPE) and on the probability of scattering over the angle α_n ($PS(\alpha_n)$). From each position S_n ($0 \leq n \leq 10$), a copy of the photon is forced to scatter over the angle θ_n towards the detector. The photon detection probability at position D_n depends on $PS(\theta_n)$, on the probability of not having been attenuated by the scatter object (PA_n), and on the shape and magnitude of the distance- (z_n) and energy-dependent CDR. In the last two steps (i.e. PA , CDR), which are performed after voxelwise binning of the photon intensities in energy-dependent 3D scatter maps, the attenuation coefficient is approximated by μ_{central} (μ in (B)) and the CDR is approximated by the CDR of $E_{\mu\text{-central}}$ (E in (B)).

subprojection images. The sum of all energy-dependent subprojection images formed the final simulated projection image for the given camera angle.

Pre-calculation of CDR kernels

An MCNPX model of the camera head of the Siemens Symbia T16 SPECT/CT system with a high-energy (HE) collimator mounted was developed to pre-calculate distance-dependent CDRs. For each of the eight scatter maps, photons with $E_{\mu\text{-central}}$ were emitted in air and detected in a 50 – 250 keV energy window. To take into account the effect that Bremsstrahlung photons are created along the tract of the beta-particle, photon emission positions were uniformly sampled from a sphere (containing air) with a radius of 3.15 mm. This approach results in a mean radial photon emission position of 2.5 mm, which corresponds to the mean range of the beta-particles in tissue. The CDRs were radially averaged after detection to reduce the required calculation time.

Validation of UMCS

Before application in SPECT reconstruction, the accuracy of the UMCS-simulated projection images was evaluated in two gamma camera experiments. The number of simulated photons was 10^6 . Measurements were performed with a dual-headed Siemens Symbia T16 SPECT/CT system with HE collimators mounted. Photons were detected in a 50 – 250 keV energy window on a 128 x 128 matrix with a pixel size of $4.8 \times 4.8 \text{ mm}^2$. In the first experiment, a 1 mm diameter line source was centered in a $40 \times 40 \times 20 \text{ cm}^3$ PMMA scatter object. Line-spread functions (LSFs), summed over 10-cm-wide profiles and normalized to their maximum value, were compared visually and by means of the area under the curve (AUC) between the measurement and the UMCS simulation. The measured LSF was also compared to a MCNPX simulation (10^9 photons), to validate the camera geometry for calculation of the CDRs. In the second experiment, the NEMA 2007/IEC 2008 PET Image Quality (IQ) phantom was filled with an ^{90}Y activity concentration of 0.27 MBq mL^{-1} in the torso-shaped compartment, 2.40 MBq mL^{-1} in the six fillable coplanar spheres (inner diameter = 10, 13, 17, 22, 28, and 37 mm), and no activity in the cylindrical lung insert (outer diameter = 51 mm). Ten-cm-wide profiles through the measured and UMCS-simulated projection images were compared.

4.2.2 Yttrium-90 Bremsstrahlung SPECT reconstruction

UMCS was incorporated in a dual matrix ordered subsets expectation maximization (OSEM) reconstruction framework (21) for Monte Carlo-based ^{90}Y SPECT reconstruction. In dual matrix OSEM the forward projector is not identical to the back projector, i.e. more approximate photon transport models are used in the back projection step. This approach accelerates reconstruction, while having minimal impact on image quality (13,21,22). In the forward projector, non-uniform photon attenuation, photon scatter, and the distance- and energy-dependent CDR were modeled, as explained above. The number of simulated photons per projection was 10^6 . In the back projection step, photon attenuation was approximated with a single (instead of eight) μ -value corresponding to the central energy of the acquisition window, photon scatter was not modeled, and the CDR was modeled with a distance-dependent Gaussian function. We will refer to the proposed SPECT reconstruction method as 'SPECT-MC' in the remainder of this work.

Image quality phantom experiment

The accuracy of SPECT-MC in comparison with state-of-the-art clinical SPECT and PET was quantitatively evaluated using the IQ phantom, with the activity distribution as described in the section 'Validation of UMCS'.

SPECT data were acquired with the Siemens Symbia T16 SPECT/CT system, using 120 angles over a 360° orbit and a 50 – 250 keV energy window. The acquisition time was 120 seconds per projection (120 minutes in total), resulting in a count density similar to that of a 30 minutes-long acquisition of a clinically realistic liver activity concentration of approximately 1 MBq mL^{-1} . SPECT-MC data were reconstructed to a voxel size of $4.8 \times 4.8 \times 4.8 \text{ mm}^3$ using 60 iterations with 8 subsets. No post-reconstruction filter was applied. State-of-the-art clinical SPECT reconstruction was performed with Siemens FLASH3D (8 iterations, 8 subsets, no post-reconstruction filter). Attenuation correction was performed with an effective broad beam linear attenuation coefficient of 0.034 cm^{-1} . Scatter correction was not included. PET data were acquired with a Siemens mCT TOF PET/CT scanner in one bed position centered on the spheres. The total acquisition time was half the SPECT acquisition time (60 minutes), because the PET field-of-view (FOV) covering a whole liver generally requires two bed positions. PET images were reconstructed using the standard clinical 3D iterative attenuation-weighted ordinary Poisson OSEM algorithm (3 iterations, 21 subsets, 5 mm FWHM post-reconstruction filter), including resolution recovery and

TOF information, and correction for scattered and random events. The reconstructed voxel size was $2 \times 2 \times 2 \text{ mm}^3$.

Image contrast, noise, and the residual count error after attenuation and scatter correction were compared between SPECT, PET, and SPECT-MC. In the slice through the center of the coplanar spheres, six circular regions of interest (ROIs) (10, 13, 17, 22, 28, 37 mm diameter) were centered on the hot spheres and a circular ROI (30 mm diameter) was centered on the lung insert. A background ROI was defined in the same slice, consisting of all voxels within the phantom excluding the hot sphere ROIs dilated by 10 mm and the physical lung insert. For each of the six hot sphere ROIs, contrast recovery coefficients (Q_H) were calculated from

$$Q_H = \frac{C_H/C_B - 1}{R - 1} \times 100\% \quad (4.1)$$

Here, C_H is the mean intensity in the hot sphere ROI, C_B the mean intensity in the background ROI, and R the sphere-to-background activity concentration ratio. The residual count error in the lung insert (ΔC_{lung}) was calculated using

$$\Delta C_{lung} = \frac{C_{lung}}{C_B} \times 100\% \quad (4.2)$$

Here, C_{lung} is the mean intensity in the lung insert ROI. As a measure of image noise, the coefficient of variation (CV) was calculated as

$$CV = \frac{STDV_B}{C_B} \times 100\% \quad (4.3)$$

Here, $STDV_B$ is the standard deviation over all voxels in the background ROI.

Patient dosimetry

For clinical illustration, a comparison between SPECT-MC, SPECT, and PET was performed in 5 patients who underwent dual post-treatment imaging using both SPECT/CT and PET/CT techniques. This clinical study included retrospective analysis of data gathered as part of the quality control protocol for implementation of ^{90}Y PET as the standard post-radioembolization imaging procedure. The institutional review board of the University Medical Center Utrecht approved this retrospective study and waived the requirements for patient informed consent.

Radioembolization with ^{90}Y -labeled resin microspheres (SIR-Spheres, Sirtex, Sydney, Australia) was successfully performed in 5 consecutive patients (2 women, 3

men; median age 57 y; age range 43-76 y) according to the international consensus standards (23). The body-surface-area (BSA) method (23) was used to calculate the activities. All patient and treatment characteristics are summarized in Table 4.1.

The total scan time was 30 minutes for both SPECT and PET, the latter requiring two bed positions centered on the liver. Images were reconstructed with the settings described in the previous section. Possible accumulation of activity in organs other than the liver was evaluated on the post-treatment images. Liver ROIs were manually delineated on the CT images and liver + 1 cm ROIs were automatically created by adding a 1 cm margin. The SPECT, PET, and SPECT-MC reconstructed counts were converted into units of activity by normalization of the total counts in the liver + 1 cm ROIs to the activities administered to the patients. For each patient, one integrated SPECT/PET/SPECT-MC high-absorbed-dose (HAD) ROI was defined and applied to all reconstructed images. This ROI consisted of all voxels with an activity concentration of at least two times the mean whole liver concentration on (at least) one of the three images, to prevent a bias to one of the methods. Subsequently, low-absorbed-dose (LAD) ROIs were defined as the liver ROIs excluding the integrated HAD ROIs. Absorbed dose images were calculated by convolution of the activity images with the appropriate ^{90}Y 3D dose-point kernel (DPK) simulated with MCNPX, in accordance with MIRP Pamphlet 17 (24). Mean absorbed doses, standard deviations, and cumulative dose-volume-histograms (DVH) were calculated for the LAD and HAD ROIs.

The analysis described above was also performed on a sub-volume (approximately 2.5 L) of the phantom including the hot spheres, to enable comparison of the SPECT, PET, and SPECT-MC estimated radiation absorbed doses in the integrated LAD and HAD ROIs to the known absorbed dose in the phantom (i.e., the gold standard). The trend in performance of the three methods as observed in the clinical study was compared with the observed trend in the phantom data.

Table 4.1. Patient and treatment characteristics.

Patient	Primary ^a	Lobes ^b	V_{liver}^c (mL)	LTI ^c (%)	A_A^d (MBq)	A_S^d (MBq)	A_P^d (MBq)
1	CRC	W	2481	6	1714	1303	1602
2	CRC	W	1835	3	1852	1483	1499
3	NPC	W	1230	6	1199	922	1109
4	MC	L	383	5	281	216	270
5	HCC	W	3050	6	1177	916	927

^a Primary disease: CRC = colorectal carcinoma; NPC = nasopharyngeal carcinoma; MC = mammary carcinoma; HCC = hepatocellular carcinoma

^b Lobes treated: W = whole liver treatment; L = left lobar treatment

^c V_{liver} = volume of treated liver; LTI = Liver Tumor Involvement

^d A_A = Activity administered to the patient; A_S = A at time of SPECT; A_P = A at time of PET

4.2.3 Statistical analysis

Descriptive parameters are presented as mean and standard deviation and as median and range. Statistical differences in contrast recovery coefficients and mean absorbed doses between reconstruction methods were analyzed using the non-parametric Wilcoxon signed rank test for paired-data, since normality could not be assumed with the small sample sizes. All tests were performed with a significance level of 0.05.

4.3 Results

4.3.1 Validation of UMCS

In Figure 4.2, the profiles through the simulated and measured projection images are presented. Good agreement between UMCS and the measured projections was found in both the line source and the IQ phantom, although the tails of the UMCS profiles were slightly overestimated. The AUCs of the UMCS simulations were 5.7% and 1.3% higher than the AUCs of the measurements, for the line source and the IQ phantom, respectively. The AUC of the MCNPX profile was overestimated by less than 1% in comparison with the measured LSF. This excellent agreement validated the camera geometry used in MCNPX.

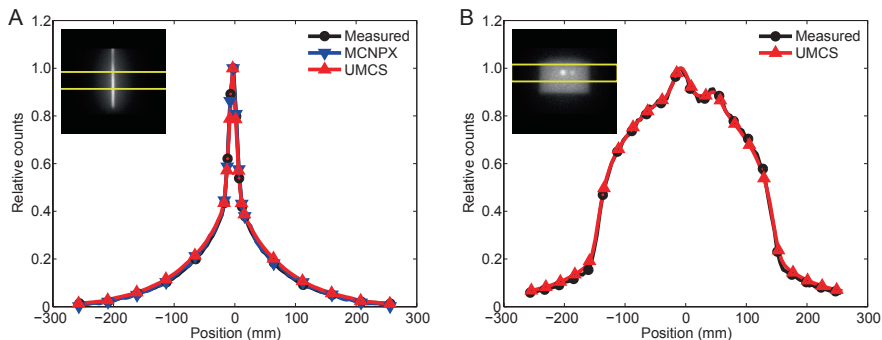


Figure 4.2. Profiles through the measured and simulated projection images of a line source centered in 20 cm scatter material (A) and the IQ phantom (B). The profiles were summed over the bins between the yellow lines and normalized to their maximum value.

4.3.2 Yttrium-90 Bremsstrahlung SPECT reconstruction

Image quality phantom experiment

Image contrast, the residual count error in the lung insert, and image noise are presented in Figure 4.3 for the three methods. Over all spheres, the SPECT-MC image contrast was significantly higher than SPECT ($p = 0.0313$). SPECT-MC image contrast was higher than PET in the two largest spheres and lower in the four smallest spheres. Over all spheres, image contrast did not differ significantly between PET and SPECT-MC ($p = 0.3125$). Image noise was 14%, 47%, and 43% for SPECT, PET, and SPECT-MC respectively. The residual error in the lung ROI was lowest for SPECT-MC; 15% versus 73% and 21% for SPECT and PET, respectively.

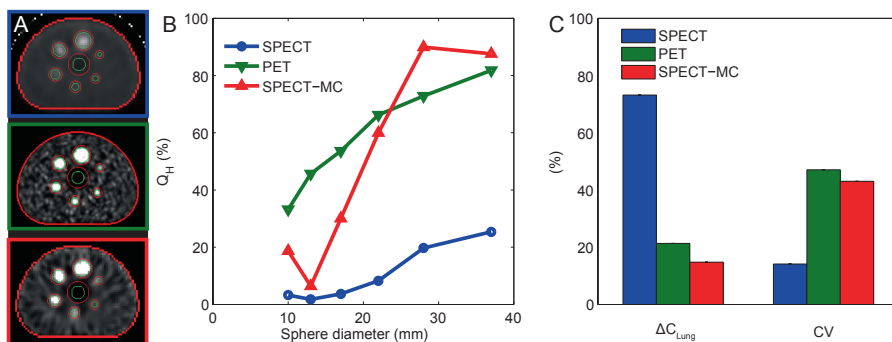


Figure 4.3. The left column shows the center slices through the SPECT (blue), PET (green), and SPECT-MC (red) reconstructed images, overlaid with the boundaries of the hot sphere and lung insert ROIs (green) and the background ROI (red) (A). All images are linearly window-leveled from 0 to 6 times the mean background intensity. The hot sphere contrast (Q_H) is plotted as a function of sphere diameter in (B). The residual count error in the lung insert (ΔC_{Lung}) and image noise (CV) are plotted in (C).

Patient dosimetry

No accumulation of activity outside the liver was found in any of the patients. Figure 4.4 gives an example of the SPECT, PET, and SPECT-MC estimated activity concentration distributions in a patient. In comparison with PET, the SPECT-MC image demonstrated a lower resolution, but was less affected by noise, which is in line with the results of the phantom study. However, in general, good correspondence was found between the PET and SPECT-MC activity distributions. In comparison with PET and SPECT-MC, the SPECT distribution showed a reduced peak activity concentration and higher background activity concentrations in the tails.

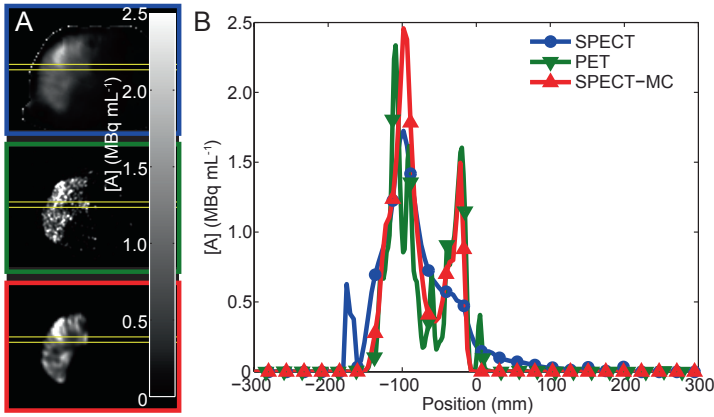


Figure 4.4. Transversal slices through the SPECT (blue), PET (green), and SPECT-MC (red) activity concentration images of patient 2 (A). Images are linearly window-leveled from 0 to 2.5 MBq mL⁻¹. The activity concentration distributions over the profiles (averaged over the bins between the yellow lines) are plotted in (B).

Figure 4.5 shows that the estimated mean absorbed doses in the LAD ROIs were consistently (i.e. for each patient) lower with SPECT-MC than with PET (median difference = -1.4 Gy, range = -1.9 – -0.2 Gy; $p = 0.0625$), but not than with SPECT (median difference = 2.9 Gy, range = -1.9 – 3.8 Gy; $p = 0.1250$). The mean absorbed doses in the HAD ROIs were consistently higher with SPECT-MC than with SPECT (median difference = 33.9 Gy, range = 21.7 – 45.9 Gy; $p = 0.0625$) and than with PET (median difference = 12.0 Gy, range = 11.2 – 12.7 Gy; $p = 0.0625$). The same trend is found for the SPECT, PET, and SPECT-MC estimated mean absorbed doses in the phantom (Figure 4.5). In both the LAD and HAD ROIs, SPECT-MC estimated mean absorbed doses were closest to the true dose. The absorbed dose images and the DVHs of patient 5 are shown in Figure 4.6 to illustrate the differences that were found between the methods.

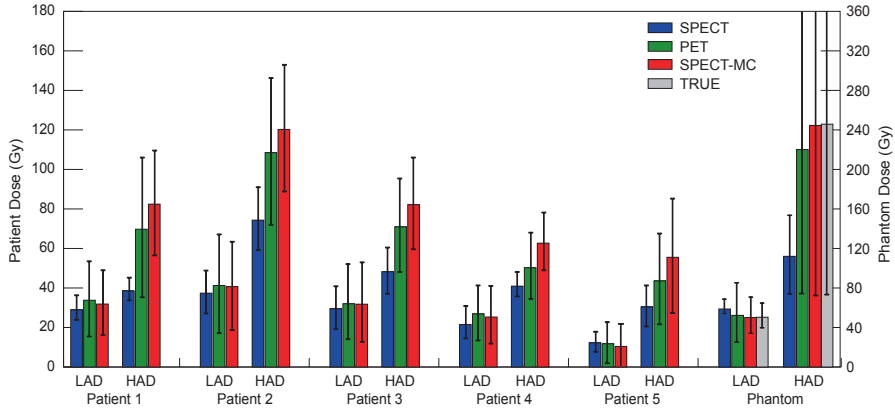


Figure 4.5. Bar plots of the SPECT (blue), PET (green), and SPECT-MC (red) estimated mean absorbed dose in the LAD and HAD ROIs for each patient and for the phantom. The TRUE mean absorbed doses in the LAD and HAD ROIs of the phantom are illustrated by the grey bars. The standard deviations of the mean voxel values are depicted by the error bars.

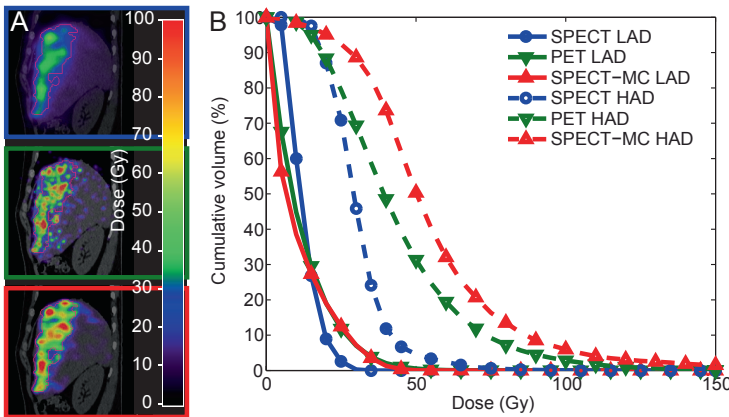


Figure 4.6. Sagittal slices through the SPECT (blue), PET (green), and SPECT-MC (red) estimated dose images of patient 5, fused with CT (A). The HAD ROI boundary is illustrated with the purple line. Dose-volume-histograms of the LAD and HAD ROIs are shown in panel (B).

4.4 Discussion

The objective of this work was to introduce and validate a new ⁹⁰Y SPECT reconstruction algorithm incorporating a fast Monte Carlo simulator to model the various image degrading factors. Small differences were observed between the UMCS-simulated projection images and the gamma camera measurements, which were probably due to assumptions made in the convolution-based forced detection (CFD) model. CFD was originally developed for ^{99m}Tc simulation, in which case almost all detected photons pass the collimator parallel to the septa. Mainly because of septal penetration, this

supposition is less accurate for ^{90}Y , which results in an underestimation of the final photon path length through the scatter object. This especially holds for the photons detected in the tails of the LSF in the line-source experiment, and explains the observed overestimation of the detection probability in this region. Other factors that may have limited the accuracy of the simulated projections include modeling the photon attenuation with a single μ_{central} for each scatter map, and the assumption of a circularly symmetric CDR, which ignores the star-shaped artifacts that are typical for septal penetration (25). Nevertheless, in general, good agreement was found between the simulated and measured projection images, which indicates that the impact of these effects was probably small and the image degrading effects were sufficiently accurately modeled.

Consequently, the image contrast of ^{90}Y SPECT-MC observed in the IQ phantom experiment was significantly higher than that of state-of-the-art clinical SPECT and the residual count error was reduced with 58 percent point. The contrast-to-noise ratio for all spheres was higher for SPECT-MC, even though the image noise was about three times lower for clinical SPECT. In comparison with PET, image noise and the residual count error in the lung insert were lower, which indicates good performance of the compensation models in SPECT-MC. Although PET showed higher image contrast in the smaller spheres, probably due to the higher resolution, contrast in the two largest spheres was higher for SPECT-MC. The SPECT and PET reconstruction parameters for optimal contrast recovery, which is more important for accurate quantification of local ^{90}Y content than reduction of noise, were determined in a previous study by our group (7). Accordingly, the number of iterations was varied between 1 and 120 in combination with various post-reconstruction filters (0, 5, 10 mm FWHM) to find the SPECT-MC reconstruction protocol for optimal contrast recovery. It should be noted that a different set of reconstruction parameters may lead to optimized images for diagnostic purposes. Surprisingly, the contrast recovery coefficients for SPECT-MC (and SPECT) did not monotonically increase with increasing sphere diameter. The contrast recovery coefficient for the 13 mm sphere was 12 percentage points lower than for the 10 mm sphere, and the contrast recovery coefficient for the 37 mm sphere was 2 percentage points lower than for the 28 mm sphere. The difference between the two smallest spheres may be a result of sampling errors, since the SPECT voxel size is relatively large in comparison with the small sphere diameters. Additionally, these small ROIs may have been substantially influenced by image noise. For the two largest spheres, image contrast had converged to its final value after 60 iterations. The relatively small difference that was found is within the

measurement error, which is expected to be 2 to 3% for the two largest spheres, based on the background noise.

The end point of this study is to compare the absorbed doses as estimated with SPECT, PET, and SPECT-MC technologies. A possible limitation with regard to calculation of the absorbed dose images may be the assumption of deposition of the complete administered activity in the liver + 1 cm ROI. Although it was validated that no activity was deposited in organs other than the liver in the SPECT and PET FOV, microspheres may (theoretically) have been deposited in organs outside the FOV, such as in the top of the lungs. A second limitation may be the use of the dose-point-kernel to convert the activity images to absorbed dose images. Although this approach is commonly used (24), it introduces extra blurring of already low-resolution images. A dose factor may be a better solution, especially for the SPECT(-MC) images. Despite these limitations, it was shown that both PET and SPECT-MC estimated mean absorbed doses were in good agreement with the true absorbed dose in the LAD and HAD ROIs of the phantom. In the clinical study, the highest mean absorbed dose estimates in the HAD ROIs were found for SPECT-MC, followed by PET and SPECT. In the LAD ROIs, slightly higher mean absorbed dose estimates were found for PET than for SPECT-MC. These results reflect the trend in radiation absorbed doses (and contrast recovery coefficients for larger ROIs) that was found in the phantom study.

Although the HAD ROIs did not necessarily coincide with tumorous tissue, the dosimetry results can, in general, be extrapolated to (larger) tumors, since in radioembolization higher activity concentrations are expected in tumorous tissue than in the healthy liver parenchyma. Consequently, underestimation of the dose on well-perfused tumors (i.e. high-absorbed-dose regions) is expected with the clinical SPECT reconstruction algorithm, while the dose on badly-perfused tumors is likely to be overestimated. Clinical consequences may include patient selection for re-treatment of 'undertreated' tumors and erroneous conclusions from dose-response analyses. SPECT-MC and PET-based tumor dose estimates are more accurate, although differences between PET and SPECT-MC are to be expected for small and large tumors, due to the different resolutions of the modalities. The clinical performance of both methods in terms of tumor-response and survival prediction should be compared in a large clinical study and is subject to further research.

The quantitative performance of SPECT-MC may be further improved by optimization of the detection window using Monte Carlo simulations, the use of photon energy-weighting to determine (voxel-specific) μ -values instead of μ_{central} , optimization of the number of scatter maps, and/or optimization of the number of

simulated photons. The impact of these possible improvements on the quality of the reconstructed images is subject to further research. The total reconstruction time per subset (15 angles) on a single core of a 1.8 GHz windows desktop computer was 102 seconds (22 seconds for simulation of the scatter map, 48 seconds for the application of the CDR, and 32 seconds for the back projection step). In general, reconstruction of post-treatment images is not as time-critical as reconstruction of diagnostic images. Still, the reconstruction time may be substantially reduced by saving certain information, such as rotated attenuation maps and CDR kernels, to the memory of a dedicated reconstruction computer, instead of redundantly recalculating it every iteration. Further speed-up may be achieved by parallelizing the detection step for each of the scatter maps, reduction of the number of simulated photons and/or using a faster, simplified forward projection model in the first few iterations (26).

We showed in a previous study that the image quality of state-of-the-art clinical PET is superior to Bremsstrahlung SPECT (7). In this study, we demonstrate that post-radioembolization images obtained with a standard SPECT/CT scanner can be of sufficiently high quantitative accuracy for dosimetry purposes, if reconstructed with adequate compensation models, especially for tumors larger than approximately 25 mm in diameter. The proposed method may be a cost-effective alternative to ^{90}Y PET, since a pre-treatment $^{99\text{m}}\text{Tc}$ -MAA SPECT scan is already part of the radioembolization procedure and thus no additional hardware investments are required.

4.5 Conclusion

We developed a new method for ^{90}Y SPECT reconstruction, including Monte Carlo-based compensation for scatter and attenuation effects, and energy-dependent modeling of the collimator-detector response. We showed in a phantom experiment that the proposed reconstruction method improved the quantitative accuracy of the Bremsstrahlung SPECT images in comparison with state-of-the-art clinical reconstruction. Evaluation of the estimated absorbed dose distribution in a small patient group indicated that the proposed SPECT method may be used as an alternative to ^{90}Y PET.

References

- 1 Vente MA, Wondergem M, van der Tweel I et al. Yttrium-90 microsphere radioembolization for the treatment of liver malignancies: a structured meta-analysis. *Eur Radiol*. 2009;19:951-959.
- 2 Kennedy AS, Salem R. Radioembolization (yttrium-90 microspheres) for primary and metastatic hepatic malignancies. *Cancer J*. 2010;16:163-175.
- 3 D'Arienzo M, Chiacramida P, Chiacchiararelli L et al. Y-90 PET-based dosimetry after selective internal radiotherapy treatments. *Nucl Med Comm*. 2012;33:633-640.
- 4 Walrand S, Lhommel R, Goffette P, Van den Eynde M, Pauwels S, Jamar F. Hemoglobin level significantly impacts the tumor cell survival fraction in humans after internal radiotherapy. *EJNMMI Research*. 2012;2:20.
- 5 Chang TT, Bourgeois AC, Balius AM, Pasciak AS. Treatment Modification of Yttrium-90 Radioembolization Based on Quantitative Positron Emission Tomography/CT Imaging. *J Vasc Intervent Radiol*. 2013;24:333-337.
- 6 Lhommel R, van Elmbt L, Goffette P et al. Feasibility of Y-90 TOF PET-based dosimetry in liver metastasis therapy using SIR-Spheres. *Eur J Nucl Med Mol Imaging*. 2010;37:1654-1662.
- 7 Elschot M, Vermolen BJ, Lam MGEH, de Keizer B, van den Bosch MAAJ, de Jong HWAM. Quantitative Comparison of PET and Bremsstrahlung SPECT for Imaging the In Vivo Yttrium-90 Microsphere Distribution after Liver Radioembolization. *PLoS ONE*. 2013;8:e55742.
- 8 Willowson K, Forwood N, Jakoby BW, Smith AM, Bailey DL. Quantitative Y-90 image reconstruction in PET. *Med Phys*. 2012;39:7153-7159.
- 9 van Elmbt L, Walrand S, Lhommel R, Jamar F, Pauwels S. Quantitative comparison between LYSO and BGO PET-tomographs in 90Y imaging. *Eur J Nucl Med Mol Imaging*. 2010;37:S293.
- 10 Elschot M, Nijssen JFW, Dam AJ, de Jong HWAM. Quantitative Evaluation of Scintillation Camera Imaging Characteristics of Isotopes Used in Liver Radioembolization. *PLoS ONE*. 2011;6:e26174.
- 11 Rong X, Du Y, Ljungberg M, Rault E, Vandenberghe S, Frey EC. Development and evaluation of an improved quantitative Y-90 bremsstrahlung SPECT method. *Med Phys*. 2012;39:2346-2358.
- 12 Hutton BF, Buvat I, Beekman FJ. Review and current status of SPECT scatter correction. *Phys Med Biol*. 2011;56:R85-R112.
- 13 Beekman FJ, de Jong HW, van GS. Efficient fully 3-D iterative SPECT reconstruction with Monte Carlo-based scatter compensation. *IEEE Trans Med Imaging*. 2002;21:867-877.
- 14 De Jong HWAM, Slijpen ETP, Beekman FJ. Acceleration of Monte Carlo SPECT simulation using convolution-based forced detection. *IEEE Trans Nucl Sci*. 2001;48:58-64.
- 15 Xiao JB, de Wit TC, Staelens SG, Beekman FJ. Evaluation of 3D Monte Carlo-based scatter correction for Tc-99m cardiac perfusion SPECT. *J Nucl Med*. 2006;47:1662-1669.
- 16 Xiao JB, de Wit TC, Zbijewski W, Staelens SG, Beekman FJ. Evaluation of 3D Monte Carlo-based scatter correction for Tl-201 cardiac perfusion SPECT. *J Nucl Med*. 2007;48:637-644.
- 17 Hendricks JS, McKinney GW, Waters LS et al. MCNPX Extensions, Version 2.5.0. 2005. Los Alamos, CA, Los Alamos National Laboratory Report LA-UR-05-2675.
- 18 Minarik D, Sjogreen GK, Ljungberg M. Evaluation of quantitative (90)Y SPECT based on experimental phantom studies. *Phys Med Biol*. 2008;53:5689-5703.
- 19 Rault E, Staelens S, Van HR, De BJ, Vandenberghe S. Fast simulation of yttrium-90 bremsstrahlung photons with GATE. *Med Phys*. 2010;37:2943-2950.

- 20 De Jong HWAM, Wang WT, Frey EC, Viergever MA, Beekman FJ. Efficient simulation of SPECT down-scatter including photon interactions with crystal and lead. *Med Phys*. 2002;29:550-560.
- 21 Kamphuis C, Beekman FJ, van Rijk PP, Viergever MA. Dual matrix ordered subsets reconstruction for accelerated 3D scatter compensation in single-photon emission tomography. *Eur J Nucl Med*. 1998;25:8-18.
- 22 Zeng GL, Gullberg GT. Unmatched projector/backprojector pairs in an iterative reconstruction algorithm. *IEEE Trans Med Imaging*. 2000;19:548-555.
- 23 Kennedy AS, Nag S, Salem R et al. Recommendations for radioembolization of hepatic malignancies using yttrium-90 microsphere brachytherapy: A consensus panel report from the Radioembolization Brachytherapy Oncology Consortium. *Int J Radiat Oncol Biol Phys*. 2007;68:13-23.
- 24 Bolch WE, Bouchet LG, Robertson JS et al. MIRD pamphlet No. 17: the dosimetry of nonuniform activity distributions--radionuclide S values at the voxel level. Medical Internal Radiation Dose Committee. *J Nucl Med*. 1999;40:11S-36S.
- 25 Staelens S, de WT, Beekman F. Fast hybrid SPECT simulation including efficient septal penetration modelling (SP-PSF). *Phys Med Biol*. 2007;52:3027-3043.
- 26 de Wit TC, Xiao JB, Beekman FJ. Monte Carlo-based statistical SPECT reconstruction: Influence of number of photon tracks. *IEEE Trans Nucl Sci*. 2005;52:1365-1369.

Chapter 5

Quantitative Monte Carlo-based holmium-166 SPECT reconstruction



Submitted for publication as:

M. Elschof, M.L.J. Smits, J.F.W. Nijssen, M.G.E.H. Lam, B.A. Zonnenberg, M.A.A.J. van den Bosch, M.A. Viergever, H.W.A.M. de Jong.

Quantitative Monte Carlo-based holmium-166 SPECT reconstruction.

Abstract

Objectives

Quantitative imaging of the radionuclide distribution is of increasing interest for microsphere radioembolization (RE) of liver malignancies, to aid treatment planning and dosimetry. For this purpose, holmium-166 (^{166}Ho) microspheres have been developed, which can be visualized with a gamma camera. The objective of this work is to develop and evaluate a new reconstruction method for quantitative ^{166}Ho SPECT, including Monte Carlo-based modeling of photon contributions from the full energy spectrum.

Methods

The Utrecht Monte Carlo System (UMCS) was adapted for ^{166}Ho and incorporated in a statistical reconstruction algorithm (SPECT-fMC). Photon scatter and attenuation for all photons sampled from the full ^{166}Ho energy spectrum were modeled during reconstruction by Monte Carlo simulations. The energy- and distance-dependent collimator-detector response was modeled using pre-calculated convolution kernels. Phantom experiments were performed to quantitatively evaluate contrast, noise, count errors, and activity recovery coefficients (ARCs) of SPECT-fMC in comparison with clinical reconstruction (SPECT-CLINICAL) and a previously developed Monte Carlo method (SPECT-hMC). Additionally, the impact of SPECT-fMC on whole-body recovered activities (A^{est}) and estimated radiation absorbed doses was evaluated using clinical SPECT data of six ^{166}Ho RE patients.

Results

At comparable noise level, SPECT-fMC images showed significantly higher contrast than SPECT-CLINICAL ($p = 0.031$) and SPECT-hMC ($p = 0.031$). The count error was reduced (SPECT-CLINICAL: 33%; SPECT-hMC: 34%; SPECT-fMC: 17%) and ARCs were improved (SPECT-CLINICAL: 23% - 77%; SPECT-hMC: 49% - 86%; SPECT-fMC 68% - 103%). SPECT-fMC recovered whole-body activities were most accurate ($A^{\text{est}} = 1.07 \times A - 5.80 \text{ MBq}$, $R^2 = 0.97$) and SPECT-fMC tumor absorbed doses were significantly higher than with SPECT-CLINICAL ($p = 0.031$) and SPECT-hMC ($p = 0.031$).

Conclusions

The quantitative accuracy of ^{166}Ho SPECT is improved by Monte Carlo-based modeling of the image degrading factors. Consequently, the proposed reconstruction method enables accurate estimation of the radiation absorbed dose in clinical practice.

5.1 Introduction

Intra-arterial microsphere radioembolization (RE) is used in clinical practice for treatment of unresectable liver malignancies (1-3). Currently, the majority of patients are being treated with commercially available glass (TheraSphere; MDS Nordion, Ontario, Canada) and resin microspheres (SIR-Spheres; Sirtex Medical, Sydney, Australia), labeled with the high-energy beta emitter yttrium-90 (^{90}Y). Quantitative imaging of the radioactive microspheres is indispensable for improving individualized treatment planning and post-treatment dosimetry, and has recently gained interest (4-6).

Poly(L-lactic acid) microspheres loaded with the high-energy beta-emitter holmium-166 (^{166}Ho), which have been developed at our institute as an alternative to ^{90}Y microspheres, possess favorable properties for quantitative imaging: the paramagnetic nature enables quantitative magnetic resonance imaging (MRI) and the emission of 81 keV gamma photons enables SPECT imaging (7-11). However, the complexity of the ^{166}Ho photon energy spectrum makes SPECT quantification of the local amount of microspheres challenging, since it includes multiple high-energy gamma (range 0.184 – 1.830 MeV; Table 5.1) and Bremsstrahlung (range 0 – 1.850 MeV) photons in addition to the 81 keV photopeak photons used for imaging (12).

In general, the SPECT image quality is degraded by photon attenuation and photon scatter in the patient, and by collimator-detector related effects like collimator scatter, lead X-rays, septal penetration, camera (back)scatter, and partial energy deposition in the crystal. The shape and magnitude of these effects depend on photon energy, tissue composition, collimator and detector characteristics, the distance between the source and the collimator, and energy window settings. As a result of the low energy of the ^{166}Ho photopeak (81 keV) and the abundance of high-energy photons, non-primary counts (i.e. scattered and collimator penetrated photons) contribute substantially to the ^{166}Ho detection window (12).

Model-based compensation for non-primary contributions is deemed most suitable for quantitative SPECT (13), but for ^{166}Ho this is complicated by the fact that photon attenuation, photon scatter, and the collimator-detector response (CDR) depend on photon energy. Additionally, the characteristic lead x-ray peak (74 keV) partially overlaps with the ^{166}Ho detection window (74.6 – 86.6 keV), which impedes the use of simple window-based scatter correction techniques. Monte Carlo-based reconstruction could potentially be a solution for ^{166}Ho , since it has the hypothetical advantage over more approximate methods that all physics can be included in

a detailed and accurate way, irrespective of photon energy (13). However, Monte Carlo-based reconstruction methods published to date do not include simulation of high-energy photon contributions to a lower-energy detection window (7,14,15). The aim of this study is to develop and evaluate a new reconstruction algorithm for quantitative ^{166}Ho SPECT, which makes use of a fast Monte Carlo simulator for 'on-the-fly' (i.e. during reconstruction) calculation of the scatter and attenuation effects in the patient, in combination with a distance- and energy-dependent model of the CDR. By means of phantom experiments, the quantitative accuracy of the proposed reconstruction method was evaluated and compared with current state-of-the-art clinical reconstruction software and with an approximate, hybrid reconstruction method that combines Monte Carlo-based scatter and attenuation correction for photopeak contributions with window-based correction for higher-energy contributions (7). Additionally, intrahepatic radiation absorbed doses were evaluated in six patients included in a phase I clinical trial, purposed to assess the safety and toxicity of ^{166}Ho RE in human liver metastases patients for the first time (16,17).

5.2 Materials and Methods

The Utrecht Monte Carlo System (UMCS) is a fully 3D Monte Carlo-based approach for simulation of gamma camera projection images of a radionuclide distribution. UMCS is fast enough to be incorporated in a statistical image reconstruction algorithm. The approach was validated for simulation of technetium-99m ($^{99\text{m}}\text{Tc}$) and thallium-201 (^{201}Tl) projections (14,15). An extensive description of standard UMCS is given elsewhere (18,19). For the purpose of this work, UMCS was adapted to simulate ^{166}Ho projection images including contributions of high-energy gamma photons and Bremsstrahlung photons.

5.2.1 UMCS physics

Two major adaptations to standard UMCS as published in (19) were made to make the approach suitable for simulation of ^{166}Ho projection images: the source photon energies were sampled from a continuous energy spectrum, and the energy-dependency of the CDR was modeled including all collimator-detector related image degrading effects. A schematic overview of UMCS physics is given in Figure 5.1.

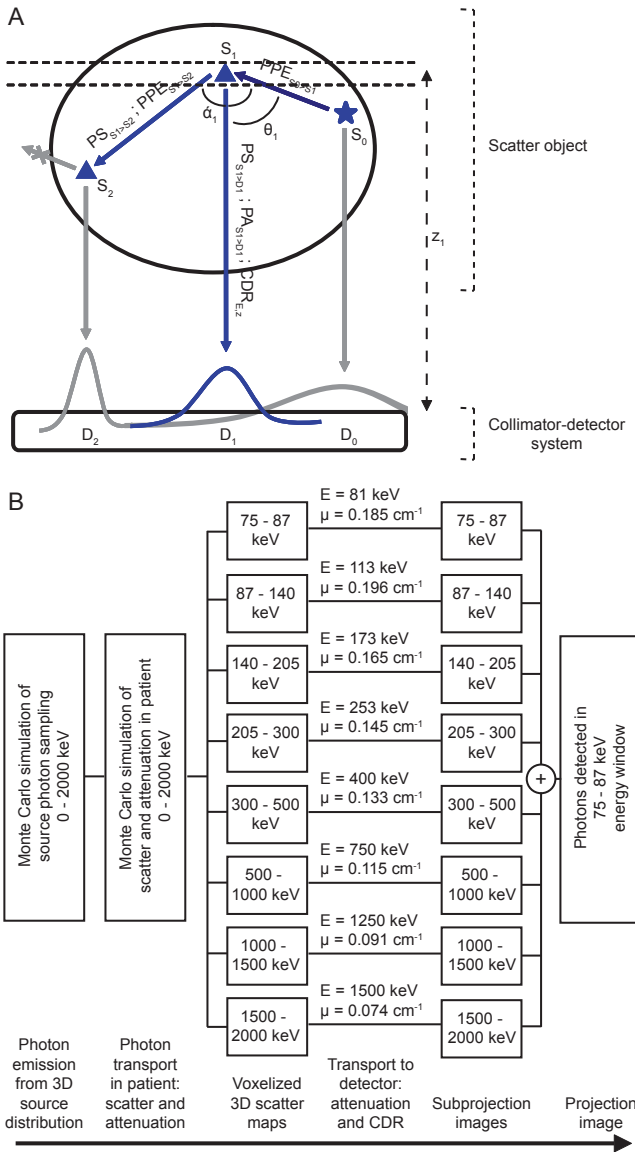


Figure 5.1. A schematic overview of the UMCS physics models in the scatter object and collimator-detector system (A) and of the subsequent steps involved in simulation of 2D projection images from a 3D source distribution (B). After photon emission (S_0), the probability of existence of a photon at scatter position S_n ($1 \leq n \leq 10$) is dependent on the probability of not having been absorbed photo-electrically (PPE) and on the probability of scattering over the angle α_n ($PS(\alpha_n)$). From each position S_n ($0 \leq n \leq 10$), a copy of the photon is forced to scatter over the angle θ_n towards the detector. The photon detection probability at position D_n depends on $PS(\theta_n)$, on the probability of not having been attenuated by the scatter object (PA_n), and on the shape and magnitude of the distance- (z_n) and energy-dependent CDR. In the last two steps (i.e. PA, CDR), which are performed after voxelwise binning of the photon intensities in energy-dependent 3D scatter maps, the attenuation coefficient is approximated by μ_{eff} (μ in (B)) and the CDR is approximated by the CDR of E_{central} (E in (B)).

Sampling of the source photon energy

The ^{166}Ho photon energy spectrum was implemented as a combination of the gamma peaks presented in Table 5.1 and the Bremsstrahlung photon energy spectrum resulting from interaction of the two high-energy beta-particles ($E_{\text{max}} = 1.77 \text{ MeV}$, 0.49 cps Bq^{-1} ; $E_{\text{max}} = 1.85 \text{ MeV}$, 0.50 cps Bq^{-1}) with water, which was simulated with MCNPX 2.5.0 (20). Beta particle physics were not simulated in UMCS and photon emission energies were directly sampled from a probability density function of the full ^{166}Ho energy spectrum. After photon emission, the standard UMCS scatter and attenuation models were used for calculation of photon transport in the patient.

Table 5.1. Energies and intensities of the gamma photons of ^{166}Ho decay. Data were obtained from the website of the National Nuclear Data Center (NNDC, Brookhaven National Laboratory, NY, USA, www.nndc.bnl.gov).

Energy (MeV)	Intensity (%)
0.081	6.6
0.184	1.6×10^{-3}
0.521	3.4×10^{-4}
0.674	1.9×10^{-2}
0.705	1.4×10^{-2}
0.786	1.2×10^{-2}
1.263	1.5×10^{-3}
1.379	9.2×10^{-1}
1.448	1.1×10^{-3}
1.528	8.9×10^{-5}
1.582	1.8×10^{-1}
1.662	1.2×10^{-1}
1.750	2.6×10^{-2}
1.830	8.0×10^{-3}

Simulation of scatter maps

Photons were first traced from their emission position to their final scatter position, via maximally 10 scatter events. For each scatter event, the photon intensity (i.e. probability of existence), position, direction, and energy were recorded. Next, for every camera angle, photons were forced to scatter from each recorded scatter position towards the detector and the photon intensities were updated accordingly (Figure 5.1 A). For the purpose of computationally efficient modeling of the distance- and energy-dependent CDR, the updated photon intensities were voxelwise binned in eight energy-dependent, voxelized 3D scatter maps, according to their energy after the last scatter event (i.e. towards the detector). The energy limits of the scatter maps are given in Figure 5.1 B.

Photon detection

Photons of all energies can potentially contribute to the 74.6 – 86.6 keV detection window, e.g. via collimator scatter or partial energy deposition in the crystal (12). These effects are modeled by the CDR in the photon detection model. To simulate energy-dependent photon detection, we made use of techniques that have been developed for fast simulation of down-scatter projections for dual-isotope SPECT (21). The detection process was performed separately for each of the eight scatter maps, in two steps. First, for each voxel of the scatter map the photon attenuation on the path to the detector was approximated by using a scatter map-specific effective attenuation coefficient (μ_{eff} , Figure 5.1 B). Second, the attenuation-corrected scatter maps were blurred layer-by-layer by convolution with the pre-calculated distance-dependent CDR, which represents the spatially varying detection probability of the corresponding photon energy (E_{central} , Figure 5.1 B) if measured in air (see next section). The blurred, attenuation-corrected scatter maps were summed over the direction perpendicular to the camera face to form 2D subprojection images. The sum of all energy-dependent subprojection images formed the final simulated projection image for the given camera angle.

Pre-calculation of CDR kernels

To generate pre-calculated CDRs, a model of a Siemens Symbia T16 (Siemens Healthcare, Erlangen, Germany) SPECT/CT camera head with a medium-energy low-penetration (MELP) collimator mounted was developed in MCNPX. For each of the eight central energies, the distance-dependent CDR to a point source in air was simulated using a 74.6 – 86.6 keV detection window.

Validation of UMCS

The accuracy of the UMCS-simulated ^{166}Ho projection images was evaluated in comparison with gamma camera measurements of a 1 mm diameter line source centered in PMMA scatter boxes of size 40 x 40 x 2 cm³ and 40 x 40 x 20 cm³, respectively. Measurements were performed with a single detector of a dual-headed Siemens Symbia T16 SPECT/CT system with MELP collimators mounted. Photons were detected in a 74.6 – 86.6 keV energy window on a 128 x 128 matrix with a pixel size of 4.8 x 4.8 mm². The distance between the collimator face and the line source was 10 cm for both measurements. Line-spread functions (LSFs) of a 10-cm-wide profile were compared visually and by means of the areas under the curves (AUCs) between the measurements and the UMCS simulations (10⁶ simulated photons).

The measured LSFs were also compared with MCNPX simulations (10^9 simulated photons), in order to validate the MCNPX camera geometry for calculation of the CDRs.

5.2.2 Holmium-166 SPECT reconstruction

UMCS was incorporated in a dual matrix ordered subsets expectation maximization reconstruction (OSEM) framework (22) for Monte Carlo-based ^{166}Ho SPECT reconstruction. In the forward projector, non-uniform photon attenuation, photon scatter, and the distance- and energy-dependent CDR were modeled, as explained above. The number of simulated photons per subset was 10^6 . In the back projection step photon attenuation was approximated with a single μ corresponding to that of the photopeak energy, photon scatter was not modeled, and the CDR was modeled as a distance-dependent Gaussian function (19). Such a dual matrix approach accelerates reconstruction, while having minimal impact on image quality (22). We will refer to the proposed ^{166}Ho SPECT reconstruction method as 'SPECT-fMC' in the remainder of this work.

Image quality

The NEMA 2007/IEC 2008 PET Image Quality (IQ) phantom was used for evaluation of reconstructed image quality. The phantom was filled with a ^{166}Ho activity concentration of 37 kBq ml^{-1} in the torso-shaped compartment, 292 kBq ml^{-1} in the six fillable coplanar spheres (inner diameter = 10, 13, 17, 22, 28, and 37 mm), and no activity in the cylindrical lung insert (outer diameter = 51 mm). SPECT data were acquired with the Siemens Symbia T16 SPECT/CT system, using 120 angles (60 per head) over a non-circular 360° orbit. In addition to the 74.6 – 86.6 keV photopeak window, a 110.9 – 125.1 keV down-scatter window was defined, which was required for the reconstruction methods used for comparison. The total activity at time of scanning was 378 MBq, which was within the linear range of the system (12). Ten cycles of 15 seconds per projection were acquired, adding up to a total acquisition time of 150 minutes. The 10 projections per camera angle were summed to obtain a count density similar to the expected clinical count density, under the assumption of a 30 minutes-long acquisition of a ^{166}Ho RE patient with a 2 liter-large liver containing approximately 400 MBq at time of scanning (i.e. $[A] = 200 \text{ kBq ml}^{-1}$).

SPECT-fMC data were reconstructed to a voxel size of $4.8 \times 4.8 \times 4.8 \text{ mm}^3$ using 20 iterations with 8 subsets. No post-reconstruction filter was applied. Two reconstruction algorithms were included in this study for comparison: state-of-

the-art clinical SPECT reconstruction (SPECT-CLINICAL) and hybrid Monte-Carlo/window-based reconstruction (SPECT-hMC), which was developed and previously used in our institute (7,9,10). SPECT-CLINICAL was performed with Siemens FLASH3D (20 iterations, 8 subsets, no post-reconstruction filter). Before reconstruction, the down-scatter projections were pixelwise subtracted from the photopeak projections, corrected for the difference in energy window width. Attenuation correction was performed with an effective broad-beam linear attenuation coefficient. SPECT-hMC reconstruction (20 iterations, 8 subsets, no post-reconstruction filtering) was performed using the same OSEM reconstruction framework as used for SPECT-fMC, but now with the standard UMCS settings for photopeak simulation in combination with a down-scatter correction window. An extensive description of the method is given elsewhere (7).

Image contrast, image noise, and the residual count error in the lung insert were compared for SPECT-CLINICAL, SPECT-hMC, and SPECT-fMC. In the slice through the center of the coplanar spheres, six circular regions of interest (ROIs) (10, 13, 17, 22, 28, 37 mm diameter) were centered on the hot spheres and a circular ROI (30 mm diameter) was centered on the lung insert. A background ROI was defined in the same slice consisting of all voxels within the phantom excluding the physical lung insert and the hot sphere ROIs dilated by 10 mm. For each of the six hot sphere ROIs, contrast recovery coefficients (Q_H) were calculated using

$$Q_H = \frac{C_H/C_B - 1}{R - 1} \times 100\% \quad (5.1)$$

Here, C_H is the mean intensity in the hot sphere ROI, C_B the mean intensity in the background ROI, and R the sphere-to-background activity concentration ratio. The residual count error in the lung insert (ΔC_{lung}) was calculated as

$$\Delta C_{lung} = \frac{C_{lung}}{C_B} \times 100\% \quad (5.2)$$

with C_{lung} the mean intensity in the lung insert ROI. As a measure of image noise, the coefficient of variation (CV) was calculated from

$$CV = \frac{STDV_B}{C_B} \times 100\% \quad (5.3)$$

Here, $STDV_B$ is the standard deviation over all voxels in the background ROI.

Activity quantification

Calibration factors for absolute activity quantification with SPECT were obtained from a cylindrical water phantom (length = 22 cm, radius = 10.5 cm), uniformly filled with 466 MBq of ^{166}Ho . SPECT data were acquired in 30 minutes (one cycle, 30 seconds per projection), with the other acquisition and reconstruction settings as described in the previous section. Calibration factors (cps MBq^{-1}) were determined for each of the three reconstruction protocols by dividing the total reconstructed counts in the phantom by the imposed phantom activity.

Activity recovery coefficients (ARCs) as a function of sphere volume were determined using a cylindrical water phantom (length = 18.5 cm, radius = 10.75 cm) containing five fillable spherical inserts. The spheres were filled with a ^{166}Ho activity concentration of 695 kBq ml^{-1} and there was no activity in the background compartment. The measured volumes of the spheres were 1.96, 4.10, 7.99, 24.12, and 106.21 ml. SPECT data were acquired and reconstructed with the same settings as for the uniform cylinder phantom. A CT scan of the phantom was used to manually delineate five 3D ROIs on the inner boundaries of the spheres. For each sphere, the ARC was calculated as

$$ARC = \frac{A_{ROI}}{A_{SPHERE}} \times 100\% \quad (5.4)$$

with A_{ROI} the activity (MBq) recovered in the ROI and A_{SPHERE} the real activity (MBq) in the sphere.

Patient dosimetry

The clinical performance of SPECT-fMC reconstruction was evaluated in comparison with SPECT-CLINICAL and SPECT-hMC in six patients that were part of a phase I dose-escalation study on ^{166}Ho RE for patients with unresectable, chemorefractory liver metastases. Study design and clinical results (patient characteristics, toxicity and adverse events) of the study have been described previously (16,17). The study was approved by the institutional review board and registered with Clinicaltrials.gov, number NCT01031784. In total, 15 patients were included in the phase I study. Nuclear imaging of the first nine patients was performed with a Philips FORTE™ SPECT system (Philips Medical Systems, Milpitas, CA, USA) whereas the last six patients were scanned on a Siemens Symbia T16 SPECT/CT system. Since the proposed SPECT reconstruction method requires a CT-derived attenuation map, only the SPECT data of the last six patients are presented in this work. Patient and treatment characteristics of these patients are provided in Table 5.2.

Table 5.2. Patient and treatment characteristics.

Patient	Primary ^a	V _{liver} ^b (ml)	LTI ^b (%)	A _{AS} ^c (MBq)	A _{SS} ^c (MBq)	A _{AT} ^c (MBq)	A _{ST} ^c (MBq)
1	CRC	3129	57.8	273	259	9523	255
2	CRC	2120	20.9	245	236	6701	302
3	CRC	2473	13.5	261	251	7900	375
4	CRC	1471	8.0	272	253	6825	353
5	UM	2816	45.9	275	265	10274	292
6	UM	1467	1.9	251	237	7172	356

^a Primary disease: CRC = colorectal carcinoma; UM = uveal melanoma

^b V_{liver} = volume of treated liver; LTI = Liver Tumor Involvement

^c A_{AS} = scout activity administered to the patient; A_{SS} = scout activity at time of pre-treatment SPECT; A_{AT} = total activity administered to the patient; A_{ST} = total activity at time of post-treatment SPECT

The ¹⁶⁶Ho RE procedure included a standard work-up angiography for prophylactic coil-embolization of non-target vessels, followed by administration of ^{99m}Tc macroaggregated albumin (^{99m}Tc-MAA) particles (0.8 mg, TechneScan LyoMaa, Mallinckrodt Medical B.V., Petten, the Netherlands) through a microcatheter in the proper, left or right hepatic artery. The ^{99m}Tc-MAA distribution was evaluated with planar nuclear imaging and SPECT/CT. If there was no extrahepatic activity, except for a lung shunt fraction of maximally 20%, the patients were scheduled for treatment. The required ¹⁶⁶Ho activity (A) was calculated using

$$A(\text{GBq}) = \frac{D(\text{Gy})}{15.87(\text{J GBq}^{-1})} \times m_{\text{LIVER}}(\text{kg}) \quad (5.5)$$

with D the scheduled whole-liver absorbed dose (patients 1-3: 60 Gy; patients 4–6: 80 Gy), m_{LIVER} the liver mass derived from contrast-enhanced CT, and 15.87 the total energy released per unit of activity ¹⁶⁶Ho. On the day of treatment, a microcatheter was placed under angiography in the exact same position as used for ^{99m}Tc-MAA administration and a scout dose of ¹⁶⁶Ho microspheres was administered to the patient, followed by evaluation of the microsphere distribution with planar nuclear imaging and SPECT/CT. Upon confirmation of a safe scout dose distribution, a treatment dose of ¹⁶⁶Ho microspheres was administered under angiography. Post-treatment SPECT/CT imaging was performed five to six days after administration of the ¹⁶⁶Ho treatment dose.

¹⁶⁶Ho SPECT data were acquired in 30 minutes with the previously described settings and reconstructed with SPECT-CLINICAL, SPECT-hMC, and SPECT-fMC. Reconstructed counts were converted into units of activity by multiplication with the appropriate calibration factor derived from the uniformly filled phantom experiment.

Subsequently, absorbed dose images were calculated by convolution of the activity images with a ^{166}Ho 3D dose-point kernel (DPK) simulated with MCNPX, in accordance with MIRD pamphlet No.17 (23). Each patient's liver contour, as well as the contours of all discernible tumors, were manually segmented on T_2 -weighted turbo spin echo (TSE) MR images (Achieva, Philips Healthcare, Best, the Netherlands; scanning parameters: $B = 1.5\text{ T}$, $\text{TR/TE} = 830/80\text{ ms}$, $\text{voxelsize} = 2 \times 2 \times 6\text{ mm}^3$) using the in-house developed radiotherapy-planning software package Volumetool (24). Non-tumor ROIs were defined as the liver ROIs excluding the tumor ROIs. Whole body contours were automatically extracted and liver + 5 mm ROIs were automatically created by adding 5 mm margins to the liver ROIs. Subsequently, the contours of the liver ROIs were manually registered to the low-dose CT images that were intrinsically aligned with the activity and dose images. The total recovered activities in the whole body ROIs and in the liver + 5 mm ROIs were calculated, as well as mean absorbed doses plus standard deviations and cumulative dose-volume-histograms (DVHs) of the non-tumor and tumor ROIs. Additionally, peak absorbed dose values were calculated for the tumor ROIs, which were defined as the mean activity concentration in the 1 cm^3 volume with the highest activity concentration, in accordance with the PERCIST criteria (25).

Statistical analysis

Descriptive parameters are presented as mean and standard deviation and as median and range. Statistical differences in contrast recovery coefficients and absorbed doses between reconstruction methods were analyzed using the non-parametric Wilcoxon signed rank test for paired-data (significance level of 0.05), since normality could not be assumed with the small sample sizes. Correlations between administered (A) and recovered activities (A^{est}) were investigated by linear regression ($A^{\text{est}} = a \times A + b$).

5.3 Results

5.3.1 Validation of UMCS

In Figure 5.2, the profiles through the simulated and measured projection images of the line source centered in $40 \times 40 \times 2\text{ cm}^3$ (A) and $40 \times 40 \times 20\text{ cm}^3$ PMMA (B) are presented. Good agreement between the UMCS-simulated and measured LSFs can be appreciated for both experiments, which is supported by the small differences in the AUCs; the AUCs of the UMCS simulations were 0.4% ($40 \times 40 \times 2\text{ cm}^3$ PMMA) and 2.3% ($40 \times 40 \times 20\text{ cm}^3$ PMMA) higher than the AUCs of the measurements.

Differences between the AUCs of the MCNPX-simulated profiles and the measured profiles were also small; the MCNPX-simulated LSFs were overestimated by 2.8% and 1.5% for the line source centered in $40 \times 40 \times 2 \text{ cm}^3$ and $40 \times 40 \times 20 \text{ cm}^3$ PMMA, respectively. This good agreement validated the camera geometry used in MCNPX.

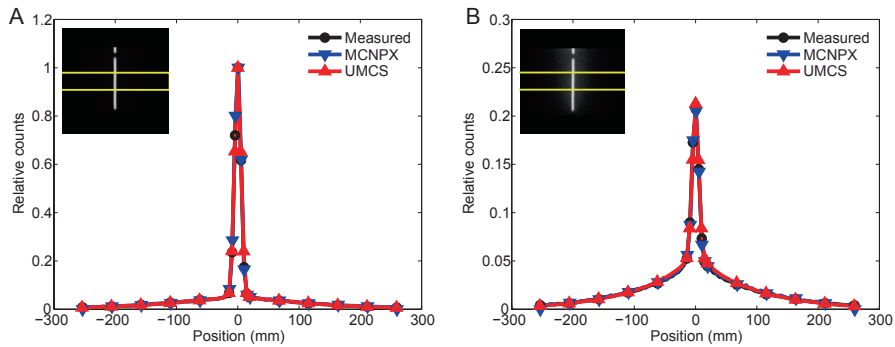


Figure 5.2. Profiles through the measured and simulated projection images of a line source centered in $40 \times 40 \times 2 \text{ cm}^3$ scatter material (A) and in $40 \times 40 \times 20 \text{ cm}^3$ scatter material (B). Counts in panel A and B were normalized to the maximum intensities in panel A.

5.3.2 Holmium-166 SPECT reconstruction

Image quality

Image contrast, the residual count error in the lung insert, and image noise are presented in Figure 5.3 for the three reconstruction methods. Over all spheres, SPECT-fMC image contrast was significantly higher than that of SPECT-CLINICAL ($p = 0.031$) and SPECT-hMC ($p = 0.031$). Image noise was slightly higher in SPECT-fMC images (37%) than in SPECT-CLINICAL (33%) and SPECT-hMC images (32%). The residual count error in the lung insert was reduced from 33% and 34% for SPECT-CLINICAL and SPECT-hMC, respectively, to 17% for SPECT-fMC.

SPECT quantification

Calibration factors for absolute activity quantification were successfully determined for each of the three reconstruction protocols. From Figure 5.4 it can be appreciated that the ARCs were consistently (but not significantly) higher for SPECT-fMC than for SPECT-CLINICAL ($p = 0.063$) and SPECT-hMC ($p = 0.063$). In comparison with SPECT-CLINICAL / SPECT-hMC, SPECT-fMC reduced the errors on the ARCs with 45 / 19 percentage point (pp), 30 / 19 pp, 31 / 18 pp, 29 / 17 pp, and 20 / 11 pp, for the 1.96, 4.10, 7.99, 24.12, and 106.21 ml spheres, respectively.

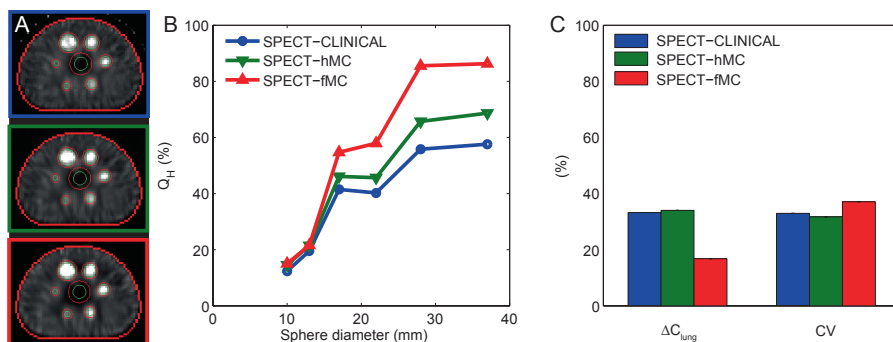


Figure 5.3. The left column shows the center slices through the SPECT-CLINICAL (blue), SPECT-hMC (green), and SPECT-fMC (red) reconstructed images, overlaid with the boundaries of the hot sphere and lung insert ROIs (green) and the background ROI (red) (A). All images are linearly window-leveled from 0 to 6 times the mean background intensity. The hot sphere contrast (Q_H) is plotted as a function of sphere diameter (B). The residual count error in the lung insert (ΔC_{lung}) and image noise (CV) are plotted in (C).

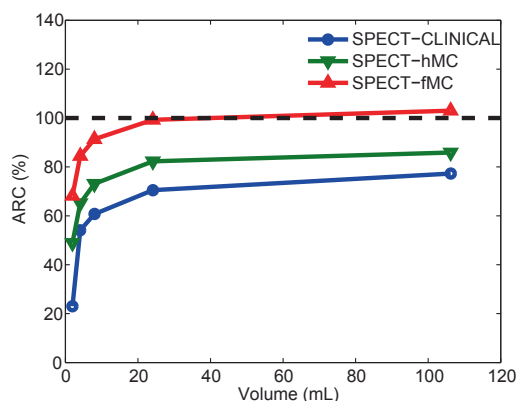


Figure 5.4. Activity recovery coefficients (ARC) as a function of sphere volume.

Patient dosimetry

Figure 5.5 shows the recovered activities in the whole body ROIs plotted as a function of the administered activities at time of scanning. Linear fit parameters were $a = 1.444$ and $b = -32.918$ (95% C.I.: $a = (1.152 ; 1.736)$, $b = (-117.523 ; 51.687)$; $R^2 = 0.924$, $p < 0.001$) for SPECT-CLINICAL, $a = 1.318$ and $b = -37.964$ (95% C.I.: $a = (1.041 ; 1.596)$, $b = (-118.294 ; 42.367)$; $R^2 = 0.918$, $p < 0.001$) for SPECT-hMC, and $a = 1.067$ and $b = -5.802$ (95% C.I.: $a = (0.928 ; 1.205)$, $b = (-45.943 ; 34.340)$; $R^2 = 0.967$, $p < 0.001$) for SPECT-fMC. The SPECT-fMC fitting parameters were closest to 1 (a) and 0 (b), which confirmed the quantitative superiority of SPECT-fMC to the other methods. This was also reflected by the median errors (ranges) on the recovered activities in the whole body ROIs, which were 34.7% (17.5% – 46.8%), 20.0% (1.6% – 30.5%), and 5.5% (-1.3% – 9.2%) for SPECT-CLINICAL, SPECT-hMC, and SPECT-fMC, respectively. Smaller

differences were observed between the administered activities and the recovered activities in the liver + 5 mm ROIs: -2.9% (-10.3% – 8.9%), -9.1% (-18.3% – 0.5%), and -0.8% (-6.4% – 4.8%) for SPECT-CLINICAL, SPECT-hMC, and SPECT-fMC, respectively.

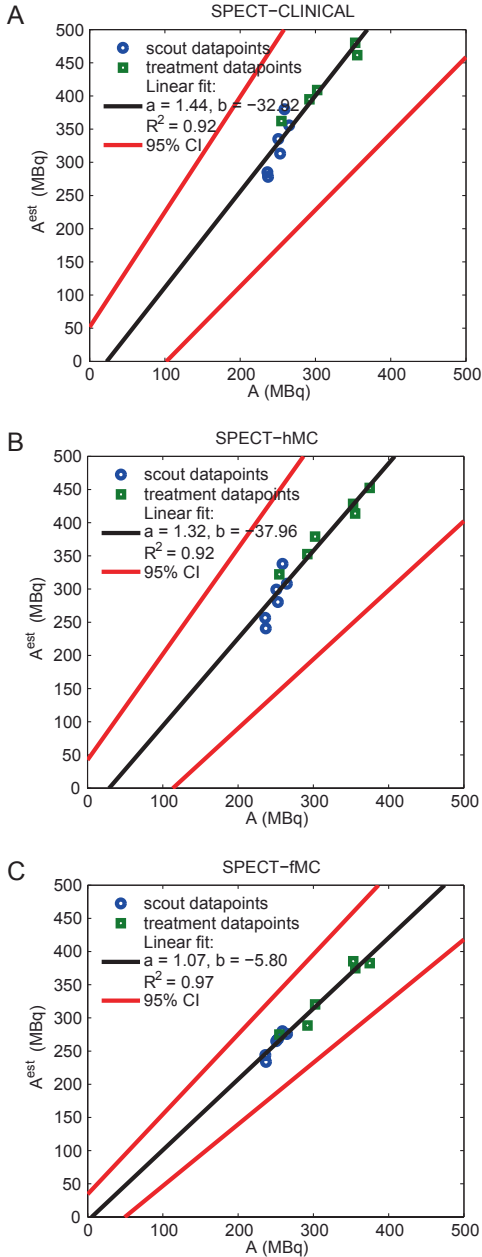


Figure 5.5. The activity recovered in the whole-body ROIs (A^{est}) on the SPECT-CLINICAL (A), SPECT-hMC (B), and SPECT-fMC images (C), plotted as a function of the administered activity at time of scanning (A). The scout dose data points are depicted by the blue circles and the treatment data points are represented by the green squares. The black lines represent the best linear fit ($A^{\text{est}} = a \times A + b$) through the data points and the red lines represent the 95% confidence intervals (C.I.).

The estimated radiation absorbed doses in the non-tumor and tumor ROIs, as a result of the total activity administered to the patient (i.e. scout + treatment dose), are shown in Figure 5.6. The absorbed doses in the non-tumor ROIs did not differ significantly between SPECT-fMC and SPECT-CLINICAL (median difference = 1.0 Gy, range = -4.4 – 5.0 Gy; $p = 0.6875$) and between SPECT-fMC and SPECT-hMC (median difference = 2.1 Gy, range = -0.3 – 7.1 Gy; $p = 0.063$). The estimated mean absorbed doses in the tumor ROIs were significantly higher with SPECT-fMC than with SPECT-CLINICAL (median difference = 3.3 Gy, range = 0.7 – 7.4 Gy; $p = 0.031$) and significantly higher with SPECT-fMC than with SPECT-hMC (median difference = 5.4 Gy, range = 3.3 – 9.1 Gy; $p = 0.031$). The estimated peak absorbed doses in the tumor ROIs were also significantly higher with SPECT-fMC than with SPECT-CLINICAL (median difference = 29.6 Gy, range = 4.5 – 108.5 Gy; $p = 0.031$) and than with SPECT-hMC (median difference = 16.2 Gy, range = 7.6 – 74.3 Gy; $p = 0.031$). The absorbed dose images and DVHs of patient 5 are shown in Figure 5.7, to illustrate the differences observed between the reconstruction methods.

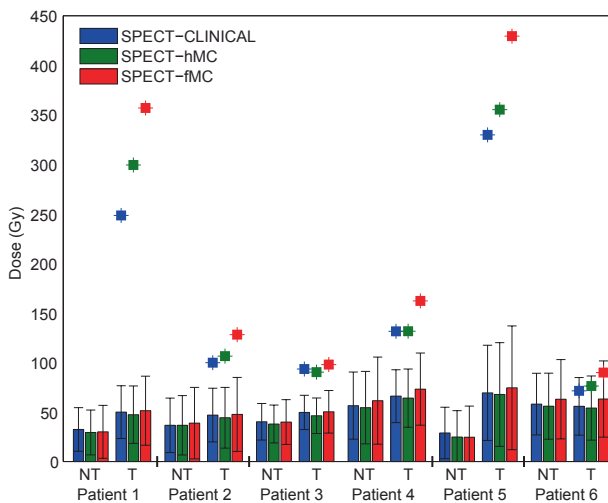


Figure 5.6. Bar plots of the SPECT-CLINICAL, SPECT-hMC, and SPECT-fMC estimated mean absorbed doses in the non-tumor and tumor ROIs of each patient. The standard deviations of the means are depicted by the error bars. Data points represent the peak absorbed doses in the tumor ROIs.

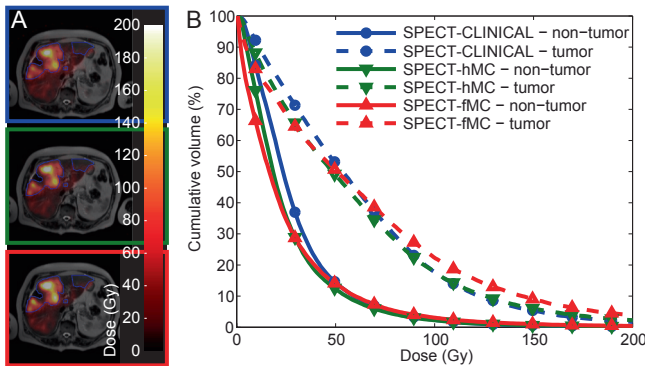


Figure 5.7. Transversal slices through the SPECT-CLINICAL (blue), SPECT-hMC (green), and SPECT-fMC-based (red) dose images of patient 5, fused with CT (A). The tumor ROI boundary is illustrated with the purple line. Dose-volume-histograms of the non-tumor and tumor ROIs are shown in panel (B).

5.4 Discussion

The objective of this work was to develop and validate a new ^{166}Ho SPECT reconstruction method, including fast Monte Carlo simulation of photon contributions from the complete energy spectrum. Good agreement was observed between UMCS-simulated projection images and measured projection images, which validates the energy-dependent photon transport and detection models used in UMCS. Overall, the proposed reconstruction method significantly improved the image quality and the quantitative accuracy of ^{166}Ho SPECT. At a comparable noise level, image contrast was significantly higher in SPECT-fMC images than in SPECT-hMC and SPECT-CLINICAL images. The residual count error in the lung insert was substantially reduced, which indicates that the compensation models in SPECT-fMC were improved in comparison with SPECT-hMC and SPECT-CLINICAL. Additionally, the improved quantitative accuracy of SPECT-fMC was demonstrated by the higher ARCs in comparison with the other methods.

The results of the phantom experiments were endorsed by the patient study, which showed that the recovered activities in the whole body ROIs were accurate within 10% for SPECT-fMC. It was assumed that the total recovered activity was detected in the field of view (FOV) of the camera. As a result of arteriovenous shunting, activity may also have been present in the upper parts of the lungs, which were located outside the SPECT FOV. However, the recovered activity in the lung bases was much less than 1% of the total recovered activity for all patients (data not shown), indicating that the activity outside the FOV was probably very small, if not negligible. A median overestimation of the total activity of 5.5% was still observed

with SPECT-fMC, which may be the result of the positive bias commonly observed in low-count regions of OSEM-reconstructed images (26,27). The larger median errors on the whole body activities recovered with SPECT-CLINICAL (34.7%) and SPECT-hMC (20.0%) can probably be attributed to suboptimal compensation for photon scatter, attenuation and collimator-detector effects, which resulted in substantial overestimation of the background activity.

The SPECT-fMC-estimated mean and peak tumor absorbed doses were significantly higher than those of SPECT-CLINICAL and SPECT-hMC. Although the actual dose distribution is unknown in patients, the SPECT-fMC-estimated tumor absorbed doses can probably be regarded as the most accurate estimates, given the method's superiority with regard to recovery of image contrast and quantification of activity, as demonstrated in the phantom study. Accurate post-treatment assessment of the radiation absorbed dose to the tumors and functional liver parenchyma can support predicting of toxicity, efficacy, and patient survival (4-6). Additionally, quantitative evaluation of the intrahepatic distribution of the ^{166}Ho scout dose may pave the way for substantial improvements in individualized treatment planning. The currently used methods for treatment planning of ^{90}Y RE with glass or resin microspheres do not consider patient specific parameters other than whole liver mass (glass microspheres) and body surface area (BSA) and fractional liver involvement (resin microspheres) (28). However, the distribution of the treatment dose ultimately determines the radiation absorbed dose to tumorous and healthy liver tissue, and thereby the safety and efficacy of the treatment. Proposed individualized treatment planning methods attempt to find an optimal balance between liver toxicity and treatment efficacy, by using the $^{99\text{m}}\text{Tc}$ -MAA distribution as a predictor of the microsphere distribution over tumorous and healthy liver tissue (partition modeling) (29-31). However, agreement between $^{99\text{m}}\text{Tc}$ -MAA tumor-to-non-tumor activity concentration ratios (T/N ratio) and ^{90}Y microspheres T/N ratios has never been quantitatively demonstrated. On the contrary, the available literature on microsphere rheology suggests that flow-based distribution heterogeneities are likely to be overestimated with $^{99\text{m}}\text{Tc}$ -MAA, due to the differences in size between the $^{99\text{m}}\text{Tc}$ -MAA particles (10 – 120 μm) and ^{90}Y glass (20 – 30 μm) and resin microspheres (20 – 60 μm) (32). This issue may be avoided with ^{166}Ho microsphere RE, since the same quantifiable microspheres can be used for scout dose and treatment. The performance of the ^{166}Ho scout dose, in comparison with the $^{99\text{m}}\text{Tc}$ -MAA scout dose, is currently being investigated in our institute.

The proposed SPECT reconstruction algorithm can be used for accurate quantification of the ^{166}Ho microsphere scout and treatment dose. The total

reconstruction time on a single core of a 1.8 GHz windows desktop computer was approximately 4.5 hours for 20 iterations with 8 subsets. The reconstruction time should preferably be reduced, in particular for reconstruction of the scout dose images, which should be readily available for treatment planning. The reconstruction of post-treatment images is typically less time-critical. Reconstruction times may be substantially reduced by saving certain information, such as rotated attenuation maps and CDR kernels, to the memory of a dedicated reconstruction computer, instead of redundantly recalculating it every iteration. Further speed-up may be achieved by parallelization of the detection step for each of the scatter maps, reduction of the number of simulated photons and/or using a faster, simplified forward projection model in the first few iterations (33). Optimization of the reconstruction method is subject of further research.

5.5 Conclusion

We developed and validate a new reconstruction algorithm for quantitative ^{166}Ho SPECT, which includes Monte Carlo-based compensation for scatter and attenuation in the patient, and distance- and energy-dependent modeling of the collimator-detector response. The proposed method significantly improved the quantitative accuracy of the ^{166}Ho SPECT images in comparison with existing reconstruction methods. Additionally, the proposed method was able to accurately quantify the activities administered to six patients treated with ^{166}Ho microsphere radioembolization. Consequently, the proposed reconstruction method enables accurate estimation of the radiation absorbed dose on tumorous and healthy liver parenchyma, which is of interest for individualized treatment planning and evaluation.

References

- 1 Vente MA, Wondergem M, van der Tweel I et al. Yttrium-90 microsphere radioembolization for the treatment of liver malignancies: a structured meta-analysis. *Eur Radiol.* 2009;19:951-959.
- 2 Coldwell D, Sangro B, Salem R, Wasan H, Kennedy A. Radioembolization in the Treatment of Unresectable Liver Tumors Experience Across a Range of Primary Cancers. *Am J Clin Oncol-Canc.* 2012;35:167-177.
- 3 Kennedy AS, Salem R. Radioembolization (yttrium-90 microspheres) for primary and metastatic hepatic malignancies. *Cancer J.* 2010;16:163-175.
- 4 Strigari L, Sciuto R, Rea S et al. Efficacy and Toxicity Related to Treatment of Hepatocellular Carcinoma with Y-90-SIR Spheres: Radiobiologic Considerations. *J Nucl Med.* 2010;51:1377-1385.
- 5 D'Arienzo M, Chiamarida P, Chiacchiararelli L et al. Y-90 PET-based dosimetry after selective internal radiotherapy treatments. *Nucl Med Commun.* 2012;33:633-640.
- 6 Walrand S, Lhommel R, Goffette P, Van den Eynde M, Pauwels S, Jamar F. Hemoglobin level significantly impacts the tumor cell survival fraction in humans after internal radiotherapy. *EJNMMI Res.* 2012;2:20.
- 7 de Wit TC, Xiao J, Nijsen JF et al. Hybrid scatter correction applied to quantitative holmium-166 SPECT. *Phys Med Biol.* 2006;51:4773-4787.
- 8 Nijsen JF, Seppenwoolde JH, Havenith T, Bos C, Bakker CJ, van het Schip AD. Liver tumors: MR imaging of radioactive holmium microspheres--phantom and rabbit study. *Radiology.* 2004;231:491-499.
- 9 Seevinck PR, Seppenwoolde JH, de Wit TC et al. Factors affecting the sensitivity and detection limits of MRI, CT, and SPECT for multimodal diagnostic and therapeutic agents. *Anticancer Agents Med Chem.* 2007;7:317-334.
- 10 Maat G, Seevinck P, Elschot M et al. MRI-based biodistribution assessment of holmium-166 poly(L-lactic acid) microspheres after radioembolisation. *Eur Radiol.* 2012;1-9.
- 11 Seevinck PR, van de Maat GH, de Wit TC, Vente MAD, Nijsen JFW, Bakker CJG. Magnetic Resonance Imaging-Based Radiation-Absorbed Dose Estimation of Ho-166 Microspheres in Liver Radioembolization. *Int J Radiat Oncol Biol Phys.* 2012;83:E437-E444.
- 12 Elschot M, Nijsen JFW, Dam AJ, de Jong HWAM. Quantitative Evaluation of Scintillation Camera Imaging Characteristics of Isotopes Used in Liver Radioembolization. *PLoS ONE.* 2011;6:e26174.
- 13 Hutton BF, Buvat I, Beekman FJ. Review and current status of SPECT scatter correction. *Phys Med Biol.* 2011;56:R85-R112.
- 14 Xiao JB, de Wit TC, Staelens SG, Beekman FJ. Evaluation of 3D Monte Carlo-based scatter correction for Tc-99m cardiac perfusion SPECT. *J Nucl Med.* 2006;47:1662-1669.
- 15 Xiao JB, de Wit TC, Zbijewski W, Staelens SG, Beekman FJ. Evaluation of 3D Monte Carlo-based scatter correction for Tl-201 cardiac perfusion SPECT. *J Nucl Med.* 2007;48:637-644.
- 16 Smits MLJ, Nijsen JFW, van den Bosch MAAJ et al. Holmium-166 radioembolization for the treatment of patients with liver metastases: design of the phase I HEPAR trial. *J Exp Clin Cancer Res.* 2010;29.
- 17 Smits MLJ, Nijsen JFW, van den Bosch MAAJ et al. Holmium-166 radioembolisation in patients with unresectable, chemorefractory liver metastases (HEPAR trial): a phase 1, dose-escalation study. *Lancet Oncol.* 2012;13:1025-1034.

- 18 Beekman FJ, de Jong HW, van GS. Efficient fully 3-D iterative SPECT reconstruction with Monte Carlo-based scatter compensation. *IEEE Trans Med Imaging*. 2002;21:867-877.
- 19 De Jong HWAM, Slijpen ETP, Beekman FJ. Acceleration of Monte Carlo SPECT simulation using convolution-based forced detection. *IEEE Trans Nucl Sci*. 2001;48:58-64.
- 20 Hendricks JS, McKinney GW, Waters LS et al. MCNPX Extensions, Version 2.5.0. 2005. Los Alamos, CA, Los Alamos National Laboratory Report LA-UR-05-2675.
- 21 De Jong HWAM, Wang WT, Frey EC, Vieregger MA, Beekman FJ. Efficient simulation of SPECT down-scatter including photon interactions with crystal and lead. *Med Phys*. 2002;29:550-560.
- 22 Kamphuis C, Beekman FJ, van Rijk PP, Vieregger MA. Dual matrix ordered subsets reconstruction for accelerated 3D scatter compensation in single-photon emission tomography. *Eur J Nucl Med*. 1998;25:8-18.
- 23 Bolch WE, Bouchet LG, Robertson JS et al. MIRD pamphlet No. 17: the dosimetry of nonuniform activity distributions--radionuclide S values at the voxel level. Medical Internal Radiation Dose Committee. *J Nucl Med*. 1999;40:115-365.
- 24 Bol GH, Kotte ANTJ, van der Heide UA, Legendijk JJW. Simultaneous multi-modality ROI delineation in clinical practice. *Comput Methods Programs Biomed*. 2009;96:133-140.
- 25 Wahl RL, Jacene H, Kasamon Y, Lodge MA. From RECIST to PERCIST: Evolving Considerations for PET Response Criteria in Solid Tumors. *J Nucl Med*. 2009;50:1225-1505.
- 26 Boellaard R, van Lingen A, Lammertsma AA. Experimental and clinical evaluation of iterative reconstruction (OSEM) in dynamic PET: Quantitative characteristics and effects on kinetic modeling. *J Nucl Med*. 2001;42:808-817.
- 27 Erlandsson K, Visvikis D, Waddington WA, Cullum I, Jarritt PH, Polowsky LS. Low-statistics reconstruction with AB-EMML. Conf Record of IEEE Nuclear Science Symp and Medical Imaging Conf. 2000;2:15/249-15/253.
- 28 Kennedy AS, Nag S, Salem R et al. Recommendations for radioembolization of hepatic malignancies using yttrium-90 microsphere brachytherapy: A consensus panel report from the Radioembolization Brachytherapy Oncology Consortium. *Int J Radiat Oncol Biol Phys*. 2007;68:13-23.
- 29 Chiesa C, Maccauro M, Romito R et al. Need, feasibility and convenience of dosimetric treatment planning in liver selective internal radiation therapy with Y-90 microspheres: the experience of the National Cancer Institute of Milan. *Q J Nucl Med Mol Imaging*. 2011;55:168-197.
- 30 Garin E, Lenoir L, Rolland Y et al. Dosimetry Based on Tc-99m-Macroaggregated Albumin SPECT/CT Accurately Predicts Tumor Response and Survival in Hepatocellular Carcinoma Patients Treated with Y-90-Loaded Glass Microspheres: Preliminary Results. *J Nucl Med*. 2012;53:255-263.
- 31 Kao YH, Tan AEH, Burgmans MC et al. Image-Guided Personalized Predictive Dosimetry by Artery-Specific SPECT/CT Partition Modeling for Safe and Effective Y-90 Radioembolization. *J Nucl Med*. 2012;53:559-566.
- 32 Van de Wiele C, Maes A, Brugman E et al. SIRT of liver metastases: physiological and pathophysiological considerations. *Eur J Nucl Med Mol Imaging*. 2012;39:1646-1655.
- 33 de Wit TC, Xiao JB, Beekman FJ. Monte Carlo-based statistical SPECT reconstruction: Influence of number of photon tracks. *IEEE Trans Nucl Sci*. 2005;52:1365-1369.

Chapter 6

**Tc-99m-MAA overestimates the dose to the lungs in
radioembolization: a quantitative evaluation in patients
treated with Ho-166 microspheres**



Submitted for publication as:

M. Elschot, M.G.E.H. Lam, J.F.W. Nijssen, M.L.J. Smits, J.F. Prince, M.A. Viergever, M.A.A.J. van den Bosch, B.A. Zonnenberg, H.W.A.M. de Jong.

Tc-99m-MAA overestimates the dose to the lungs in radioembolization: a quantitative evaluation in patients treated with Ho-166 microspheres.

Abstract

Objectives

Radiation pneumonitis is a rare but serious complication of radioembolization (RE). The particles used in holmium-166 microsphere ($^{166}\text{Ho-MS}$) RE can be visualized with a gamma camera, which facilitates image-based assessment of the mean dose to the lungs (LMD) after treatment (LMD_{Ho}). Prior to treatment, the LMD can be estimated on a $^{99\text{m}}\text{Tc-MAA}$ scout dose (eLMD_{Tc}), or on a $^{166}\text{Ho-MS}$ scout dose (eLMD_{Ho}). Assessment of LMD_{Ho} , eLMD_{Tc} , and eLMD_{Ho} can be performed on (planar) scintigraphic and SPECT images. We aim to quantitatively evaluate the performance of the $^{99\text{m}}\text{Tc-MAA}$ and $^{166}\text{Ho-MS}$ scout dose for estimation of the LMD in $^{166}\text{Ho-MS}$ RE.

Methods

First, the accuracy of scintigraphy-based and SPECT-based LMD_{Ho} values was evaluated in an anthropomorphic torso phantom with simulated lung shunt fractions (LSF) of 0 – 30%. Second, scintigraphy-based and SPECT-based eLMD_{Tc} and eLMD_{Ho} were compared to SPECT-based LMD_{Ho} in patients treated with $^{166}\text{Ho-MS}$ RE.

Results

In the phantom study, absolute errors on scintigraphy-based LMD_{Ho} ranged from 9.5 Gy (LSF = 30%) to 11.8 Gy (LSF = 10%). SPECT-based LMD_{Ho} values were more accurate, with errors ranging from 0.1 Gy (LSF = 0%) to -4.4 Gy (LSF = 30%). In the patient study, the median value of SPECT-based LMD_{Ho} was 0 Gy (0 – 0.7 Gy). SPECT-based eLMD_{Ho} was a significantly better predictor of LMD_{Ho} than scintigraphy-based eLMD_{Tc} ($p < 0.001$), SPECT-based eLMD_{Tc} ($p = 0.003$), and scintigraphy-based eLMD_{Ho} ($p < 0.001$).

Conclusions

$^{166}\text{Ho-MS}$ enable accurate assessment of the LMD with quantitative SPECT. In clinical practice, LMD values are significantly overestimated on scintigraphic and SPECT images of a $^{99\text{m}}\text{Tc-MAA}$ scout dose, but not on SPECT images of a $^{166}\text{Ho-MS}$ scout dose. These findings suggest that treatment planning in RE is improved if the same MS are used for scout dose and treatment.

6.1 Introduction

Intra-arterial radioembolization (RE) with yttrium-90 (^{90}Y) labeled microspheres (MS) is used for treatment of unresectable liver malignancies (1,2). Treatment complications are mild in the majority of patients and may include fatigue, nausea, vomiting, and/or mild pain (1,3,4). However, more serious complications have also been reported, such as radioembolization-induced liver disease (REILD) (5-7), gastrointestinal ulceration and bleeding (3,8,9), and radiation pneumonitis (10-12). Radiation pneumonitis is considered one of the most serious complications of RE, since it may cause serious debilitation of respiratory function and can even be fatal (10,13). It is generally assumed that, to avoid radiation pneumonitis, the mean radiation absorbed dose to the lungs (LMD) should not exceed 30 Gy for a single treatment and 50 Gy for multiple treatments. These limits have been adopted from the field of external beam radiotherapy and adapted to ^{90}Y RE (10,14,15).

In the currently used lung dosimetry model for ^{90}Y -MS, a scout dose of technetium-99m macroaggregated albumin ($^{99\text{m}}\text{Tc}$ -MAA) particles is used to estimate the LMD. This is performed by measurement of the fraction of particles that shunted to the lungs (LSF) on (planar) scintigraphic images (16,17). However, a study by Salem et al. has demonstrated that this model is not predictive for radiation pneumonitis in patients treated with ^{90}Y glass MS (18). Possible explanations for the poor performance of the lung dosimetry model include i) inaccurate quantification of the $^{99\text{m}}\text{Tc}$ -MAA activity in the lungs, ii) invalid model assumptions with regard to the homogeneity of the lung dose distribution, and iii) disparity between the $^{99\text{m}}\text{Tc}$ -MAA distribution and that of the ^{90}Y -MS. In a recent clinical study, Yu et al. suggested that substantial improvements to the estimated LMD (eLMD) can be realized by using scatter and attenuation corrected SPECT/CT images of the $^{99\text{m}}\text{Tc}$ -MAA distribution, instead of scintigraphic images (19). To evaluate the accuracy of the scintigraphy-based and SPECT-based eLMD values, the LMD would ideally have been measured after ^{90}Y -MS treatment. Unfortunately, current clinical ^{90}Y Bremsstrahlung SPECT is hindered by poor image quality, whereas ^{90}Y PET is extremely challenging in the lung region due to the low activity concentration (20). Therefore, the predictive value of the eLMD remains unclear to date.

In our institute, Poly(L-lactic acid) MS loaded with the high-energy beta emitter holmium-166 (^{166}Ho) have been developed as an alternative to ^{90}Y -MS (21). ^{166}Ho -MS possess favorable nuclear imaging characteristics, as ^{166}Ho beta-decay is accompanied by the emission of 81 keV gamma photons (22). Recently, we have demonstrated

that quantitative SPECT imaging of the ^{166}Ho activity distribution is feasible in clinical practice, despite the relatively high susceptibility of the 81 keV photons to scatter and attenuation and the deteriorating effects of high energy Bremsstrahlung and gamma photons (*chapter 5*). Of interest, quantitative ^{166}Ho SPECT may facilitate the use of a scout dose of ^{166}Ho -MS to predict the distribution of the treatment dose, instead of a scout dose of $^{99\text{m}}\text{Tc}$ -MAA particles. To investigate this, the ^{166}Ho -MS RE clinical study protocols include both a $^{99\text{m}}\text{Tc}$ -MAA scout dose and a ^{166}Ho -MS scout dose.

Radiation pneumonitis is also considered a risk factor for ^{166}Ho -MS RE, since the diameter of the ^{166}Ho -MS (mean 30 μm ; range 20 – 50 μm) (23) is similar to that of ^{90}Y glass MS (mean 25 μm ; range 20 - 30 μm) and resin MS (mean 32 μm ; range 20 - 60 μm) (24). As currently implemented, ^{166}Ho -MS RE enables image-based assessment of the LMD after treatment (LMD_{Ho}), estimation of the LMD on the $^{99\text{m}}\text{Tc}$ -MAA scout dose (eLMD_{Tc}), and estimation of the LMD on the ^{166}Ho -MS scout dose (eLMD_{Ho}). The main objective of this study is to compare the performance of the $^{99\text{m}}\text{Tc}$ -MAA and ^{166}Ho -MS scout dose for estimation of the LMD in ^{166}Ho -MS RE. For this purpose, the accuracy of scintigraphy-based and SPECT-based assessment of LMD_{Ho} was first evaluated in a phantom study. Second, the scintigraphy-based and SPECT-based eLMD_{Tc} and eLMD_{Ho} were compared to LMD_{Ho} in patients treated with ^{166}Ho -MS RE. This study is the first to quantify the LMD in patients treated with RE by post-treatment assessment of the MS concentration in the lungs.

6.2 Materials and methods

All scintigraphic and SPECT/CT images were acquired with a Siemens Symbia T16 SPECT/CT system (Siemens Healthcare, Erlangen, Germany), which combines a dual detector SPECT scanner with a 16-slice CT scanner. The medium-energy low-penetration (MELP) collimators were mounted for ^{166}Ho imaging and the low-energy high-resolution (LEHR) collimators for $^{99\text{m}}\text{Tc}$ imaging.

6.2.1 Phantom study

The accuracy of scintigraphy-based and SPECT-based assessment of LMD_{Ho} for several different LSF values was evaluated with phantom experiments and simulations.

Phantom

The liver compartment (volume = 1200 ml; $\rho = 1 \text{ g ml}^{-1}$) of an anthropomorphic torso phantom was uniformly filled with ^{166}Ho . The phantom further contained a cylindrical

spine, a fillable heart compartment and two lung compartments (left, volume = 900 ml; right, volume = 1100 ml; $\rho = 0.4 \text{ g ml}^{-1}$). At time of imaging, the total ^{166}Ho activity in the liver compartment was 368.9 Mbq. Since no activity was applied to the lung compartments, this phantom set-up simulated a clinical situation without lung shunting (LSF = 0%).

Scintigraphy

Projection images of the phantom were acquired on a 256 x 256 matrix (zoom = 1.0; pixelsize = 2.4 x 2.4 mm²) in 300 seconds with the camera heads in anterior and posterior position. In addition to the 81 keV +/- 7.5% photopeak window, a 118 keV +/- 6% window was defined to correct for down-scattered high-energy contributions to the photopeak window. Geometric mean (GM) images were calculated as the geometric mean of the down-scatter corrected anterior and posterior projections, using

$$GM = \sqrt{(ANT^{81} - g \times ANT^{118}) \times (POST^{81} - g \times POST^{118})} \quad (6.1)$$

with ANT^{81} , $POST^{81}$, ANT^{118} , and $POST^{118}$ the anterior and posterior photopeak and down-scatter projections, respectively, and $g = (0.15 \times 81) / (0.12 \times 118)$ a factor to compensate for the difference in energy window widths.

SPECT/CT

SPECT data of the phantom were acquired on a 128 x 128 matrix (zoom = 1.0; pixelsize = 4.8 x 4.8 mm²) using 120 angles (30 seconds per projection) over a non-circular 360° orbit and a 81 keV +/- 7.5% keV photopeak window. Low-dose CT data (130 kVp; 30 mAs; adaptive dose modulation) were acquired and reconstructed to a voxelsize of 1.27 x 1.27 x 5 mm³ using a smooth kernel (B08s; Siemens Healthcare). After a CT-derived attenuation map was created (Syngo MI Applications; Siemens Healthcare), SPECT images were offline reconstructed to a voxelsize of 4.8 x 4.8 x 4.8 mm³ using an in-house developed quantitative reconstruction algorithm (20 iterations, 8 subsets, no post-reconstruction filtering), which includes full Monte Carlo-based compensation for scatter and attenuation effects and distance- and energy-dependent modeling of the collimator-detector response (*chapter 5*). Reconstructed counts were converted into units of activity by multiplication with a pre-determined calibration factor.

Simulations

Three-dimensional (3D) digital activity distributions were generated to simulate the phantom set-up with seven different LSF values in the range of 0–30%. First, the liver and lung compartments of the phantom were segmented on CT using the in-house developed radiotherapy-planning software package Volumetool (25). Subsequently, activity concentrations (i.e., voxel intensities) were proportionally imposed to the liver and lung voxels, such that 0, 1, 2, 5, 10, 20, and 30% of the total activity was located in the lung compartments. Together with the CT-derived attenuation map, these 3D activity distributions were input to an in-house developed computationally efficient Monte Carlo simulator to generate nearly noise-free projections including scatter, attenuation and collimator-detector effects (*chapter 5*). The number of counts in the simulated scintigraphy and SPECT projections were scaled to the total number of counts in the measured projections (LSF = 0%) and Poisson noise was voxelwise added. Finally, GM and SPECT images were reconstructed from the simulated projections as described for the phantom measurements. To evaluate the simulation set-up, simulated projections (LSF = 0%) were compared to the measured projections.

Region-of-interest delineation

For analysis of the SPECT images, 3D regions-of-interest (ROIs) were delineated on the CT-scan of the phantom using VolumeTool. Whole body (ROI_{3D-WB}), right lung (ROI_{3D-RL}), and left lung ROI (ROI_{3D-LL}) delineation was performed semi-automatically (25) and the liver ROI (ROI_{3D-LIV}) was manually delineated. A liver+2cm ROI ($ROI_{3D-LIV2CM}$) was generated by automatically adding a 2 cm margin to ROI_{3D-LIV} . A total lung ROI ($ROI_{3D-LUNG}$) was created consisting of all voxels in ROI_{3D-RL} and ROI_{3D-LL} that did not overlap with $ROI_{3D-LIV2CM}$.

$$ROI_{3D-LUNG} = (ROI_{3D-RL} \cup ROI_{3D-LL}) \setminus ROI_{3D-LIV2CM} \quad (6.2)$$

The voxels in $ROI_{3D-LIV2CM}$ were excluded from $ROI_{3D-LUNG}$ to prevent erroneous registration of liver activity to the lung region, which may occur due to partial volume effects, patient breathing, and/or suboptimal SPECT/CT registration (19). Clearly, these effects will be less a problem in the phantom study, but we chose to analyze the phantom data in the same manner as the clinical data. For analysis of the GM images, two-dimensional (2D) right lung (ROI_{2D-RL}), left lung (ROI_{2D-LL}), and liver+2cm ($ROI_{2D-LIV2CM}$) ROIs were calculated from their 3D equivalents as the binary projections

in the anterior/posterior direction. A total lung ROI ($ROI_{2D-LUNG}$) was subsequently created consisting of all pixels in ROI_{2D-RL} and ROI_{2D-LL} that did not overlap with $ROI_{2D-LIV2CM}$

$$ROI_{2D-LUNG} = (ROI_{2D-RL} \cup ROI_{2D-LL}) \setminus ROI_{2D-LIV2CM} \quad (6.3)$$

6.2.2 Clinical study

Patients

Images of the scout and treatment dose distribution were processed to evaluate the (estimated) mean lung doses (viz. $eLMD_{Tc}$, $eLMD_{Ho}$, and LMD_{Ho}) in 14 patients with unresectable, chemorefractory liver metastases. Six patients were treated with ^{166}Ho -MS RE as part of a phase I dose-escalation study (HEPAR; registered with Clinicaltrials.gov, number NCT01031784), and eight patients as part of an ongoing phase II efficacy study (HEPAR II; Clinicaltrials.gov, number NCT01612325). SPECT/CT data of the first 9 (out of 15) patients of the phase I study were not available, because these patients were scanned on a (non-hybrid) SPECT system. Both studies were approved by the institutional review board and all patients provided written informed consent before enrolment. Baseline patient and treatment characteristics are provided in Table 6.1. Study design and clinical results (patient characteristics, toxicity and adverse events) of the phase I study have been described previously (21,26).

Radioembolization procedure

The ^{166}Ho -MS RE procedure included a standard work-up angiography for prophylactic coil-embolization of non-target vessels, followed by administration of approximately 150 MBq of ^{99m}Tc -MAA particles (0.8 mg, TechneScan LyoMaa, Mallinckrodt Medical B.V., Petten, the Netherlands) through a microcatheter in the proper, left or right hepatic artery (21,27). The ^{99m}Tc -MAA distribution was evaluated with scintigraphy and SPECT/CT. If there was no extrahepatic activity, except for a LSF of maximally 20%, the patients were scheduled for treatment. The required ^{166}Ho activity (A) was calculated using

$$A(GBq) = \frac{D(Gy)}{15.87(JGBq^{-1})} \times m_{LIVER}(kg) \quad (6.4)$$

with D the aimed liver absorbed dose (60 – 80 Gy), m_{LIVER} the liver mass derived from contrast-enhanced CT and 15.87 the total energy released per unit of activity

^{166}Ho . On the day of treatment, a microcatheter was placed under angiography in the same position as used for $^{99\text{m}}\text{Tc}$ -MAA administration and a ^{166}Ho -MS scout dose of approximately 250 MBq (60 mg) was administered to the patient, followed by evaluation of the ^{166}Ho -MS distribution with scintigraphy and SPECT/CT. In the absence of extrahepatic activity, the treatment dose of ^{166}Ho -MS (approximately 540 mg) was administered under angiography with the microcatheter again in the same position. Post-treatment scintigraphy and SPECT/CT were performed five to seven days after administration of the ^{166}Ho treatment dose.

Table 6.1. Patient baseline characteristics and treatment details. Data are number or median (range).

Baseline characteristics	<i>n</i>
Nr. of patients that underwent ^{166}Ho -MS RE	14
Gender	
male	9
female	5
Age (y)	65 (45 – 87)
Tumor type (primary)	
Uveal melanoma	2
Colorectal carcinoma	10
Pancreatic cancer	1
Neuroendocrine cancer	1
Aimed liver absorbed dose	
60 Gy	11
80 Gy	3
Treatment details	
Liver lobes	
Bilobar	13 ^a
Right lobar	1
Treated liver volume (ml)	1750 (958 – 3129)
Net administered activity (MBq)	
$^{99\text{m}}\text{Tc}$ -MAA scout dose	139 (105 – 180)
^{166}Ho -MS scout dose	265 (229 – 297)
^{166}Ho -MS treatment dose	6701 (3822 – 11093)
Total activity at time of nuclear imaging (MBq)	
$^{99\text{m}}\text{Tc}$ -MAA scout dose	127 (91 – 146)
^{166}Ho -MS scout dose	256 (222 – 288)
^{166}Ho -MS treatment dose	353 (175 – 438)

^a One patient received left and right lobar treatment in two separate sessions.

^{99m}Tc-MAA imaging

^{99m}Tc-MAA projection images of the abdomen and the thorax were acquired on a 256 x 256 matrix (zoom = 1.0; pixelsize = 2.4 x 2.4 mm²) in 300 seconds with the camera heads in anterior and posterior position. The photopeak window was set to 140 keV +/- 7.5%. GM images were calculated as the geometric mean of the anterior and posterior projections, using

$$PS = \sqrt{ANT^{140} \times POST^{140}} \quad (6.5)$$

with ANT¹⁴⁰ and POST¹⁴⁰ the anterior and posterior photopeak projections, respectively. An anterior thorax projection of a cobalt-57 (⁵⁷Co) flood-source placed behind the patient was acquired to support delineation of the lung ROIs.

^{99m}Tc-MAA SPECT data of the abdomen were acquired on a 128 x 128 matrix (zoom = 1.23; pixelsize = 3.9 x 3.9 mm²) using 120 angles (20 seconds per projection) over a non-circular 360° orbit. In addition to the 140 keV +/- 7.5% photopeak energy window, a 119 keV +/- 8.8% window was defined for scatter correction. Low-dose CT data were acquired and reconstructed as described for ¹⁶⁶Ho SPECT/CT in the phantom section. SPECT images were reconstructed to a voxelsize of 3.9 x 3.9 x 3.9 mm³ using Siemens FLASH3D (8 iterations, 4 subsets, no post-reconstruction filter) including correction for scatter and attenuation. These reconstruction settings are known to result in quantitatively accurate SPECT images (28). Reconstructed counts were converted into units of activity by multiplication with a pre-determined calibration factor.

¹⁶⁶Ho-MS imaging

For both the ¹⁶⁶Ho-MS scout and treatment dose, scintigraphic images of the abdomen and thorax were acquired and processed as described in the phantom section. Additionally, an anterior ⁵⁷Co flood-source projection of the thorax region was acquired to support delineation of the lung ROIs. SPECT/CT imaging of the abdomen was performed as described in the phantom section.

Region-of-interest delineation

Three-dimensional ROIs were delineated on the abdominal CT-scans corresponding to the SPECT images of the ^{99m}Tc-MAA scout dose, ¹⁶⁶Ho-MS scout dose, and ¹⁶⁶Ho-MS treatment dose. For each of the three scans, ROI_{3D-WB}, ROI_{3D-RL}, ROI_{3D-LL}, ROI_{3D-LIV}, ROI_{3D-LIV2CM} and ROI_{3D-LUNG} were created as described in the phantom section.

ROI_{3D-LUNG} extended from the lung bases to the end of the field-of-view (FOV) of the SPECT/CT scan, which did not always cover the complete lung region in clinical practice. For analysis of the abdominal GM images, ROI_{2D-LIV2CM} was calculated from the 3D ROIs as described in the phantom section. For the analysis of the thoracic GM images, however, ROI_{2D-LUNG} could not be automatically calculated from the 3D ROIs, since the SPECT/CT FOV did not cover the complete lung region in all patients. Therefore, ROI_{2D-RL} and ROI_{2D-LL} were manually delineated on the thoracic GM images, supported by the ⁵⁷Co flood-source projections. Subsequently, ROI_{2D-LIV2CM} was registered to the thoracic GM image and ROI_{2D-LUNG} was calculated according to equation 6.3.

6.2.3 Lung dosimetry

The ^{99m}Tc-MAA and ¹⁶⁶Ho-MS scout dose images were used to estimate the LMD induced by the treatment dose of ¹⁶⁶Ho-MS. Scintigraphy-based eLMD_{Tc} and eLMD_{Ho} values were calculated as

$$eLMD_{Tc/Ho} (Gy) = \frac{C_{2D-LUNG}}{C_{2D-LIV2CM} + C_{2D-LUNG}} \times \frac{A_0 (GBq) \times 15.87 (J GBq^{-1})}{m_{2D-LUNG} (kg)} \quad (6.6)$$

with $C_{2D-LUNG}$ the cumulative counts in ROI_{2D-LUNG}, $C_{2D-LIV2CM}$ the cumulative counts in ROI_{2D-LIV2CM}, A_0 the net ¹⁶⁶Ho activity at time of administration of the treatment dose, and $m_{2D-LUNG}$ the lung mass, which was assumed to be 1 kg for all patients (29). For the phantom, $m_{2D-LUNG}$ was 0.6 kg.

SPECT-based eLMD_{Tc} and eLMD_{Ho} values were calculated as

$$eLMD_{Tc/Ho} (Gy) = \frac{A_{3D-LUNG} (GBq)}{A_{REF} (GBq)} \times \frac{A_0 (GBq) \times 15.87 (J GBq^{-1})}{m_{3D-LUNG} (kg)} \quad (6.7)$$

with $A_{3D-LUNG}$ the cumulative activity in ROI_{3D-LUNG}, A_{REF} the reference activity, and $m_{3D-LUNG}$ the mass of ROI_{3D-LUNG}, calculated as the ROI volume times the lung density of 0.3 g ml⁻¹ (30). For the SPECT images of the ¹⁶⁶Ho-MS scout dose, A_{REF} was set to the net activity of the ¹⁶⁶Ho-MS scout dose at time of scanning. For the ^{99m}Tc-MAA scout dose, A_{REF} was set to the total recovered activity in ROI_{3D-WB} instead of the injected activity, since dissociated ^{99m}Tc-pertechnetate had potentially accumulated in the brain, thyroid, salivary glands, kidneys and bladder (31), all of which were typically located outside the SPECT FOV.

The LMD_{Ho} values, which were treated as the golden standard in this clinical study, were calculated on SPECT images of the ^{166}Ho -MS treatment dose, using

$$LMD_{Ho} (Gy) = \frac{A_{3D-LUNG} (GBq)}{A_{REF} (GBq)} \times \frac{A_0 (GBq) \times 15.87 (J GBq^{-1})}{m_{3D-LUNG} (kg)} \quad (6.8)$$

With A_{REF} the net activity of the ^{166}Ho -MS treatment dose at time of scanning.

6.2.4 Statistical analysis

Descriptive parameters are presented as median and range. Statistical differences between eLMD and LMD values were analyzed using the non-parametric Wilcoxon signed rank test for paired-data (significance level of 0.05), since normality could not be assumed with the small sample sizes.

6.3 Results

6.3.2 Phantom study

Excellent agreement between the simulations and measurements of anterior (Figure 6.1 A) and posterior (Figure 6.1 B) projections of the phantom (LSF = 0%) was observed in both the 81 keV photopeak window and the 118 keV down-scatter window, which validated our simulation set-up. The total activity in the phantom was 368.9 MBq. The total activity in ROI_{3D-WB} as recovered with quantitative SPECT was 372.4 MBq (relative error: 0.9%) for the measurement (LSF = 0%). For the simulations, the SPECT recovered activities in ROI_{3D-WB} ranged from 364.3 MBq to 365.8 MBq (-1.3% – -0.8%).

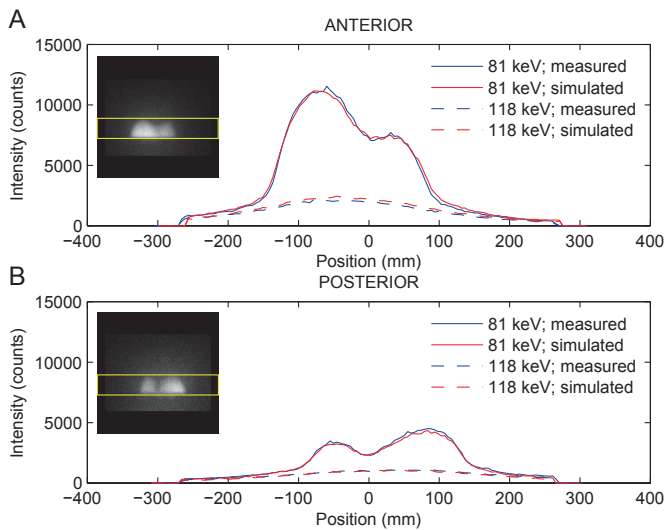


Figure 6.1. The summed image intensities (counts) over 10-cm-wide profiles through the measured and simulated anterior (A) and posterior (B) projections of the phantom without lung shunting.

Figure 6.2 shows the GM and SPECT images of the simulated phantom with a 20% LSF. For the phantom without lung shunting, scintigraphy substantially overestimated the true LMD of 0 Gy in both the measurement ($\text{LMD}_{\text{Ho}} = 9.5 \text{ Gy}$) and the simulation ($\text{LMD}_{\text{Ho}} = 11.2 \text{ Gy}$) (Figure 6.3 A). SPECT-based LMD_{Ho} values of the phantom with 0% LSF were in good agreement with the true LMD: 0 Gy and 0.1 Gy for the measurement and simulation, respectively (Figure 6.3 A). For all simulated LSF values, the SPECT-based LMD_{Ho} was closer to the true LMD than the scintigraphy-based LMD_{Ho} (Figure 6.3 A). Absolute errors on the scintigraphy-based and SPECT-based LMD_{Ho} ranged from 9.5 Gy to 11.8 Gy, and from 0.1 Gy to -4.4 Gy, respectively (Figure 6.3 B). Relative errors ranged from 23.2% to 844.5% for scintigraphy-based LMD_{Ho} and from -10.9% to -46.3% for SPECT-based LMD_{Ho} (Figure 6.3 B).

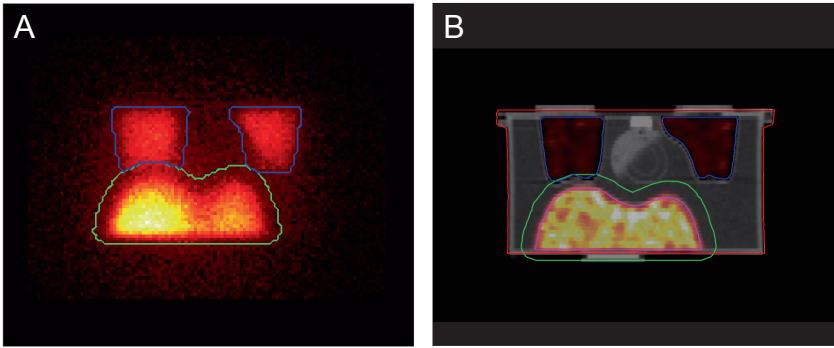


Figure 6.2. The simulated GM image of the phantom with 20% LSF (A) and a coronal slice through the corresponding SPECT image, fused with CT (B). The images are overlaid with the boundaries of ROI_{2D-LIV2CM} (A; green), ROI_{2D-LUNG} (A; blue), ROI_{3D-LIV2CM} (B; green), ROI_{3D-RL} and ROI_{3D-LL} (B; blue), ROI_{3D-LIV} (B; pink) and ROI_{3D-WB} (B; red).

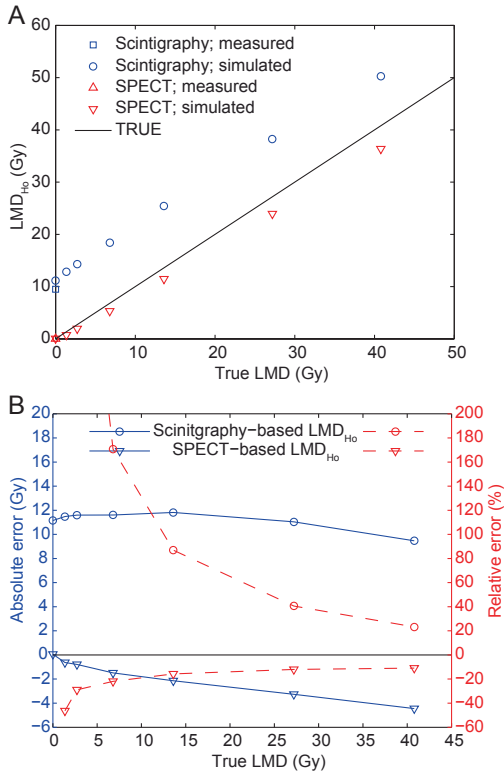


Figure 6.3. In (A) image-based LMD_{Ho} values (Gy) are plotted as function of the true LMD (Gy). Data points represent the measured and simulated scintigraphy-based and SPECT-based LMD_{Ho} values (Gy). In (B) the absolute (Gy) and relative errors (%) of the simulated scintigraphy-based and SPECT-based LMD_{Ho} are plotted as function of the true LMD (Gy).

6.3.2 Clinical study

The superiority of SPECT-based LMD_{Ho} to scintigraphy-based LMD_{Ho} was demonstrated in the phantom study. Consequently, SPECT-based LMD_{Ho} were treated as the golden standard in this clinical study. The median relative error on the total SPECT-based recovered activities in the patients' whole body ROIs was -7.5% (range = -35.6 – 8.2%) for the ^{99m}Tc -MAA scout dose, 4.7% (range = -2.4 – 8.3%) for the ^{166}Ho -MS scout dose, and 4.5% (range = -5.9 – 9.8%) for the ^{166}Ho -MS treatment dose. The LMD_{Ho} , $eLMD_{Tc}$, and $eLMD_{Ho}$ values of all 14 patients are plotted in Figure 6.4.

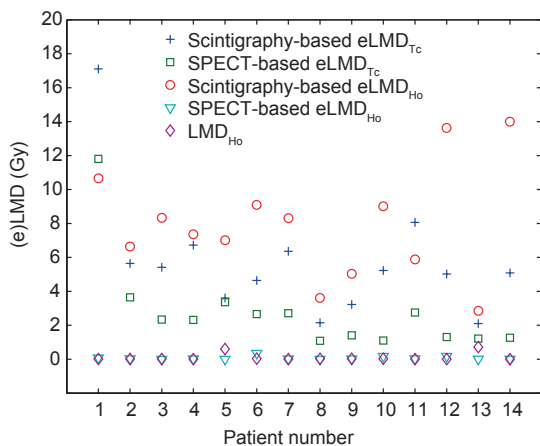


Figure 6.4. A plot of LMD_{Ho} , $eLMD_{Tc}$, and $eLMD_{Ho}$ values (Gy) for each patient.

For patient 12, who received left and right lobar treatment in two tempi, the values represent the cumulative (estimated) dose. Over all patients, LMD_{Ho} ranged from 0 Gy to 0.7 Gy, with a median value of 0 Gy. LMD_{Ho} was significantly overestimated by scintigraphy-based $eLMD_{Tc}$, SPECT-based $eLMD_{Tc}$, and scintigraphy-based $eLMD_{Ho}$ (Table 6.2). On the contrary, no significant differences were found between LMD_{Ho} and SPECT-based $eLMD_{Ho}$.

Table 6.2. Analyses of statistical differences between LMD and eLMD values.

Method 1	Method 2	Median difference (range)	p-value
LMD_{Ho}	Scintigraphy-based $eLMD_{Tc}$	5.1 Gy (1.4 – 17.1)	< 0.001
LMD_{Ho}	SPECT-based $eLMD_{Tc}$	2.3 Gy (0.5 – 11.8)	< 0.001
LMD_{Ho}	Scintigraphy-based $eLMD_{Ho}$	7.8 Gy (2.2 – 14.0)	< 0.001
LMD_{Ho}	SPECT-based $eLMD_{Ho}$	0.0 Gy (-0.7 – 0.3)	0.542

These findings are endorsed by the GM and SPECT images of patient 1, which are shown in Figure 6.5. The absolute differences between LMD_{Ho} and $eLMD_{Tc}$ ($\Delta eLMD_{Tc}$), and LMD_{Ho} and $eLMD_{Ho}$ ($\Delta eLMD_{Ho}$), can be regarded as a measure of goodness of predictability (Figure 6.6). It was found that SPECT-based $eLMD_{Ho}$ was a significantly better predictor for LMD_{Ho} than all other methods (Table 6.3).

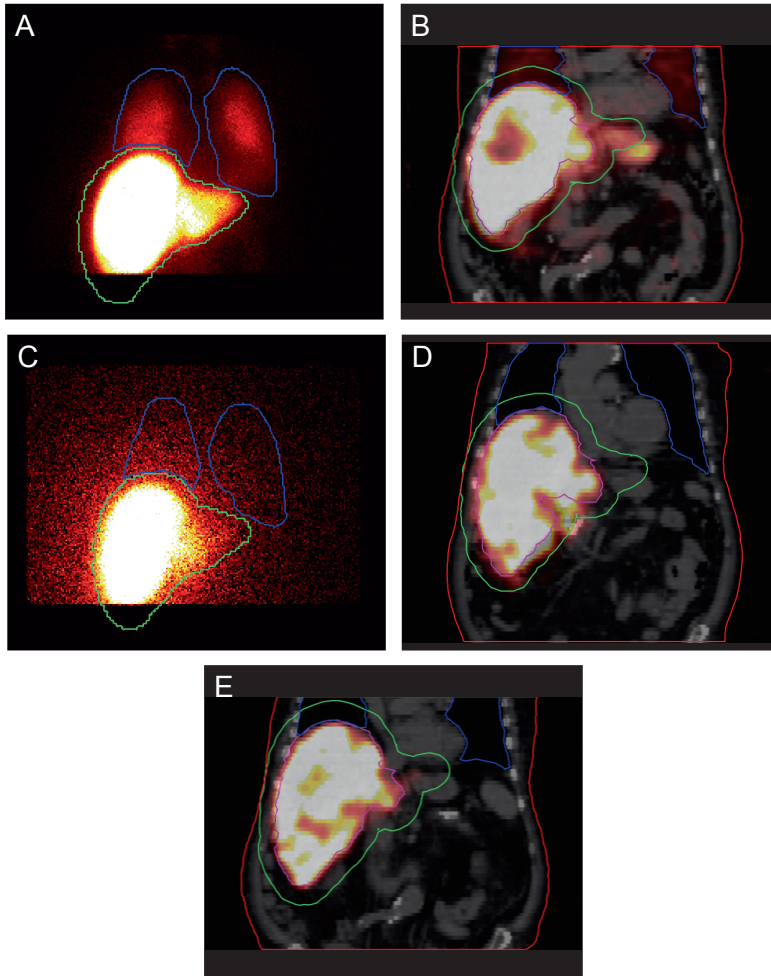


Figure 6.5. Scintigraphic and SPECT images of patient 1. The GM image of the ^{99m}Tc -MAA scout dose (A), a coronal slice through the SPECT image of the ^{99m}Tc -MAA scout dose (B), the GM image of the ^{166}Ho -MS scout dose (C), a coronal slice through the SPECT image of ^{166}Ho -MS scout dose (D), and a coronal slice through the SPECT image of the ^{166}Ho -MS treatment dose (E). GM images are overlaid with the boundaries of $\text{ROI}_{2\text{D-LIV}2\text{CM}}$ (A,C; green) and $\text{ROI}_{2\text{D-LUNG}}$ (A,C; blue). SPECT images are fused with CT and overlaid with the boundaries of $\text{ROI}_{3\text{D-LIV}2\text{CM}}$ (B,D,E; green), $\text{ROI}_{3\text{D-RL}}$ and $\text{ROI}_{3\text{D-LL}}$ (B,D,E; blue), $\text{ROI}_{3\text{D-LIV}}$ (B,D,E; pink) and $\text{ROI}_{3\text{D-WB}}$ (B,D,E; red). A homogeneous distribution of ^{99m}Tc -MAA in the lung region is clearly observed in (B), whereas this is not the case for ^{166}Ho -MS in (D) and (E).

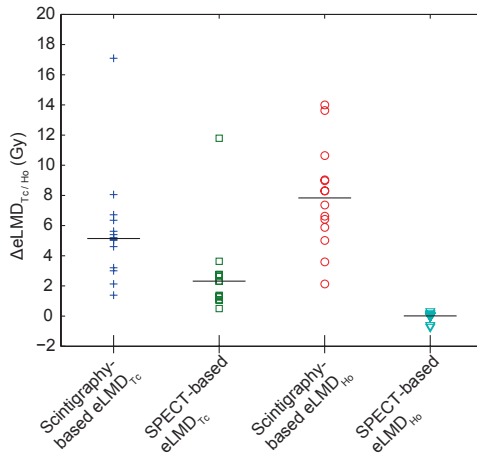


Figure 6.6. A plot of the absolute differences between image-based LMD_{Ho} and $eLMD_{Tc}$ ($\Delta eLMD_{Tc}$), and LMD_{Ho} and $eLMD_{Ho}$ ($\Delta eLMD_{Ho}$) values. The data points represent the $\Delta eLMD_{Tc/Ho}$ values for each patient and the black lines represent median values.

Table 6.3. Analyses of statistical differences between $\Delta eLMD$ values.

Method 1	Method 2	Median difference (range)	p-value
SPECT-based $\Delta eLMD_{Ho}$	Scintigraphy-based $\Delta eLMD_{Tc}$	5.1 Gy (2.1– 17.0)	< 0.001
SPECT-based $\Delta eLMD_{Ho}$	SPECT-based $\Delta eLMD_{Tc}$	2.3 Gy (0.9 – 11.7)	< 0.001
SPECT-based $\Delta eLMD_{Ho}$	Scintigraphy-based $\Delta eLMD_{Ho}$	7.8 Gy (2.8 – 14.0)	< 0.001
SPECT-based $\Delta eLMD_{Tc}$	Scintigraphy-based $\Delta eLMD_{Tc}$	3.4 Gy (0.2 – 5.3)	< 0.001
SPECT-based $\Delta eLMD_{Tc}$	Scintigraphy-based $\Delta eLMD_{Ho}$	4.3 Gy (-1.2 – 12.7)	< 0.001
Scintigraphy-based $\Delta eLMD_{Tc}$	Scintigraphy-based $\Delta eLMD_{Ho}$	1.9 Gy (-6.5 – 8.9)	0.035

6.4 Discussion

The objective of this study was to compare the performance of the ^{99m}Tc -MAA and ^{166}Ho -MS scout dose for estimation of the LMD in ^{166}Ho -MS RE. Using phantom experiments and simulations, we have demonstrated that image-based post-treatment assessment of LMD_{Ho} is most accurate with quantitative SPECT. For a clinically relevant LMD of 30 Gy, an underestimation of about 3.5 Gy (11.5%) is to be expected with SPECT, which is mainly due to partial volume effects. With scintigraphy, an overestimation of about 10.5 Gy (35%) is expected, due to lack of proper compensation methods for photon scatter and attenuation. Simulations were performed to analyze LSFs larger than 0%, whereas ideally measured projection images of a physical phantom would have been used (as was done for LSF = 0%). However, it is somewhat difficult to achieve a homogeneous activity distribution in the lung compartments of the anthropomorphic torso phantom, which contain thousands of small Styrofoam spheres. Additionally, the simulation approach

provides more flexibility with regard to the magnitude and number of LSF values tested. The comparison of the simulated and measured phantom set-up for LSF = 0% showed good agreement in intensity distributions, scintigraphy-based and SPECT-based LMD_{Ho} values, and the total recovered activities, which validated the simulation set-up.

This is the first study to have assessed the MS-induced LMD with quantitative SPECT in patients treated with RE. The maximum LMD_{Ho} value observed in the clinical study was only 0.7 Gy. Consistent with these very low LMD_{Ho} values, none of the patients included in this study showed clinical signs of radiation pneumonitis. Scintigraphy-based $eLMD_{Tc}$ values were significantly higher than LMD_{Ho} values, with observed differences up to 17.1 Gy. This indicates that for ^{166}Ho MS RE, the LMD is not accurately predicted by the currently advised lung dosimetry model based on ^{99m}Tc -MAA. The poor performance of the model can be partly attributed to the fact that the ^{99m}Tc -MAA GM images were not corrected for scatter and attenuation effects. This is supported by the SPECT-based $eLMD_{Tc}$ values presented in this study and in the study of Yu et al. (19), which were significantly lower than their scintigraphy-based equivalents. However, SPECT-based $eLMD_{Tc}$ also significantly overestimated LMD_{Ho} , despite proper compensation for scatter and attenuation effects. Importantly, visual comparison of the SPECT images of the ^{99m}Tc -MAA scout dose and the ^{166}Ho -MS treatment dose learned that these differences in (estimated) LMD were truly the result of disparity between the radioactive particle distributions.

Small ^{99m}Tc -MAA particles (< 20 μm) are abundantly present as a result of the broad range in size (10 – 90 μm) and the relative instability of ^{99m}Tc -MAA particles (32,33). Being relatively prone to arteriovenous shunting, these small particles are likely to be retained in the lung tissue, as a result of mechanical lodging in the pulmonary arterioles and capillaries or by uptake by the alveolar macrophages of the reticuloendothelial system (33,34). To the contrary, the ^{166}Ho MS are larger and highly stable (23), and may therefore be less prone to arteriovenous shunting. Therefore, we hypothesize that the presence of small ^{99m}Tc -MAA particles substantially contributes to the overestimation of the LMD. The glass and resin ^{90}Y -MS are comparable in size and stability to the ^{166}Ho -MS. Consequently, it is likely that disparity between the ^{99m}Tc -MAA distribution and the ^{90}Y -MS distribution is also present in selected patients treated with ^{90}Y -MS RE. This has possibly contributed to the poor performance of the lung dosimetry model for ^{90}Y -MS RE that was observed by Salem et al (18). These findings suggest that a number of patients scheduled for RE (both ^{90}Y -MS-RE and ^{166}Ho -MS-RE) are unnecessarily treated with a reduced amount of activity, or are withheld treatment overall, due to overestimation of the LSF with ^{99m}Tc -MAA.

In contrast to SPECT-based $eLMD_{Tc}$, SPECT-based $eLMD_{Ho}$ was able to accurately predict the LMD induced by the ^{166}Ho -MS treatment dose. This good agreement may be due to the fact that the same ^{166}Ho -MS are used for scout dose and treatment. SPECT-based estimation of the LMD does not require an additional scan, as it can be performed on the abdominal SPECT/CT scan of the ^{166}Ho -MS scout dose that is routinely acquired for assessment of possible extrahepatic ^{166}Ho -MS deposition. The value of the ^{166}Ho -MS scout dose needs to be further investigated in a patient study without eLMD-related exclusion criteria (i.e. LSF > 20% or LMD > 30 Gy on ^{99m}Tc -MAA). With such a study design, it can be investigated whether LMD estimation on the ^{166}Ho -MS scout dose will avoid unnecessary exclusion of patients (in comparison to ^{99m}Tc -MAA). Furthermore, the maximum tolerated dose to the lungs, which is currently assumed to be 30 Gy, can be validated or redefined by means of post-treatment assessment of the true LMD.

This study demonstrates that $eLMD_{Tc}$ values are a too conservative predictor of the LMD_{Ho} , not only because of the limited quantitative accuracy of scintigraphic images (19,35), but also due to disparity between the distribution of the ^{99m}Tc -MAA scout dose and that of the ^{166}Ho -MS treatment dose. The significantly better predictive value of the ^{166}Ho -MS scout dose suggests that treatment planning for ^{166}Ho -MS RE is improved by using the same microspheres for scout dose and treatment. However, before ^{166}Ho -MS can fully replace ^{99m}Tc -MAA as the particles to be used for treatment planning, the performance of a ^{166}Ho -MS scout dose in other established uses of ^{99m}Tc -MAA needs to be investigated as well, such as for prediction of extrahepatic deposition of activity in the gastro-intestinal tract (36), and for prediction of the intrahepatic distribution for partition modeling (37).

6.5 Conclusion

We have shown that ^{166}Ho -MS enable accurate assessment of the LMD on quantitative SPECT images. In patients treated with ^{166}Ho -MS RE, the LMD is significantly overestimated by the currently advised lung dosimetry model, which is based on scintigraphic images of the ^{99m}Tc -MAA scout dose. The LMD is also significantly overestimated on quantitative SPECT images of the ^{99m}Tc -MAA scout dose, which indicates that there is a disparity between the particle distributions. The estimated LMD values obtained from SPECT images of the ^{166}Ho -MS scout dose are an accurate predictor of the LMD, which suggests that treatment planning in RE can be improved if the same MS are used for scout dose and treatment.

References

- 1 Coldwell D, Sangro B, Salem R, Wasan H, Kennedy A. Radioembolization in the Treatment of Unresectable Liver Tumors Experience Across a Range of Primary Cancers. *Am J Clin Oncol*. 2012;35:167-177.
- 2 Vente MA, Wondergem M, van der Tweel I et al. Yttrium-90 microsphere radioembolization for the treatment of liver malignancies: a structured meta-analysis. *Eur Radiol*. 2009;19:951-959.
- 3 Riaz A, Lewandowski RJ, Kulik LM et al. Complications Following Radioembolization with Yttrium-90 Microspheres: A Comprehensive Literature Review. *J Vasc Intervent Radiol*. 2009;20:1121-1130.
- 4 Sato K, Lewandowski RJ, Bui JT et al. Treatment of unresectable primary and metastatic liver cancer with yttrium-90 microspheres (TheraSphere): assessment of hepatic arterial embolization. *Cardiovasc Intervent Radiol*. 2006;29:522-529.
- 5 Lam M, Louie J, Iagaru A, Goris M, Sze D. Safety of Repeated Yttrium-90 Radioembolization. *Cardiovasc Intervent Radiol*. 2013;1-9.
- 6 Sangro B, Gil-Alzugaray B, Rodriguez J et al. Liver disease induced by radioembolization of liver tumors. *Cancer*. 2008;112:1538-1546.
- 7 Kennedy AS, McNeillie P, Dezarn WA et al. Treatment Parameters and Outcome in 680 Treatments of Internal Radiation With Resin 90Y-Microspheres for Unresectable Hepatic Tumors. *Int J Radiat Oncol Biol Phys*. 2009;74:1494-1500.
- 8 Lam M, Banerjee S, Louie J et al. Root Cause Analysis of Gastroduodenal Ulceration After Yttrium-90 Radioembolization. *Cardiovasc Intervent Radiol*. 2013;1-12.
- 9 Murthy R, Brown DB, Salem R et al. Gastrointestinal complications associated with hepatic arterial yttrium-90 microsphere therapy. *J Vasc Intervent Radiol*. 2007;18:553-562.
- 10 Leung TWT, Lau WY, Ho SKW et al. Radiation Pneumonitis After Selective Internal Radiation Treatment with Intraarterial (90)Yttrium-Microspheres for Inoperable Hepatic-Tumors. *Int J Radiat Oncol Biol Phys*. 1995;33:919-924.
- 11 Wright CL, Werner JD, Tran JM et al. Radiation Pneumonitis Following Yttrium-90 Radioembolization: Case Report and Literature Review. *J Vasc Intervent Radiol*. 2012;23:669-674.
- 12 Dancey JE, Shepherd FA, Paul K et al. Treatment of nonresectable hepatocellular carcinoma with intrahepatic Y-90-microspheres. *J Nucl Med*. 2000;41:1673-1681.
- 13 Slauson DO, Hahn FF, Benjamin SA, Chiffelle TL, Jones RK. Inflammatory Sequences in Acute Pulmonary Radiation-Injury. *Am J Pathol*. 1976;82:549-&.
- 14 Yorke ED, Jackson A, Rosenzweig KE, Braban L, Leibel SA, Ling CC. Correlation of dosimetric factors and radiation pneumonitis for non small-cell lung cancer patients in a recently completed dose escalation study. *Int J Radiat Oncol Biol Phys*. 2005;63:672-682.
- 15 Ho S, Lau WY, Leung TW, Chan M, Johnson PJ, Li AK. Clinical evaluation of the partition model for estimating radiation doses from yttrium-90 microspheres in the treatment of hepatic cancer. *Eur J Nucl Med*. 1997;24:293-298.
- 16 Kennedy AS, Nag S, Salem R et al. Recommendations for radioembolization of hepatic malignancies using yttrium-90 microsphere brachytherapy: A consensus panel report from the Radioembolization Brachytherapy Oncology Consortium. *Int J Radiat Oncol Biol Phys*. 2007;68:13-23.
- 17 Ho S, Lau WY, Leung TW et al. Partition model for estimating radiation doses from yttrium-90 microspheres in treating hepatic tumours. *Eur J Nucl Med*. 1996;23:947-952.

- 18 Salem R, Parikh P, Atassi B et al. Incidence of Radiation Pneumonitis After Hepatic Intra-Arterial Radiotherapy With Yttrium-90 Microspheres Assuming Uniform Lung Distribution. *Am J Clin Oncol*. 2008;31:431-438.
- 19 Yu N, Srinivas SM, DiFilippo FP et al. Lung Dose Calculation With SPECT/CT for 90Yttrium Radioembolization of Liver Cancer. *Int J Radiat Oncol Biol Phys*. 2013;85:834-839.
- 20 Elschot M, Vermolen BJ, Lam MGEH, de Keizer B, van den Bosch MAAJ, de Jong HWAM. Quantitative Comparison of PET and Bremsstrahlung SPECT for Imaging the In Vivo Yttrium-90 Microsphere Distribution after Liver Radioembolization. *PLoS ONE*. 2013;8:e55742.
- 21 Smits MLJ, Nijsen JFW, van den Bosch MAAJ et al. Holmium-166 radioembolisation in patients with unresectable, chemorefractory liver metastases (HEPAR trial): a phase 1, dose-escalation study. *Lancet Oncol*. 2012;13:1025-1034.
- 22 Seevinck PR, Seppenwoolde JH, de Wit TC et al. Factors affecting the sensitivity and detection limits of MRI, CT, and SPECT for multimodal diagnostic and therapeutic agents. *Anticancer Agents Med Chem*. 2007;7:317-334.
- 23 Zielhuis SW, Nijssen JF, de RR et al. Production of GMP-grade radioactive holmium loaded poly(L-lactic acid) microspheres for clinical application. *Int J Pharm*. 2006;311:69-74.
- 24 Van de Wiele C, Maes A, Brugman E et al. SIRT of liver metastases: physiological and pathophysiological considerations. *Eur J Nucl Med Mol Imaging*. 2012;39:1646-1655.
- 25 Bol GH, Kotte ANTJ, van der Heide UA, Lagendijk JJW. Simultaneous multi-modality ROI delineation in clinical practice. *Comput Methods Programs Biomed*. 2009;96:133-140.
- 26 Smits MLJ, Nijsen JFW, van den Bosch MAAJ et al. Holmium-166 radioembolization for the treatment of patients with liver metastases: design of the phase I HEPAR trial. *J Exp Clin Cancer Res*. 2010;29.
- 27 Salem R, Lewandowski RJ, Sato KT et al. Technical Aspects of Radioembolization with 90Y Microspheres. *Tech Vasc Intervent Radiol*. 2007;10:12-29.
- 28 Zeintl J, Vija AH, Yahil A, Hornegger J, Kuwert T. Quantitative Accuracy of Clinical 99mTc SPECT/CT Using Ordered-Subset Expectation Maximization with 3-Dimensional Resolution Recovery, Attenuation, and Scatter Correction. *J Nucl Med*. 2010;51:921-928.
- 29 Kennedy A, Coldwell D, Sangro B, Wasan H, Salem R. Radioembolization for the Treatment of Liver Tumors: General Principles. *Am J Clin Oncol*. 2012;35.
- 30 van Dyk J, Keane TJ, Rider WD. Lung Density As Measured by Computerized-Tomography - Implications for Radiotherapy. *Int J Radiat Oncol Biol Phys*. 1982;8:1363-1372.
- 31 Sabet A, Ahmadzadehfar H, Muckle M et al. Significance of Oral Administration of Sodium Perchlorate in Planning Liver-Directed Radioembolization. *J Nucl Med*. 2011;52:1063-1067.
- 32 Bult W, Vente MAD, Zonnenberg BA, van het Schip AD, Nijssen JFW. Microsphere, radioembolization of liver malignancies: current developments. *Q J Nucl Med Mol Imaging*. 2009;53:325-335.
- 33 Taplin GV, MacDonald NS. Radiochemistry of macroaggregated albumin and newer lung scanning agents. *Semin Nucl Med*. 1971;1:132-152.
- 34 Zolle I, Bremer PO, J+inoki G. Monographs of 99mTc Pharmaceuticals. In: Zolle I, ed. *Technetium-99m Pharmaceuticals*. Springer Berlin Heidelberg; 2007:173-337.
- 35 Willowson K, Bailey DL, Baldock C. Quantifying lung shunting during planning for radio-embolization. *Phys Med Biol*. 2011;56:N145-N152.
- 36 Ahmadzadehfar H, Sabet A, Biermann K et al. The Significance of (99m)Tc-MAA SPECT/CT Liver Perfusion Imaging in Treatment Planning for (90)Y-Microsphere Selective Internal Radiation Treatment. *J Nucl Med*. 2010;51:1206-1212.
- 37 Lau WY, Kennedy AS, Kim YH et al. Patient Selection and Activity Planning Guide for Selective Internal Radiotherapy with Yttrium-90 Resin Microspheres. *Int J Radiat Oncol Biol Phys*. 2012;82:401-407.

Chapter 7

Summary and general discussion



7.1 Summary

Intra-arterial radioembolization, using microspheres loaded with a high-energy beta-emitting radionuclide (e.g. ^{90}Y or ^{166}Ho), is increasingly applied for treatment of unresectable liver tumors. Image-based treatment planning and evaluation (i.e. dosimetry) is crucial for radioembolization, since treatment safety and efficacy depend on the distribution of the radioactive microspheres over tumorous and healthy tissue. Prior to ^{90}Y microsphere radioembolization, treatment planning is performed on gamma camera images of a scout dose of $^{99\text{m}}\text{Tc}$ -MAA particles, which differ from the ^{90}Y microspheres in size, shape, density, injected particle load and micro-embolic effects. Post-treatment evaluation is performed on either ^{90}Y Bremsstrahlung SPECT or ^{90}Y PET images. In ^{166}Ho radioembolization, the same microspheres may be used for treatment planning (scout dose) and for therapy (treatment dose), since the emission of low-energy gamma photons enables visualization of the ^{166}Ho microsphere distribution with SPECT. This approach can potentially improve the predictive value of the scout dose and may obviate the use of a $^{99\text{m}}\text{Tc}$ -MAA scout dose in ^{166}Ho radioembolization.

Dosimetry in radioembolization requires accurate SPECT- or PET-based quantification of the local amount of $^{99\text{m}}\text{Tc}$ -MAA particles, ^{90}Y microspheres, or ^{166}Ho microspheres. SPECT and PET images are reconstructed from a set of projection data, which are affected by various physical processes, such as photon attenuation and scatter in the patient, photon scatter in the collimator (SPECT) and detector, penetration of high-energy photons through the collimator septa (SPECT), detection of random events (PET), and Poisson noise. All of these effects degrade the visual quality and the quantitative accuracy of the reconstructed images. A general way to correct for these image degrading effects is to incorporate a physical model of the image formation process (i.e. a photon transport model) in the iterative reconstruction algorithm. In SPECT reconstruction, approximate (analytical) models are frequently used for this purpose, mainly because they are computationally efficient. Although these models appear to be sufficiently accurate for $^{99\text{m}}\text{Tc}$, they fall short for radionuclides with more complex photon energy spectra, such as ^{90}Y and ^{166}Ho . The research presented in this thesis aims to develop, evaluate, and exploit quantitative nuclear imaging methods, to enable accurate assessment of the *in vivo* ^{90}Y and ^{166}Ho microsphere distribution for dosimetry in radioembolization.

SPECT reconstruction algorithms can correct for image degrading effects, but only to some extent. The image quality and quantitative accuracy of SPECT is above all dependent on the quality of the acquired projection data. The acquisition settings (i.e. collimator, energy window, number of angles, etc.) should be chosen in such a way that noise is minimized, the resolution is as high as possible, and artifacts are absent in the projection data. Consequently, SPECT-based dosimetry in radioembolization starts with defining the optimal acquisition protocol. In **Chapter 2**, a quantitative evaluation of the gamma camera imaging characteristics of ^{99m}Tc , ^{90}Y , and ^{166}Ho is presented for various acquisition protocols. Using phantom experiments and Monte Carlo simulations, the combination of high-energy collimators and a wide energy window was found to optimize the spatial resolution and primary photon fraction for ^{90}Y . The ^{90}Y and ^{166}Ho images showed a substantially lower spatial resolution, sensitivity, and contrast than ^{99m}Tc images, and were more affected by scatter and collimator-detector effects. The presented characterization provides important information for the development of quantitative reconstruction algorithms for ^{90}Y and ^{166}Ho SPECT. Furthermore, this analysis can guide clinical comparisons between or within radioembolization studies with varying radionuclides and imaging protocols.

Bremsstrahlung SPECT and PET are both used for imaging the ^{90}Y microsphere distribution after radioembolization. Model-based correction techniques for scatter, random, and attenuation effects are clinically available for PET, whereas current clinical ^{90}Y Bremsstrahlung SPECT reconstruction includes (at best) very approximate models for correction of attenuation and collimator-detector effects. Furthermore, clinical PET has a higher spatial resolution than SPECT, because it does not require mechanical collimation. However, the number of positrons emitted by ^{90}Y is much lower than the number of Bremsstrahlung photons created. Consequently, the count rate in ^{90}Y PET is approximately twenty-times lower than in ^{90}Y Bremsstrahlung SPECT. The effect of these subjects on the ^{90}Y image quality is described in **chapter 3**. In this chapter, a quantitative comparison between state-of-the-art clinical Bremsstrahlung SPECT and PET is presented for the assessment of the ^{90}Y microsphere distribution after radioembolization. It was demonstrated in a phantom study, that image contrast was higher with PET than with SPECT. PET was better able to uniquely detect small accumulations of activity than SPECT, which is an important feature for post-treatment evaluation of possible extrahepatic deposition of ^{90}Y microspheres. A clinical study showed substantially higher PET than SPECT-based absorbed dose estimates in those regions of the liver where the microspheres had primarily accumulated. In conclusion, this study shows that state-of-the-art clinical PET is

superior to Bremsstrahlung SPECT for quantitative assessment of the ^{90}Y microsphere distribution after radioembolization.

Advanced reconstruction algorithms, which include correction techniques for the image degrading effects, are clinically available for ^{90}Y PET. If the ^{90}Y Bremsstrahlung SPECT reconstruction algorithms are brought to the same level of development, SPECT could be a practical and cost-effective alternative to ^{90}Y PET. These SPECT reconstruction algorithms require accurate modeling of photon transport, which is complicated by the wide range and the continuous nature of the ^{90}Y Bremsstrahlung photon energy spectrum. A possible solution may be to use fast Monte Carlo simulations for calculation of photon transport during the reconstruction process. Monte Carlo simulations have the hypothetical advantage over more approximate models, that all physics can be accurately included in the photon transport calculations, irrespective of photon energy, scatter order, and other complicating factors. In **chapter 4**, a new reconstruction method for quantitative ^{90}Y Bremsstrahlung SPECT is developed and evaluated (SPECT-MC), which includes Monte Carlo-based photon transport modeling for all photons of the ^{90}Y Bremsstrahlung energy spectrum. In a phantom study, the performance of SPECT-MC was quantitatively evaluated in comparison with state-of-the-art clinical ^{90}Y Bremsstrahlung SPECT and ^{90}Y PET technologies. In comparison with clinical SPECT, image contrast was improved by SPECT-MC and the residual count error, which represents the error in scatter and attenuation corrections, was found to be reduced. In comparison with PET, SPECT-MC images showed lower noise, a lower residual count error, and higher contrast in larger spheres (diameter ≥ 28 mm), which validated the accuracy of the photon transport model used in SPECT-MC reconstruction. PET showed higher image contrast in smaller spheres, due to its superior spatial resolution. It was demonstrated in a clinical study, that in those liver regions where the microspheres had primarily accumulated, SPECT-MC-based mean absorbed dose estimates were consistently higher than their clinical SPECT and PET-based equivalents. The results of this study demonstrate that the quantitative accuracy of ^{90}Y Bremsstrahlung SPECT is substantially improved by Monte Carlo-based modeling of the image degrading effects. Consequently, SPECT-MC may be used as a cost-effective alternative to ^{90}Y PET for quantitative assessment of the microsphere distribution after ^{90}Y radioembolization.

The Monte Carlo-based approach for calculation of photon transport presented in chapter 4 may also be beneficial for SPECT reconstruction of other radionuclides with high-energy photon contributions. This option is investigated for ^{166}Ho in **chapter 5**. In this chapter, a Monte Carlo-based reconstruction method for quantitative ^{166}Ho SPECT

is developed (SPECT-fMC) and evaluated in comparison with two state-of-the-art clinical ^{166}Ho SPECT reconstruction algorithms. Phantom experiments demonstrated that SPECT-fMC significantly improved image contrast, reduced the residual count error, and improved activity quantification, while image noise remained comparable to that of the reference methods. In patients treated with ^{166}Ho microsphere radioembolization, the total administered activity was accurately quantified with SPECT-fMC and tumor absorbed dose estimates were significantly higher than with the reference methods. In conclusion, this study demonstrates that the quantitative accuracy of ^{166}Ho SPECT is significantly improved by Monte Carlo-based modeling of the image degrading effects. SPECT-fMC enables accurate quantification of the ^{166}Ho microsphere distribution in clinical practice, which facilitates image-based treatment planning and evaluation in ^{166}Ho radioembolization.

Arteriovenous shunting of microspheres to the lungs is considered a risk factor of radioembolization, since it may cause serious debilitation of respiratory function (radiation pneumonitis). Therefore, it is of utmost importance to estimate the mean dose to the lungs (LMD) prior to treatment. The aim of **chapter 6** is to evaluate and improve the lung dosimetry model that is currently used for treatment planning in radioembolization. The clinical study protocol for ^{166}Ho radioembolization included both a $^{99\text{m}}\text{Tc}$ -MAA scout dose and a ^{166}Ho microsphere scout dose for prediction of the ^{166}Ho treatment dose distribution. In a clinical study, the LMD was found to be significantly overestimated by the currently used lung dosimetry model, which is based on (planar) scintigraphic images of the $^{99\text{m}}\text{Tc}$ -MAA scout dose. The LMD was also found to be significantly overestimated on quantitative SPECT images of the $^{99\text{m}}\text{Tc}$ -MAA scout dose, but not on quantitative SPECT images of the ^{166}Ho microsphere scout dose. On the SPECT images of the $^{99\text{m}}\text{Tc}$ -MAA scout dose, a homogeneous activity distribution was observed in the lung region, which was not present on the SPECT images of the ^{166}Ho microsphere scout and treatment doses. These results demonstrate that the LMD in ^{166}Ho radioembolization is not accurately predicted by a scout dose of $^{99\text{m}}\text{Tc}$ -MAA particles. Moreover, this study suggests that treatment planning in radioembolization is improved by using the same microspheres for scout dose and treatment. Consequently, some patients scheduled for radioembolization will be unnecessarily treated with a reduced amount of activity, or will be withheld treatment overall, if the lung dosimetry model is not adapted.

7.2 General discussion and future perspectives

In the research presented in this thesis, quantitative nuclear imaging methods were developed, evaluated, and exploited to enable accurate assessment of the *in vivo* ^{90}Y and ^{166}Ho microsphere distribution for dosimetry in radioembolization. This last chapter surveys the performance of the presented quantitative imaging methods and discusses their (future) dosimetric applications, along with other developments aiming to improve personalized treatment planning and evaluation in liver radioembolization.

7.2.1 Quantitative nuclear imaging

The performance of the developed and evaluated quantitative imaging techniques, in comparison with ^{18}F PET and $^{99\text{m}}\text{Tc}$ SPECT, is summarized in Table 7.1. It should be noted that images were acquired under clinically realistic, and therefore unequal, imaging conditions (i.e. activity concentrations, scan times, reconstruction protocols). Under these conditions, image contrast in ^{90}Y PET approximates that of F-18 PET, but image noise and the residual count error, which represents the error in scatter and attenuation corrections (1), are higher. These results are very similar to those reported in literature (2,3). In ^{90}Y Bremsstrahlung SPECT (reconstructed with the method proposed in chapter 4), image contrast is more affected by partial volume effects than in $^{99\text{m}}\text{Tc}$ SPECT, and image noise is higher. The same holds true for ^{166}Ho SPECT in comparison with $^{99\text{m}}\text{Tc}$ SPECT. The residual count errors are similar for ^{90}Y , ^{166}Ho , and $^{99\text{m}}\text{Tc}$ SPECT. It has been shown in chapters 3, 4, and 5 that accurate quantification of the radiation absorbed dose is mainly dependent on high image contrast (or high resolution) and low residual count errors. Low (voxel) noise is less important (but desirable) for dosimetric purposes, since tumor and healthy tissue compartments typically consist of several tens to several tens of thousands of voxels. In smaller tumors, the quantitative values obtained with ^{90}Y PET, ^{90}Y SPECT, and ^{166}Ho SPECT are less reliable, because of the larger influence of image noise and partial volume effects. The latter should always be considered in PET and SPECT for objects smaller than approximately 3 times the system spatial resolution (~ 5 mm and 15 mm FWHM, respectively) (4).

It is noteworthy that contrast, noise, and residual count errors of ^{90}Y PET, ^{90}Y SPECT, and ^{166}Ho SPECT images are similar for spheres ≥ 22 mm, under post-treatment imaging conditions (Table 7.1). However, a very interesting feature of ^{166}Ho SPECT is that it allows for imaging of a scout dose of ^{166}Ho microspheres (~ 250 MBq), thereby

potentially obviating the use of ^{99m}Tc -MAA as microsphere surrogates (see also section 7.2.2). When the same concept is investigated for ^{90}Y radioembolization, a scout dose of maximally 80 MBq may be administered to the patient. This activity is equivalent to 250 MBq of ^{166}Ho in terms of delivered radiation absorbed dose. In comparison with a treatment dose of ^{90}Y microspheres (~ 2000 Mbq), the activity concentration is reduced with a factor of 25. Consequently, the SNR of the ^{90}Y PET and SPECT images will be reduced with a factor of 5. It has been demonstrated that accurate quantification of ^{90}Y with PET is not feasible under these conditions (5). Accordingly, the back-of-the-envelope calculations presented here suggest that accurate quantification of a hypothetical ^{90}Y scout dose will also be (too) challenging with ^{90}Y Bremsstrahlung SPECT. However, further research is required to establish the lower detection limit of the method presented in chapter 4.

Table 7.1. Quantitative imaging characteristics of ^{90}Y PET, ^{90}Y SPECT, and ^{166}Ho SPECT under post-treatment imaging conditions, in comparison with ^{18}F PET and ^{99m}Tc SPECT. All results were obtained with the same anthropomorphic image quality phantom (see chapters 4, 5, and 6) with similar sphere-to-background activity concentration ratios (second column), but with different activity concentrations (third column). The 37 mm sphere was not filled with activity for the ^{18}F PET and ^{99m}Tc SPECT measurements.

Radionuclide and modality	Sphere-to-background ratio	Background activity concentration	Contrast recovery in 13 / 22 / 37 mm sphere	Noise (coefficient of variation)	Residual count error
^{18}F PET ^a	8.3	6.6 kBq ml ⁻¹	51% / 71% / –	15%	9%
^{90}Y PET ^a	8.9	1.1 MBq ml ⁻¹	46% / 66% / 82%	47%	21%
^{99m}Tc SPECT ^b	7.9	34 kBq ml ⁻¹	33% / 65% / –	30%	14%
^{90}Y SPECT ^c	8.9	1.1 MBq ml ⁻¹	6% / 60% / 88%	43%	15%
^{166}Ho SPECT ^d	7.8	185 kBq ml ⁻¹	22% / 58% / 86%	37%	17%

^a reconstruction: OP-OSEM + PSF + TOF (3 iterations; 21 subsets; 5 mm FWHM) (see chapter 3)

^b reconstruction: FLASH3D (16 iterations; 8 subsets) (see chapter 5)

^c reconstruction: SPECT-MC (60 iterations; 8 subsets) (see chapter 4)

^d reconstruction: SPECT-fMC (20 iterations; 8 subsets) (see chapter 5)

7.2.2 Personalized treatment planning

Patient-specific calculation of the radiation absorbed dose to tumorous and normal tissues has been routinely used for treatment planning in external-beam radiation therapy (EBRT) for decades. Treatment planning involves tailoring of physical parameters (viz. beam type, energy, beam exposure time, geometry, etc.) to derive the desired spatial distribution and intensity of the radiation absorbed dose over the tumor and the organs at risk. In radioembolization, however, the spatial distribution of the radiation absorbed dose is solely dependent on the microsphere distribution, which cannot be modified by tweaking physical parameters. Consequently, the

activity to be administered to the patient is the only parameter that can be tailored in treatment planning for radioembolization. Still, the accuracy of treatment planning in EBRT may be approximated if, and only if, i) tumor, healthy liver, and lung compartments are accurately determined, and ii) the microsphere distribution of the treatment dose is accurately predicted by the scout dose. Of the three treatment planning methods currently used in radioembolization, the partition model is the only one that takes both of these criteria into account. Although this model is increasingly recognized as being (scientifically) superior to semi-empiric treatment planning approaches (6-10), its current implementation leaves ample room for improvements and further research.

Delineation of target volumes

Currently, application of the partition model in ^{90}Y radioembolization is only advised in patients with discrete lesions with clearly definable regions-of-interest (9). The rationale behind this is that smaller and diffuse lesions cannot be accurately delineated on anatomical CT images. Under these conditions, application of the partition model is almost entirely restricted to patients with primary liver cancer, since liver metastases generally present as diffuse lesions infiltrating in the healthy liver tissue. In treatment planning for EBRT, ^{18}F -FDG PET is increasingly used in combination with CT and/or MRI. With its ability to distinguish metabolically active disease, PET/CT can provide important (adjunctive) information for tumor delineation (11). Promising results of such a multi-modality imaging approach have also been reported for radioembolization in retrospective studies including patients with liver metastases (10,12) and deserve further research.

Pre-treatment estimation of the microsphere distribution

Accurate pre-treatment estimation of the microsphere distribution over the tumor, healthy liver, and lung compartments is of utmost importance for personalized treatment planning with the partition model. Currently, a scout dose of $^{99\text{m}}\text{Tc}$ -MAA particles is used for this purpose in ^{90}Y and ^{166}Ho radioembolization. Although the $^{99\text{m}}\text{Tc}$ -MAA scout dose effectively predicts (and prevents) microsphere deposition in the gastro-intestinal tract, there are conflicting reports with regard to its validity for prediction of the intrahepatic microsphere distribution (6,10,13,14) and absorbed dose to the lungs in ^{90}Y radioembolization (15). It has been demonstrated in this thesis, that the mean dose to the lungs is significantly overestimated by a scout dose of $^{99\text{m}}\text{Tc}$ -MAA particles in ^{166}Ho radioembolization, whereas it is accurately predicted

by a scout dose of ^{166}Ho microspheres (chapter 6). These findings contribute to the evidence that the distribution of $^{99\text{m}}\text{Tc}$ -MAA particles is different from the distribution of ^{166}Ho and ^{90}Y microspheres and suggest that treatment planning in radioembolization can be improved by using the same microspheres for the scout dose and treatment. A conclusive answer regarding the validity of treatment planning on the $^{99\text{m}}\text{Tc}$ -MAA (and ^{166}Ho microsphere) scout dose can be facilitated by the quantitative imaging methods presented in this thesis. For ^{90}Y radioembolization, the (predicted) radiation absorbed doses delivered to the tumor, healthy liver, and lung compartments should be compared between quantitative SPECT images of the $^{99\text{m}}\text{Tc}$ -MAA scout dose and quantitative Bremsstrahlung SPECT or PET images of the ^{90}Y microsphere treatment dose. Quantitative ^{90}Y SPECT may be preferred over ^{90}Y PET for this purpose, since post-treatment assessment of the mean absorbed dose to the lungs requires imaging with a high sensitivity. For ^{166}Ho radioembolization, the comparison should be performed between quantitative SPECT images of the $^{99\text{m}}\text{Tc}$ -MAA scout dose, the ^{166}Ho microsphere scout dose, and the ^{166}Ho microsphere treatment dose. This is subject of investigation in the phase II clinical trial for ^{166}Ho radioembolization that is currently being performed in our institute. In section 7.2.3, another study is proposed to address these issues.

Towards voxel-based dosimetry

The partition model is based on estimates of the mean radiation absorbed doses in the tumor, healthy liver, and lung compartments. The absorbed dose is assumed to be uniformly distributed within each of these compartments, which is not the case in clinical practice. For example, dose ranges of 100 to 8000 Gy have been found at a microscopic level within and between tumors in explanted livers of patients treated with glass and resin ^{90}Y microspheres (16). For treatment planning in EBRT, (non-) uniformity of the delivered dose is considered an important parameter for prediction of efficacy and toxicity. Since (in theory) a single surviving tumor cell can repopulate the tumor, treatment efficacy depends on the delivery of a sufficiently high dose to the complete tumor (i.e. all tumor cells). Furthermore, for organs with parallel functioning subunits, like the liver and the lungs, toxicity is related to the relative volume of the organ that is irradiated to a certain dose level (17,18). In radioembolization, a highly non-uniform radiation absorbed dose distribution is expected, due to i) a non-uniform distribution of the microspheres (16), and ii) the rapid dose falloff (~ 4 orders of magnitude within the first millimeter) around each single microsphere (19). To take into account the effects of absorbed dose (non-)uniformity within the separate

compartments of the partition model, voxel-based dosimetry methods have been proposed (20,21). These methods calculate the absorbed dose to each voxel, usually by convolution of quantitative images of the activity distribution with a dose point kernel (22), which accounts for the spatially variant energy deposition resulting from the range of the beta particles (and photons). It should be noted that for image-based assessment of the true dose distribution, in theory a spatial resolution comparable to the size of the microspheres is required. Obviously, this is not feasible in clinical practice with the currently available nuclear imaging techniques. The exact relation between imaging resolution and the accuracy of voxel-based dosimetry needs further investigation. Still, voxel-based dosimetry enables approximate estimation of various dosimetric parameters, which include mean dose, maximum dose, minimum dose, dose uniformity, dose conformity, V_x values (i.e. the (relative) volume receiving X Gy or more), and dose volume histograms in the tumor, healthy liver, and lung compartments. Subsequently, radiobiological models can be used to correlate these dosimetric parameters to clinical outcome, in terms of tumor control probability (TCP) and normal tissue complication probability (NTCP) (21,23).

7.2.3 Recommendations

Various recommendations for advancing dosimetry in radioembolization have been discussed in the previous sections, including quantitative assessment of the microsphere distribution with SPECT and PET, the use of FDG-PET/CT for region-of-interest delineation in the partition model, and voxel-based dosimetry and radiobiological modeling for treatment planning and evaluation. These recommendations should all be incorporated in an advanced dose-escalation study, which aims to establish i) the validity of treatment planning on a scout dose, and ii) which dosimetric parameters (i.e. mean dose, V_x , etc.) are correlated with treatment efficacy (TCP) and liver and lung toxicity (NTCP). In the proposed study design (Figure 7.1), the distribution of the scout dose over the partition model compartments will be used to calculate the activity that is required to deliver a certain mean radiation absorbed dose to the healthy liver. This radiation absorbed dose to the healthy liver should be escalated to the point where toxicity starts to be observed. With the proposed study, the validity of the scout dose may be established and the required parameters for personalized dosimetry in ^{90}Y and ^{166}Ho radioembolization may be determined.

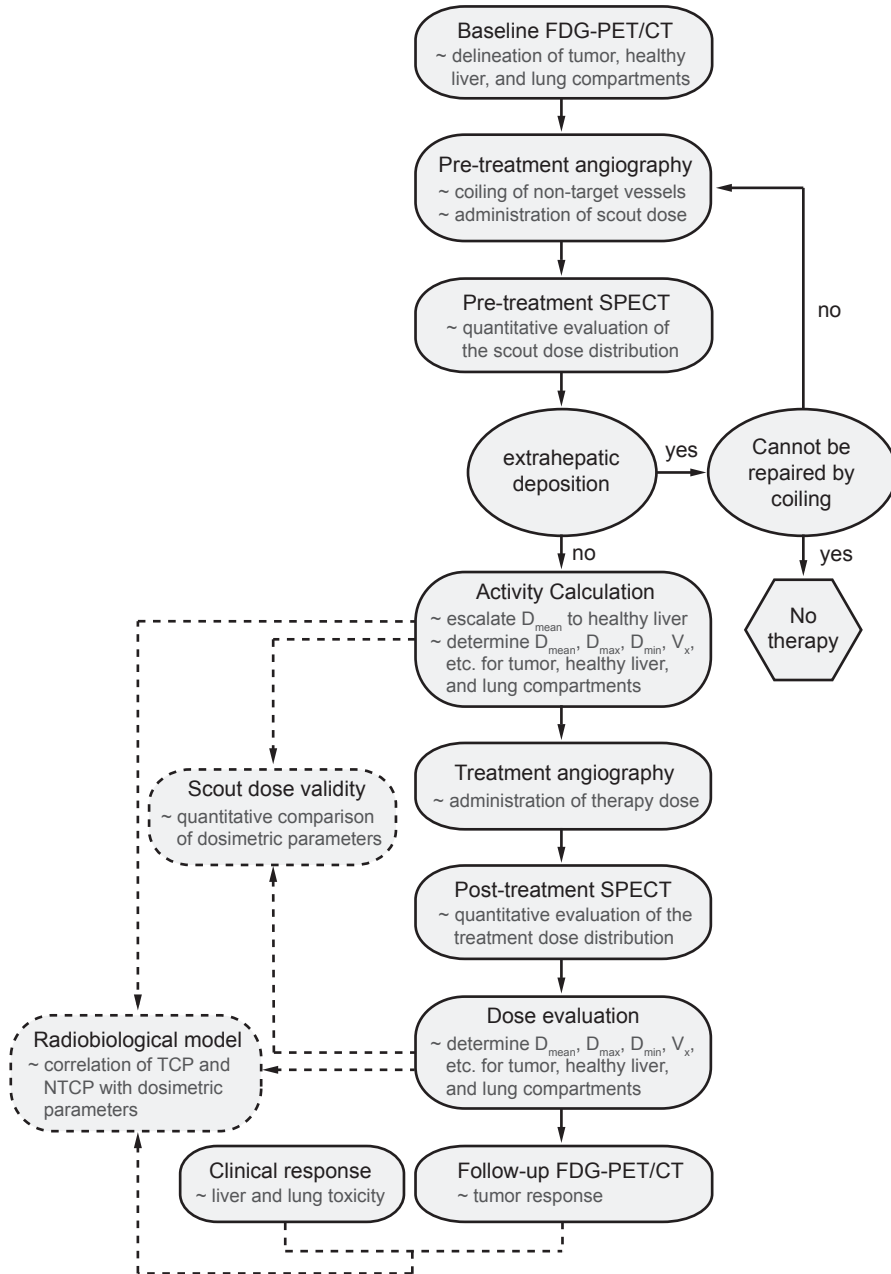


Figure 7.1. An overview of the design of the proposed dose-escalation study for ^{90}Y and ^{166}Ho radioembolization (see section 7.2.3). The research questions are indicated in the boxes with the dashed borders.

7.2.4 Conclusions

In the research presented in this thesis, quantitative nuclear imaging methods were developed, evaluated, and exploited to enable accurate assessment of the in vivo ^{90}Y and ^{166}Ho microsphere distribution for dosimetry in radioembolization.

The most important conclusions are:

- The quantitative accuracy of ^{166}Ho SPECT and ^{90}Y Bremsstrahlung SPECT is substantially improved by incorporation of a Monte Carlo-based model of the image degrading effects in the iterative reconstruction algorithm (chapters 4 and 5)
- Both ^{90}Y PET and ^{90}Y Bremsstrahlung SPECT can be reliably used for post-treatment dosimetry in ^{90}Y radioembolization, if accurate correction methods for the image degrading effects are applied (chapters 3 and 4)
- The distribution of both a scout dose and a treatment dose of ^{166}Ho microspheres can be accurately assessed with quantitative SPECT in ^{166}Ho radioembolization (chapter 5)
- Treatment planning in ^{166}Ho radioembolization can be improved by using the same microspheres for scout dose and treatment (chapter 6)

References

- 1 National Electrical Manufacturers Association. NEMA Standards Publication NU 2-2007: Performance Measurements of Positron Emission Tomographs. 2007. Rosslyn, VA, National Electrical Manufacturers Association.
- 2 Willowson K, Forwood N, Jakoby BW, Smith AM, Bailey DL. Quantitative Y-90 image reconstruction in PET. *Med Phys*. 2012;39:7153-7159.
- 3 van Elmbt L, Walrand S, Lhommel R, Jamar F, Pauwels S. Quantitative comparison between LYSO and BGO PET-tomographs in 90Y imaging. *Eur J Nucl Med Mol Imaging*. 2010;37:S293.
- 4 Bailey DL, Willowson KP. An Evidence-Based Review of Quantitative SPECT Imaging and Potential Clinical Applications. *J Nucl Med*. 2013;54:83-89.
- 5 Carlier T, Eugene T, Bodet-Milin C et al. Assessment of acquisition protocols for routine imaging of Y-90 using PET/CT. *EJNMMI Res*. 2013;3:11.
- 6 Kao YH, Tan AEH, Burgmans MC et al. Image-Guided Personalized Predictive Dosimetry by Artery-Specific SPECT/CT Partition Modeling for Safe and Effective Y-90 Radioembolization. *J Nucl Med*. 2012;53:559-566.
- 7 Kao YH, Tan EH, Ng CE, Goh SW. Clinical implications of the body surface area method versus partition model dosimetry for yttrium-90 radioembolization using resin microspheres: a technical review. *Ann Nucl Med*. 2011;25:455-461.
- 8 Garin E, Lenoir L, Rolland Y et al. Dosimetry Based on Tc-99m-Macroaggregated Albumin SPECT/CT Accurately Predicts Tumor Response and Survival in Hepatocellular Carcinoma Patients Treated with Y-90-Loaded Glass Microspheres: Preliminary Results. *J Nucl Med*. 2012;53:255-263.
- 9 Lau WY, Kennedy AS, Kim YH et al. Patient Selection and Activity Planning Guide for Selective Internal Radiotherapy with Yttrium-90 Resin Microspheres. *Int J Radiat Oncol Biol Phys*. 2012;82:401-407.
- 10 Flamen P, Vanderlinden B, Delatte P et al. Multimodality imaging can predict the metabolic response of unresectable colorectal liver metastases to radioembolization therapy with Yttrium-90 labeled resin microspheres. *Phys Med Biol*. 2008;53:6591-6603.
- 11 Ford EC, Herman J, Yorke E, Wahl RL. 18F-FDG PET/CT for Image-Guided and Intensity-Modulated Radiotherapy. *J Nucl Med*. 2009;50:1655-1665.
- 12 Walrand S, Lhommel R, Goffette P, Van den Eynde M, Pauwels S, Jamar F. Hemoglobin level significantly impacts the tumor cell survival fraction in humans after internal radiotherapy. *EJNMMI Res*. 2012;2:20.
- 13 Atul D, Prue L, Richard S Stubbs. Relationship of 99mtechnetium labelled macroaggregated albumin (99mTc-MAA) uptake by colorectal liver metastases to response following Selective Internal Radiation Therapy (SIRT). *BMC Nucl Med*. 2005;5:7.
- 14 Knesaurek K, Machac J, Muzinic M, DaCosta M, Zhang Z, Heiba S. Quantitative comparison of yttrium-90 (90Y)-microspheres and technetium-99m (99mTc)-macroaggregated albumin SPECT images for planning 90Y therapy of liver cancer. *Technol Cancer Res Treat*. 2010;9:253-262.
- 15 Salem R, Parikh P, Atassi B et al. Incidence of Radiation Pneumonitis After Hepatic Intra-Arterial Radiotherapy With Yttrium-90 Microspheres Assuming Uniform Lung Distribution. *Am J Clin Oncol*. 2008;31:431-438.
- 16 Kennedy AS, Nutting C, Coldwell D, Gaiser J, Drachenberg C. Pathologic response and microdosimetry of Y-90 microspheres in man: Review of four explanted whole livers. In *Int J Radiat Oncol Biol Phys*. 2004;60:1552-1563.

- 17 Jackson A, Ten Haken RK, Robertson JM, Kessler ML, Kutcher GJ, Lawrence TS. Analysis of clinical complication data for radiation hepatitis using a parallel architecture model. *Int J Radiat Oncol Biol Phys.* 1995;31:883-891.
- 18 Graham MV, Purdy JA, Emami B et al. Clinical dose-volume histogram analysis for pneumonitis after 3D treatment for non-small cell lung cancer (NSCLC). *Int J Radiat Oncol Biol Phys.* 1999;45:323-329.
- 19 Gulec SA, Szejnberg ML, Siegel JA, Jevremovic T, Stabin M. Hepatic Structural Dosimetry in 90Y Microsphere Treatment: A Monte Carlo Modeling Approach Based on Lobular Microanatomy. *J Nucl Med.* 2010;51:301-310.
- 20 Sarfaraz M, Kennedy AS, Lodge MA, Li XA, Wu XG, Yu CX. Radiation absorbed dose distribution in a patient treated with yttrium-90 microspheres for hepatocellular carcinoma. *Med Phys.* 2004;31:2449-2453.
- 21 Chiesa C, Maccauro M, Romito R et al. Need, feasibility and convenience of dosimetric treatment planning in liver selective internal radiation therapy with Y-90 microspheres: the experience of the National Cancer Institute of Milan. *Q J Nucl Med Mol Imaging.* 2011;55:168-197.
- 22 Bolch WE, Bouchet LG, Robertson JS et al. MIRD pamphlet No. 17: the dosimetry of nonuniform activity distributions--radionuclide S values at the voxel level. Medical Internal Radiation Dose Committee. *J Nucl Med.* 1999;40:11S-36S.
- 23 Strigari L, Sciuto R, Rea S et al. Efficacy and Toxicity Related to Treatment of Hepatocellular Carcinoma with Y-90-SIR Spheres: Radiobiologic Considerations. *J Nucl Med.* 2010;51:1377-1385.

Addenda

Samenvatting in het Nederlands

Dankwoord/Acknowledgments

List of affiliations

List of publications

Curriculum Vitae



Samenvatting in het Nederlands

Radioembolisatie wordt steeds vaker toegepast voor het behandelen van levertumoren die niet chirurgisch verwijderd kunnen worden. Het principe van radioembolisatie is dat er kleine radioactieve bolletjes, zogenaamde microsferen, via een katheter worden toegediend in de leverslagader. Deze microsferen zijn beladen met een radionuclide (een radioactieve stof) die hoog-energetische beta-deeltjes (electronen) uitzendt, zoals yttrium-90 (^{90}Y) en holmium-166 (^{166}Ho). Door de specifieke anatomie van de lever is het de verwachting dat de microsferen voornamelijk in het vaatbed in en rond de tumoren terecht komen, met het gewenste gevolg dat het tumorweefsel een hogere stralingsdosis krijgt dan het gezonde leverweefsel. Bij radioembolisatie is het bepalen van de te geven dosis (planning) en het controleren van de verdeling daarvan in de patient (evaluatie) van cruciaal belang, omdat zowel de effectiviteit als de veiligheid van de therapie afhankelijk is van de stralingsdosis op de tumoren en het gezonde weefsel. Daartoe wordt voorafgaand aan de therapie (d.w.z., de zogenaamde behandeldosis) alvast een kleine hoeveelheid deeltjes toegediend, de zogenaamde scoutdosis, met als doel de verdeling van de behandeldosis te voorspellen. Voor het afbeelden van de scoutdosis (voor therapie planning) en de behandeldosis (voor therapie evaluatie) kan gebruik gemaakt worden van de nucleaire beeldvormingstechnieken *single photon emission computed tomography* (SPECT) en *positron emission tomography* (PET). Een SPECT scanner is ontworpen voor het drie-dimensionaal (3D) afbeelden van radionucliden die gammafotonen uitzenden, terwijl een PET scanner is gemaakt voor het afbeelden van radionucliden die positronen uitzenden.

Ondanks dat ^{90}Y geen gammafotonen uitzendt, kan het toch worden afgebeeld met een SPECT scanner. Hiervoor wordt gebruikt gemaakt van zogenaamde Bremsstrahlungsfotonen, die worden gecreëerd bij afremming van de beta-deeltjes door het omringende weefsel. Door de beperkte kwaliteit van deze Bremsstrahlung SPECT beelden is het echter niet mogelijk om een scoutdosis van ^{90}Y microsferen betrouwbaar in beeld te brengen. Daarom wordt voor het plannen van radioembolisatie met ^{90}Y microsferen een scoutdosis van *technetium-99m macro-aggregated albumin* ($^{99\text{m}}\text{Tc}$ -MAA) deeltjes toegediend, die vervolgens wordt afgebeeld met SPECT. Deze $^{99\text{m}}\text{Tc}$ -MAA deeltjes dienen als surrogaat voor de ^{90}Y microsferen, maar zijn verschillend in grootte, vorm, dichtheid, en het aantal toegediende deeltjes, waardoor de verdeling binnen en buiten de lever kan afwijken van de uiteindelijke verdeling van de ^{90}Y microsferen. Na radioembolisatie met ^{90}Y

microsferen, kan de verdeling van de behandeldosis worden geëvalueerd met behulp van Bremsstrahlung SPECT of PET beelden.

In tegenstelling tot bij ^{90}Y radioembolisatie, kunnen bij radioembolisatie met ^{166}Ho microsferen mogelijk dezelfde microsferen gebruikt worden voor de scoutdosis als voor de behandeldosis, omdat ^{166}Ho naast beta-deeltjes ook laag-energetische gammafotonen uitzendt. Deze fotonen kunnen goed in beeld gebracht worden met SPECT, wat het bepalen van de verdeling van een kleine hoeveelheid ^{166}Ho microsferen mogelijk maakt. Ten opzichte van een scoutdosis van $^{99\text{m}}\text{Tc-MAA}$ deeltjes, kan het gebruik van dezelfde microsferen voor de scout- en behandeldosis potentieel leiden tot een verbetering in voorspellende waarde van de scoutdosis.

Planning en evaluatie van de stralingsdosis bij radioembolisatie, oftewel dosimetrie, vereist nauwkeurige, op SPECT of PET beelden gebaseerde kwantificatie van de lokale hoeveelheid $^{99\text{m}}\text{Tc-MAA}$ deeltjes, ^{90}Y microsferen, of ^{166}Ho microsferen. Bij zowel SPECT als PET wordt een 3D beeld van de radionuclideverdeling in de patient gereconstrueerd vanuit opgenomen 2D projectiebeelden. De kwaliteit van deze 2D projectiebeelden wordt (negatief) beïnvloed door een aantal fysische processen, waaronder verzwakking en verstrooiing van de uitgezonden fotonen in de patient, en penetratie van hoog-energetische fotonen door de collimator (dat is het onderdeel van de SPECT scanner dat er voor moet zorgen dat alleen fotonen die loodrecht op de camera vallen gedetecteerd worden). Deze en andere effecten verminderen de visuele kwaliteit en de kwantitatieve nauwkeurigheid van de gereconstrueerde 3D beelden. Een manier om voor deze effecten te corrigeren, is door een fysisch model van het beeldvormingsproces, een zogenaamd foton transportmodel, te includeren in de reconstructie. Het doel van het foton transportmodel is om zo nauwkeurig mogelijk te voorspellen hoe de 2D projectiebeelden er uit komen te zien, gegeven een bepaalde schatting van de 3D radionuclideverdeling in de patient. Populair gezegd wordt, tijdens de reconstructie, de geschatte 3D radionuclideverdeling net zo lang aangepast totdat de gemodeleerde 2D projectiebeelden overeenkomen met de gemeten 2D projectiebeelden, en dus de geschatte 3D radionuclideverdeling met de werkelijke 3D radionuclideverdeling. Het is dan wel van cruciaal belang dat het foton transportmodel het beeldvormingsproces accuraat modeleert. Momenteel wordt vooral gebruik gemaakt van (relatief eenvoudige) analytische foton transportmodellen, omdat deze efficiënt berekend kunnen worden. Hoewel deze analytische modellen goed genoeg blijken te werken voor radionucliden met relatief weinig verstoring, zoals $^{99\text{m}}\text{Tc}$, zijn ze niet uitgebreid genoeg voor radionucliden met complexere energiespectra, zoals ^{90}Y en ^{166}Ho . Het onderzoek dat in dit proefschrift

gepresenteerd wordt, is gericht op het ontwikkelen, evalueren, en toepassen van nucleaire beeldvormingstechnieken om de verdeling van ^{90}Y en ^{166}Ho microsferen in de patient accuraat te bepalen, ten behoeve van dosimetrie bij radioembolisatie.

Met slimme SPECT reconstructiealgoritmes kan gecorrigeerd worden voor effecten die de beelden verstoren, maar slechts in beperkte mate. De beeldkwaliteit en kwantitatieve nauwkeurigheid is vooral afhankelijk van de kwaliteit van de opgenomen projectiebeelden. De acquisitieparameters (zoals de gebruikte collimator, het energie venster, het aantal opname hoeken, enz.) moet daarom op zo'n manier gekozen worden dat de ruis geminimaliseerd wordt, de resolutie (d.w.z. het onderscheidend vermogen) zo hoog mogelijk is, en artefacten afwezig zijn in de projectiebeelden. Dientengevolge begint dosimetrie op basis van SPECT beelden met het definiëren van het optimale acquisitieprotocol. In **hoofdstuk 2** wordt een kwantitatieve evaluatie van de karakteristieken van $^{99\text{m}}\text{Tc}$, ^{90}Y , en ^{166}Ho projectiebeelden gepresenteerd voor verschillende acquisitieprotocollen. Met fantoomexperimenten (een nagebootste klinische situatie) en Monte Carlo simulaties (een numerieke simulatie methode) werd gevonden dat voor ^{90}Y , de combinatie van *high-energy* collimatoren en een breed energie venster leidt tot een optimale spatiële resolutie en het hoogste percentage primaire fotonen (d.w.z. fotonen die niet verstrooid zijn, of op een andere manier de beeldkwaliteit negatief beïnvloeden). De ^{90}Y en ^{166}Ho beelden hadden een substantieel lagere resolutie, sensitiviteit, en contrast in vergelijking met $^{99\text{m}}\text{Tc}$ beelden. Bovendien waren de ^{90}Y en ^{166}Ho beelden meer beïnvloed door verstrooide fotonen en door interactie van fotonen met de collimator en/of de detector. De gepresenteerde beeldkarakterisatie verschaft belangrijke informatie voor het ontwikkelen van kwantitatieve reconstructiealgoritmes voor ^{90}Y en ^{166}Ho SPECT. Daarnaast ondersteunt deze analyse klinische vergelijkingen binnen of tussen radioembolisatiestudies met verschillende radionucliden.

Bremsstrahlung SPECT en PET worden beiden gebruikt voor het afbeelden van de verdeling van ^{90}Y microsferen na radioembolisatie. Geavanceerde correctie technieken voor foton verzwakking, verstrooiing, en toevalsdetecties zijn klinisch beschikbaar voor PET, terwijl de ^{90}Y Bremsstrahlung SPECT reconstructie algoritmes die op dit moment beschikbaar zijn in de kliniek (op zijn best) eenvoudige modellen voor foton verzwakking en collimator-detector effecten bevatten. Daarnaast heeft PET een betere spatiële resolutie dan SPECT, omdat een mechanische collimator niet nodig is. Echter, het aantal positronen dat uitgezonden wordt tijdens ^{90}Y verval is veel lager dan het aantal Bremsstrahlungsfotonen dat gecreëerd wordt. Het effect

van deze onderwerpen op de ^{90}Y beeld kwaliteit is beschreven in **hoofdstuk 3**. In dit hoofdstuk wordt een kwantitatieve vergelijking gepresenteerd tussen *state-of-the-art* klinische Bremsstrahlung SPECT en PET voor het bepalen van de verdeling van de ^{90}Y microsferen na radioembolisatie. Met een fantoomstudie werd aangetoond dat het contrast hoger was in de PET beelden dan in de SPECT beelden. PET was ook beter in staat om kleine accumulaties van microsferen uniek te detecteren, hetgeen een belangrijke eigenschap is voor evaluatie van mogelijke depositie van ^{90}Y microsferen buiten de lever. Door middel van een klinische studie werd aangetoond dat in de regionen van de lever waar de microsferen voornamelijk geaccumuleerd waren, de geschatte geabsorbeerde dosis substantieel hoger was op basis van de PET beelden dan op basis van de SPECT beelden. Op basis van deze resultaten kan er geconcludeerd worden dat *state-of-the-art* ^{90}Y PET superieur is aan ^{90}Y Bremsstrahlung SPECT voor het kwantitatief bepalen van de verdeling van de ^{90}Y microsferen na radioembolisatie.

Geavanceerde reconstructiealgoritmes, die corrigeren voor de fysische processen die de beeldkwaliteit verminderen, zijn klinisch beschikbaar voor ^{90}Y PET. Als ^{90}Y Bremsstrahlung SPECT reconstructie naar eenzelfde ontwikkelingsniveau kan worden gebracht, zou SPECT een praktisch en kosteneffectief alternatief kunnen vormen voor ^{90}Y PET. Dergelijke SPECT reconstructiealgoritmes vereisen een accuraat foton transportmodel, hetgeen bemoeilijkt wordt door de wijde bandbreedte en het continue karakter van het ^{90}Y Bremsstrahlung energiespectrum. Dit zou opgelost kunnen worden met snelle Monte Carlo simulaties voor het berekenen van foton transport gedurende het reconstructieproces. Monte Carlo simulaties hebben het hypothetische voordeel ten opzichte van eenvoudiger modellen, dat alle fysica meegenomen kan worden in de foton transport berekeningen, ongeacht de energie van het foton, hoe vaak het foton verstrooid is, een variërende dichtheid van het weefsel, en andere complicerende factoren. In **hoofdstuk 4** wordt een nieuwe reconstructiemethode, SPECT-MC, voor kwantitatieve ^{90}Y Bremsstrahlung SPECT ontwikkeld en geëvalueerd, met een op Monte Carlo berekeningen gebaseerd foton transportmodel voor alle fotonen van het ^{90}Y energie spectrum. De prestaties van SPECT-MC werden met behulp van een fantoomstudie kwantitatief geëvalueerd en vergeleken met *state-of-the-art* klinische ^{90}Y Bremsstrahlung SPECT en ^{90}Y PET reconstructietechnieken. Ten opzichte van klinische SPECT reconstructie, verbeterde SPECT-MC het contrast in de beelden en de correctie voor foton verzwakking en verstrooiing. In vergelijking met PET liet SPECT-MC een verlaagd ruisniveau zien, een betere correctie voor foton verzwakking en verstrooiing, en een hoger contrast in bollen met een diameter groter dan of gelijk aan 28 millimeter. In de kleinere bollen

was het contrast in de PET beelden hoger, vanwege de hogere spatiële resolutie van deze techniek. Met een klinische studie werd aangetoond dat in de lever regionen waar concentratie van ^{90}Y microsferen hoog was, de geschatte geabsorbeerde dosis consistent hoger was op basis van de SPECT-MC beelden dan op basis van de klinische SPECT en PET beelden. De resultaten van deze studie laten zien dat de kwantitatieve nauwkeurigheid van ^{90}Y Bremsstrahlung SPECT beelden aanzienlijk wordt verbeterd door het modeleren van beeldverstorende effecten met behulp van Monte Carlo simulaties (SPECT-MC). Derhalve kan SPECT-MC gebruikt worden als een kosteneffectief alternatief voor ^{90}Y PET, voor het kwantitatief bepalen van de verdeling van de microsferen na ^{90}Y radioembolisatie.

Het modeleren van foton transport op basis van Monte Carlo simulaties, zoals gepresenteerd in hoofdstuk 4, zou ook voordelig kunnen zijn voor de reconstructie van SPECT beelden van andere radionucliden met bijdragen van hoog-energetische fotonen. Deze mogelijkheid wordt in **hoofdstuk 5** onderzocht voor ^{166}Ho . In dit hoofdstuk wordt een nieuwe ^{166}Ho SPECT reconstructie methode (SPECT-fMC), gebaseerd op foton transport berekeningen met Monte Carlo simulaties, ontwikkeld en geëvalueerd in vergelijking met twee *state-of-the-art* klinische ^{166}Ho SPECT reconstructiealgoritmes. Met fantoom experimenten werd aangetoond dat SPECT-fMC reconstructie het contrast, de correctie voor foton verzwakking en verstrooiing, en de kwantificatie van activiteit significant verbeterde, terwijl het ruisniveau vergelijkbaar bleef met dat van de referentiemethoden. In patiënten behandeld met radioembolisatie met ^{166}Ho microsferen, werd de totale activiteit die toegediend was nauwkeurig gekwantificeerd met SPECT-fMC. De geschatte geabsorbeerde dosis op de tumoren was significant hoger met SPECT-fMC dan met de referentiemethoden. Deze resultaten tonen aan dat de kwantitatieve nauwkeurigheid van ^{166}Ho SPECT significant verbeterd wordt door het modeleren van de beeldverstorende effecten met Monte Carlo simulaties. Met SPECT-fMC is het daarom mogelijk om de verdeling van de ^{166}Ho microsferen in de patiënt nauwkeurig te kwantificeren. Dit alles faciliteert planning en evaluatie van de ^{166}Ho radioembolisatie behandeling op basis van SPECT beelden.

Bij radioembolisatie kan het voorkomen dat een gedeelte van de microsferen niet vastloopt in de lever, maar “doorschiet” (*shunt*) naar de longen. Dit wordt beschouwd als een risicofactor voor de patiënt, aangezien het kan leiden tot serieuze verzwakking van de longfunctie. Daarom is het van groot belang om voorafgaand aan de therapie een schatting van de gemiddelde dosis op de longen te maken. Het doel van **hoofdstuk 6** is om het long dosimetrie model dat momenteel

gebruikt wordt voor het plannen van de radioembolisatie behandeling te evalueren en te verbeteren. Het klinisch protocol voor ^{166}Ho radioembolisatie bevat zowel een $^{99\text{m}}\text{Tc}$ -MAA scoutdosis, als ook een scoutdosis van ^{166}Ho microsferen voor het voorspellen van de verdeling van de ^{166}Ho behandeldosis. Met een klinische studie werd aangetoond dat het long dosimetrie model dat momenteel gebruikt wordt, gebaseerd op (planair) scintigrafische (d.w.z., 2D) beelden van de $^{99\text{m}}\text{Tc}$ -MAA scoutdosis, de dosis op de longen significant overschat. De dosis op de longen werd ook overschat op kwantitatieve SPECT beelden van de $^{99\text{m}}\text{Tc}$ -MAA scoutdosis, maar niet op kwantitatieve SPECT beelden van de scoutdosis van ^{166}Ho microsferen. Op de SPECT beelden van de $^{99\text{m}}\text{Tc}$ -MAA scoutdosis werd een homogene activiteitsverdeling waargenomen, die niet aanwezig was op de SPECT beelden van de scoutdosis van ^{166}Ho microsferen. Deze resultaten tonen aan dat de dosis op de longen bij ^{166}Ho radioembolisatie niet nauwkeurig voorspeld wordt door een scoutdosis van $^{99\text{m}}\text{Tc}$ -MAA. Bovendien suggereren de resultaten van deze studie dat het plannen van de radioembolisatie behandeling verbeterd kan worden door dezelfde soort microsferen te gebruiken voor de scoutdosis als voor behandeling. Indien het long dosimetrie model niet aangepast wordt, zullen sommige radioembolisatie patiënten onnodig behandeld worden met een gereduceerde hoeveelheid activiteit, of zelfs onterecht onthouden worden van behandeling.

Het onderzoek dat in dit proefschrift gepresenteerd wordt, beschrijft het ontwikkelen, evalueren, en toepassen van kwantitatieve nucleaire beeldvormingstechnieken voor het nauwkeurig bepalen van de verdeling van ^{90}Y en ^{166}Ho microsferen in de patiënt, ten behoeve van dosimetrie bij radioembolisatie. De belangrijkste conclusies zijn:

- De kwantitatieve nauwkeurigheid van ^{166}Ho SPECT en ^{90}Y Bremsstrahlung SPECT wordt substantieel verbeterd door de beeldverstorende effecten te modeleren met Monte Carlo simulaties tijdens het iteratieve reconstructie proces (hoofdstukken 4 en 5)
- Zowel ^{90}Y PET als ^{90}Y Bremsstrahlung SPECT kunnen met vertrouwen gebruikt worden voor dosimetrie na ^{90}Y radioembolisatie, mits nauwkeurige correctie methodes voor beeldverstorende effecten toegepast worden (hoofdstukken 3 en 4)
- De verdeling van zowel de scoutdosis als de behandeldosis van ^{166}Ho microsferen kan nauwkeurig bepaald worden met kwantitatieve SPECT bij ^{166}Ho radioembolisatie (hoofdstuk 5)
- Het plannen van de ^{166}Ho radioembolisatie behandeling kan verbeterd worden door het gebruik van dezelfde microsferen voor de scoutdosis en de behandeling (hoofdstuk 6)

Addenda

Samenvatting in het Nederlands

Dankwoord/Acknowledgments

List of affiliations

List of publications

Curriculum Vitae



Dankwoord/Acknowledgments

En dan nog het dankwoord. Als het een beetje meezit, schrijf ik vandaag dit dankwoord af, wat zou betekenen dat ik de laatste letter van dit proefschrift, precies 4 jaar nadat ik ben begonnen, op papier zet. Dat dat gelukt is heb ik te danken aan een flink aantal mensen, die direct of van een afstandje betrokken zijn geweest bij het tot stand komen van dit proefschrift, of zich hebben laten gebruiken voor morele ondersteuning en/of afleiding. Ik heb de afgelopen 4 jaar met zeer veel plezier kunnen werken, waarvoor ik iedereen graag wil bedanken.

Om te beginnen wil ik mijn co-promotor dr. ir. Hugo de Jong en mijn promotoren prof. dr. ir. Max Viergever en prof. dr. Maurice van den Bosch bedanken. Beste Hugo, samen met Alan behoorde ik tot de eerste promovendi die jij begeleidde. Van enige onervarenheid op dit gebied heb ik echter nooit iets gemerkt. In tegendeel zelfs. Je was altijd bereikbaar en je enthousiaste, doelgerichte, en zeer betrokken manier van werken heeft me scherp gehouden. Beste Max, jouw ervaring is enorm waardevol voor mij geweest in dit laatste jaar. Gezien het feit dat ik zeker niet je enige promovendus ben, vind ik je betrokkenheid ongekend. Beste Maurice, jouw enthousiasme en drang naar innovatie heeft er mede toe geleid dat radioembolisatie niet alleen in Utrecht, maar in heel Nederland op de kaart staat.

De leden van de beoordelingscommissie, prof. dr. E.E. Voest, prof. dr. ir. J.J.W. Lagendijk, prof. dr. ir. W.E. Hennink, prof. dr. R. Boellaard en prof. dr. J. Kirpensteijn, wil ik bedanken voor hun bereidheid tot het beoordelen van dit proefschrift. Prof. dr. ir. Lagendijk, beste Jan, bedankt dat je me de kans hebt gegeven me als wetenschapper te ontwikkelen binnen het UMC Utrecht en voor de begeleiding gedurende de eerste 3 jaren van mijn promotie.

Tijdens de afgelopen 4 jaren in het UMC heb ik evenzoveel kamers versleten en nog een aantal meer kamergenoten. Allen wil ik bedanken voor de goede sfeer, de vele, vele bakkies koffie en de aangename discussies, die vaak van wetenschappelijke aard waren, soms maatschappelijke dilemma's aansneden, maar gelukkig nog vaker over complete onzin gingen. Na enkele initiële omzwervingen kwam ik op de kamer terecht bij Wouter Bult, die het afronden van zijn proefschrift op wonderbaarlijke wijze combineerde met een onverzettelijk goed humeur. Wouter, aan jouw houding heb ik in de afgelopen maanden een voorbeeld proberen te nemen, wat helaas niet altijd gelukt is, ben ik bang. *Wouter left and was replaced by Alan Riordan. Alan, I don't think I have ever met anyone more laid-back than you are. All the best with finishing your thesis on CT perfusion and try not to lose it (I mean, really, don't*

lose the manuscript...). Na nog twee verhuizingen voegden Casper Beijst en Edwin Bennink zich bij ons. Casper, onze Bob de Bouwer, als je na een jaar al een nieuwe imaging modaliteit en een nieuwe collimator op je naam hebt staan, volgen die publicaties (bijna) vanzelf. Edwin, onze enige *echte* programmeur, succes met het CT perfusie onderzoek dat je uitvoert in samenwerking met nieuwste aanwinst Jaap Oosterbroek.

Mijn dank gaat ook uit naar de heren klinisch fysici (al dan niet in opleiding) Arnold Schilham, Bart Vermolen, Rob van Rooij, en Tim de Wit (inmiddels AMC). In tegenstelling tot de daaraan voorafgaande telefoongesprekken (“Lunch?”, “Ja.”), waren de lunches en aansluitende koffie pauzes wél gezellig. Bart, bedankt voor de prettige samenwerking tijdens de ⁹⁰Y PET/SPECT studie.

Frank Nijsen, zonder jou geen holmium radioembolisatie; ik wens je enorm veel succes met de volgende spannende stappen. Remmert de Roos, dankzij jou lag er altijd een spuitje holmium klaar als ik dat nodig had voor een fantoom experiment; duizend maal dank daarvoor. Marnix Lam en Maarten Smits, ik heb nooit het gevoel gehad dat we enorm langs elkaar heen gepraat hebben, wat vrij ongebruikelijk is voor mensen met ons emploi. Dank voor alle discussies en de vele, snelle, en altijd nuttige klinische input op mijn papers. Maarten Vente, sinds jouw vertrek heeft de holmium groep behoorlijk aan feitenkennis en mooie verhalen ingeboet. Dat je onder de vlag van Sirtex menig ziekenhuis in Nederland aan de radioembolisatie krijgt is zeer waardevol! Gerrit van de Maat, mijn MRI-wederhelft, je hebt met jouw verdediging de lat wel erg hoog weten te leggen. Peter Seevinck, jouw inzichten werken ontzettend verfrissend en *dat ene paper* gaan we echt afmaken. Daarnaast gaat minstens zo veel dank uit naar alle onderzoekers, klinici, laboranten, en iedereen nog meer die betrokken is (geweest) bij het (holmium) onderzoek en die ik hier niet persoonlijk genoemd heb.

Voor de nodige afleiding van het werk (‘iets met petri-schaaltjes’) heb ik altijd kunnen terugvallen op een geweldige groep vrienden, die van mijn tijd in Utrecht (vaak letterlijk) een feestje hebben gemaakt. Namen en rugnummers ga ik hier niet noemen, maar allen oneindig veel dank! U weet er van en ziet elkaar op mijn promotie feest. De heren voetballers van Hercules 6 (veld) en Voorwaarts 1 (zaal) bedankt voor de zeer gemakkelijke tijd op en naast het veld. H6, ik ben blij dat ik heb kunnen bijdragen aan het winnen van de Joop Zoetemelk Troffee (6 jaar op rij eindigen op de 2^e plaats). VW1, bedankt voor mijn eerste kampioenschappen sinds de D1.

Gerrit, Nienke, Floortje, Ronald, Menno, Sandra, en Stijntje, bedankt voor de altijd aanwezige interesse! Vera en Jaap, jullie zijn een levende doktersroman. Lieve Veer, ik ben er trots op dat je één van mijn paranimfen wilt zijn. Pap, ik ben bang dat je als ras-alfa nooit 100% zult begrijpen wat ik de afgelopen 4 jaar nou precies heb uitgevoerd, en volgens mij heb je daar ook wel vrede mee. Ik wil je enorm bedanken voor alle lieve support en interesse die je desalniettemin altijd getoond hebt. Mama†, ook al kon je er niet bij zijn, jouw onvoorwaardelijke steun en liefde heb ik altijd gevoeld. Lieve, lieve Lobke, dat we een week na elkaar promoveren is speciaal, maar feitelijk bijzaak. Jij bent zonder twijfel het meest speciale wat me ooit is overkomen. Blijf me verrassen lief!

Addenda

Samenvatting in het Nederlands

Dankwoord/Acknowledgments

List of affiliations

List of publications

Curriculum Vitae



List of affiliations

M.A.A.J. van den Bosch	Department of Radiology and Nuclear Medicine, University Medical Center Utrecht, Utrecht, The Netherlands
A.J. Dam	Department of Medical Technology, Gelre Hospital, Apeldoorn, The Netherlands
M. Elschot	Department of Radiology and Nuclear Medicine, University Medical Center Utrecht, Utrecht, The Netherlands
H.W.A.M. de Jong	Department of Radiology and Nuclear Medicine, University Medical Center Utrecht, Utrecht, The Netherlands
M.G.E.H. Lam	Department of Radiology and Nuclear Medicine, University Medical Center Utrecht, Utrecht, The Netherlands
J.F.W. Nijssen	Department of Radiology and Nuclear Medicine, University Medical Center Utrecht, Utrecht, The Netherlands
J.F. Prince	Department of Radiology and Nuclear Medicine, University Medical Center Utrecht, Utrecht, The Netherlands
M.L.J. Smits	Department of Radiology and Nuclear Medicine, University Medical Center Utrecht, Utrecht, The Netherlands
B.J. Vermolen	Department of Radiology and Nuclear Medicine, University Medical Center Utrecht, Utrecht, The Netherlands
M.A. Viergever	Image Sciences Institute, University Medical Center Utrecht, Utrecht, The Netherlands
B.A. Zonnenberg	Department of Radiology and Nuclear Medicine, University Medical Center Utrecht, Utrecht, The Netherlands

Addenda

Samenvatting in het Nederlands

Dankwoord/Acknowledgments

List of affiliations

List of publications

Curriculum Vitae



List of publications

Full papers (published and accepted for publication)

ML Smits, **M Elschot**, MA van den Bosch, GH van de Maat, AD van het Schip, BA Zonnenberg, PR Seevinck, HM Verkooijen, CJ Bakker, HW de Jong, MG Lam, JF Nijsen. *Imageable radioactive holmium-166 microspheres for treatment of liver malignancies: in vivo dosimetry based on SPECT and MRI*. Accepted with minor revision in: Journal of Nuclear Medicine.

M Elschot, MG Lam, MA van den Bosch, MA Viergever, HW de Jong. *Quantitative Monte Carlo-based yttrium-90 SPECT reconstruction*. Accepted in: Journal of Nuclear Medicine.

M Wondergem, ML Smits, **M Elschot**, HW de Jong, HM Verkooijen, MA van den Bosch, JF Nijsen, MG Lam. *Technetium-99m-MAA poorly predicts the intrahepatic distribution of yttrium-90 resin microspheres in hepatic radioembolization*. Accepted in: Journal of Nuclear Medicine.

M Elschot, BJ Vermolen, MG Lam, B de Keizer, MA van den Bosch, HW de Jong. *Quantitative comparison of PET and Bremsstrahlung SPECT for imaging the in vivo yttrium-90 microsphere distribution after radioembolization*. PLoS One 2013;8(2):e55742.

W Bult, SG Kroeze, **M Elschot**, PR Seevinck, FJ Beekman, HW de Jong, DR Uges, JG Kosterink, PR Luijten, WE Hennink, AD van het Schip, JL Bosch, JF Nijsen, JJ Jans. *Intratumoral administration of holmium-166 acetylacetonate microspheres: antitumor efficacy and feasibility of multimodality imaging in renal cancer*. PLoS One 2013;8(1):e52178.

GH van de Maat, PR Seevinck, **M Elschot**, ML Smits, H de Leeuw, AD van het Schip, MA Vente, BA Zonneberg, HW de Jong, MG Lam, MA Viergever, MA van den Bosch, JF Nijsen, CJ Bakker. *MRI-based biodistribution assessment of holmium-166 poly(L-lactic acid) microspheres after radioembolisation*. European Radiology 2013;23(3):827-35.

M Elschot, JF Nijsen, AJ Dam, HW de Jong. *Quantitative evaluation of scintillation camera imaging characteristics of isotopes used in liver radioembolization*. PLoS One 2011;6(11):e26174.

M Elschot, TC de Wit, HW de Jong. *The influence of self-absorption on PET and PET/CT shielding requirements*. Medical Physics 2010;37(6):2999-3007.

ML Smits, JF Nijsen, MA van den Bosch, MG Lam, MA Vente, JE Huijbregts, AD van het Schip, **M Elschot**, W Bult, HW de Jong, PC Meulenhoff, BA Zonnenberg. *Holmium-166 radioembolization for the treatment of patients with liver metastases: design of the phase I HEPAR trial*. Journal of Experimental & Clinical Cancer Research 2010;29(1):70.

Full papers (submitted for publication)

M Elschot, ML Smits, JF Nijsen, MG Lam, BA Zonnenberg, MA van den Bosch, MA Viergever, HW de Jong. *Quantitative Monte Carlo-based holmium-166 SPECT reconstruction*.

M Elschot, MG Lam, JF Nijsen, ML Smits, JF Prince, MA Viergever, MA van den Bosch, BA Zonnenberg, HW de Jong. *Tc-99m-MAA overestimates the dose to the lungs in radioembolization: a quantitative evaluation in patients treated with holmium-166 microspheres*.

Addenda

Samenvatting in het Nederlands

Dankwoord/Acknowledgments

List of affiliations

List of publications

Curriculum Vitae



Curriculum Vitae

Mattijs Elschot was born in Beuningen (Gelderland, The Netherlands) on the 3rd of November in 1983. In 2002, he completed his secondary school (VWO) at the Stedelijk Gymnasium Nijmegen and started studying Biomedical Engineering at the Eindhoven University of Technology. After studying a semester in Lisbon (Portugal), he passed his Bachelor's exam in 2006 and joined the Master Medical Engineering. During this study, he went to Boston (MA, USA) for an internship at the Massachusetts General Hospital. In 2009, he obtained his Master's degree after a graduation project at the Donders Institute for Brain, Cognition and Behaviour of the Radboud University Nijmegen. In the same year, he started working as a PhD student at the department of Radiology and Nuclear Medicine of the University Medical Center Utrecht. The results of his research are described in this thesis.

Mattijs Elschot werd geboren in Beuningen (Gelderland) op 3 november 1983. In 2002 voltooide hij zijn middelbare school (VWO) op het Stedelijk Gymnasium Nijmegen en begon met de studie Biomedische Technologie aan de Technische Universiteit Eindhoven. Na een semester gestudeerd te hebben in Lissabon (Portugal), slaagde hij in 2006 voor zijn Bachelor's examens en begon aan de Master opleiding Medical Engineering. Tijdens deze studie ging hij naar Boston (MA, Verenigde Staten) voor een stage binnen het Massachusetts General Hospital. In 2009 behaalde hij zijn Master's diploma na een afstudeer project aan het Donders Institute for Brain, Cognition and Behaviour van de Radboud Universiteit Nijmegen. In hetzelfde jaar ging hij aan de slag als promovendus op de afdeling Radiologie en Nucleaire Geneeskunde van het Universitair Medisch Centrum Utrecht. De resultaten van zijn promotie onderzoek zijn beschreven in dit proefschrift.